

https://dspace.org/

Crack tip shielding in fracture and fatigue: extrinsic versus intrinsic toughening

Dauskardt, Reinhold Horst

2015-01-16
http://hdl.handle.net/10539/16564

Downloaded from a DSpace repository. https://dspace.org/

CRACK TIP SHIELDING IN FRACTURE AND FATIGUE:

EXTRINSIC VERSUS INTRINSIC TOUGHENING

Reinhold Horst Dauskardt

December 1987

Work undertaken at:

Materials and Chemical Sciences Division,
Lawrence Berkeley Laboratory,
and
Department of Materials Science and Mineral Engineering,
University of California, Berkeley, CA 94720.

A thesis submitted to the Faculty of Engineering, University of the Witwatersrand, Johannesburg, in fulfillment of the requirements for the Degree of Doctor of Philosophy.

DECLARATION

I declare that this thesis is my own unaided work except where due acknowledgment is made to others. It is being submitted for the Degree of Doctor of Philosophy to the University of the Witwatersrand, Johannesburg. It has not been submitted before for any degree or examination to any other university.

Reinhold Horst Bauskardt

day of Sept. 1988.

ABSTRACT

Crack tip shielding phenomena, whereby the "effective crack driving force" experienced at the crack tip is reduced compared to the applied (far-field) value, are examined with reference to fracture toughness, sustained-load cracking and fatigue crack propagation behavior in metals, ceramics and composites. Sources of shielding are described in terms of mechanisms relying on crack path deflection and meandering, on the production of elastically constrained zones which envelop the crack (zone shielding), and on the generation of wedging, bridging or sliding forces between the crack surfaces (contact shielding).

The fatigue crack propagation behavior of pressure vessel steels is investigated, with particular emphasis on the role of crack tip shielding. Existing data has been reviewed and new data are presented, for both baseplate and weldments, on crack growth in steels exposed to hydrogen environments. It is shown that, at the lower growth rates where the majority of fatigue life is obtained, the influence of environmental degradation may be surprisingly small, a result which appears to originate from the mutually offsetting effects of environmental damage and increased crack tip shielding.

The role of dispersions of pre-existing grain boundary microvoids is investigated in fracture toughness and fatigue crack propagation behavior in a low alloy steel. Whereas the crack initiation and crack growth toughness (i.e., K_{Ic} and the tearing modulus) are severely degraded, even for comparatively mild degrees of microvoid damage, rates of subcritical crack growth by fatigue remain relatively unaffected. Results are interpreted in terms of a mutual competition between microstructural damage generated by the grain boundary microvoids, which promotes crack growth by lowering the intrinsic resistance of the microstructure, and the resulting tortuous crack paths, which extrinsically retard crack growth at low stress intensities by lowering the local tip "driving force" (crack tip shielding).

Contrary to traditional notions concerning ceramics, fatigue crack propagation under tension-tension loading is observed in a transformation-toughened partially-stabilized zirconia ceramic. Such subcritical behavior is demonstrated to be cyclically induced, based on a comparison with behavior under sustained loading and at varying cyclic frequencies. Growth rates over the range 10^{-10} to 10^{-6} m/cycle were found to be power-law dependent on the stress intensity range, and to show mean stress, crack closure, frequency and environmental effects, analogous to behavior in metals. Such behavior is rationalized primarily in terms of the non-linear behavior of material elements in the region of the crack tip due to mechanisms of extrinsic transformation toughening.

Although utilization of crack tip shielding can be a potent means to enhance toughness, the implication of such extrinsic toughening is crack size dependent behavior. This important consequence is shown to result in resistance curve behavior, anomalous "small crack" effects, and contrasting microstructural factors controlling crack initiation and growth. An additional consequence is susceptibility to cyclic fatigue damage in a range of advanced ceramic materials. Possible mechanisms of such fatigue degradation are identified and discussed with regard to four major classes of ceramic and ceramic-matrix composites. Suggestions for future work are presented.

ACKNOWLEDGEMENTS

I am indebted to Professor Robert O. Ritchie who provided a challenging and helpful supervision of the research program and most importantly, was a constant source of inspiration. Together with his remarkable knowledge of the literature, his assistance with compiling the extensive survey of available literature is gratefully acknowledged.

I am grateful to a number of people for many stimulating and helpful discussions. I would particularly like to express my gratitude to Mr Paul Spencer and Professor Earl Parker for assistance in the pressure vessel program, and Dr. Roland Cannon and Dr. David Marshall for discussions in the ceramics program.

For their extensive technical assistance which was indispensable in the completion of this work, I would like to thank in particular Dr. Weikang Yu, Fred Haulbensak, Jim Mason, and Dr. Raj Pendse.

Finally, I would like to thank Madeleine Penton for her patience and assistance in preparing the manuscript.

CONTENTS

DECLARATION ..... i.

ABSTRACT ..... ii.

ACKNOWLEDGEMENTS ..... iii.

CONTENTS ..... iv.

CHAPTER 1: INTRINSIC AND EXTRINSIC TOUGHENING

ABSTRACT ..... 1.

1.1. INTRODUCTION ..... 1.

1.2. MECHANISMS OF INTRINSIC TOUGHENING ..... 2.

1.3. GENERAL CONSIDERATIONS OF EXTRINSIC TOUGHENING ..... 4.

1.3.1. "Crack Driving Force" ..... 4.
1.3.2. Mechanisms of Crack Tip Shielding ..... 6.

1.4. CRACK DEFLECTION AND MEANDERING ..... 7.

1.5. ZONE SHIELDING ..... 8.

1.5.1. Introduction ..... 8.
1.5.2. Transformation Toughening ..... 10.
1.5.3. Microcrack Toughening ..... 13.
1.5.4. Dislocation Shielding ..... 14.
1.5.5. Other Forms of Zone Shielding ..... 16.

1.6. CONTACT SHIELDING ..... 17.

1.6.1. Introduction ..... 17.
1.6.2. Wedging ..... 17.
1.6.3. Bridging ..... 21.
1.6.4. Sliding ..... 21.
1.6.5. Combined Wedging and Bridging ..... 21.

1.7. COMBINED ZONE AND CONTACT SHIELDING ..... 22.

1.7.1. Plasticity-Induced Crack Closure ..... 22.

1.7.2. Phase Transformation-Induced Closure ..... 22.

1.8. CONCLUDING REMARKS ..... 22.

1.9. REFERENCES ..... 23.

1.10. FIGURES ..... 29.

CHAPTER 2: FATIGUE CRACK PROPAGATION BEHAVIOR IN PRESSURE VESSEL STEELS FOR HIGH PRESSURE HYDROGEN SERVICE

ABSTRACT ..... 37.

2.1. INTRODUCTION ..... 37.

2.2. EXPERIMENTAL PROCEDURES ..... 38.

2.3. RESULTS ..... 40.

2.3.1. Exposure to Gaseous Hydrogen ..... 41.
2.3.2. Prior Exposure to High Pressure Hydrogen ..... 42.
2.3.3. Influence of Load Ratio ..... 44.
2.3.4. Influence of Cyclic Frequency ..... 45.
2.3.5. Influence of Temperature ..... 45.
2.3.6. Influence of Weld and HAZ Microstructures ..... 45.

2.4. DISCUSSION ..... 47.

2.5. SUMMARY AND CONCLUSIONS ..... 49.

2.6. REFERENCES ..... 50.

2.7. FIGURES ..... 52.

CHAPTER 3: EFFECTS OF PRE-EXISTING GRAIN BOUNDARY MICROVOID DISTRIBUTIONS ON CRACK PROPAGATION IN LOW ALLOY STEEL

ABSTRACT ..... 72.

3.1. INTRODUCTION ..... 72.

3.2. EXPERIMENTAL PROCEDURES ..... 74.

3.3. RESULTS ..... 76.

3.3.1. Characterization of Microstructural Damage ..... 76.
3.3.2. Effects of Pre-Existing Microvoids on Fracture Toughness ..... 78.
3.3.3. Effects of Pre-Existing Microvoids on Fatigue Crack Propagation ..... 83.

3.4. CONCLUDING REMARKS ..... 87.

3.5. CONCLUSIONS ..... 88.

3.6. REFERENCES ..... 90.

3.7. APPENDIX I ..... 93.

3.8. APPENDIX II ..... 96.

3.9. FIGURES ..... 97.

CHAPTER 4: FATIGUE CRACK PROPAGATION IN TRANSFORMATION-TOUGHENED ZIRCONIA CERAMIC

ABSTRACT ..... 113.

4.1. INTRODUCTION ..... 113.

4.2. EXPERIMENTAL PROCEDURE ..... 114.

4.3. RESULTS ..... 116.

4.3.1. (i) Sustained Load Behavior ..... 116.
(ii) Influence of Cyclic Frequency ..... 117.
(iii) Influence of Stress Intensity Range ..... 117.
4.3.2. Environmental Contribution to Crack Growth ..... 117.
4.3.3. Influence of Fracture Toughness ..... 118.
4.3.4. Constant ΔK and Block Loading Sequences ..... 118.

4.4. DISCUSSION ..... 119.

4.5. CONCLUSIONS ..... 121.

4.6. REFERENCES ..... 122.

4.7. FIGURES ..... 124.

CHAPTER 5: IMPLICATIONS OF EXTRINSIC TOUGHENING AND PROPOSALS FOR FUTURE WORK

ABSTRACT ..... 136.

5.1. INTRODUCTION ..... 136.

5.2. GENERAL IMPLICATIONS OF EXTRINSIC TOUGHENING ..... 137.

5.3. POSSIBLE MECHANISMS OF FATIGUE IN CERAMIC MATERIALS AND PROPOSALS FOR FUTURE WORK ..... 139.

5.3.1. Introduction ..... 139.
5.3.2. Transformation and Microcracked Toughened Materials 142.
5.3.3. Deflection and Bridging Materials ..... 145.
5.3.4. Whisker Reinforced Ceramic-Matrix Materials ..... 146.
5.3.6. Ductile Phase Toughened Materials ..... 148.

5.4. REFERENCES ..... 149.

5.5. FIGURES ..... 151.

CHAPTER 5: IMPLICATIONS OF EXTRINSIC TOUGHENING AND PROPOSALS FOR FUTURE WORK

ABSTRACT ..... 136.

5.1. INTRODUCTION ..... 136.

5.2. GENERAL IMPLICATIONS OF EXTRINSIC TOUGHENING ..... 137.

5.3. POSSIBLE MECHANISMS OF FATIGUE IN CERAMIC MATERIALS AND PROPOSALS FOR FUTURE WORK ..... 139.

5.3.1. Introduction ..... 139.
5.3.2. Transformation and Microcracked Toughened Materials 142.
5.3.3. Deflection and Bridging Materials ..... 145.
5.3.4. Whisker Reinforced Ceramic-Matrix Materials ..... 146.
5.3.5. Ductile Phase Toughened Materials ..... 148.

5.4. REFERENCES ..... 149.

5.5. FIGURES ..... 151.

CHAPTER 1: INTRINSIC AND EXTRINSIC TOUGHENING

ABSTRACT

Crack tip shielding phenomena, whereby the "effective crack driving force" actually experienced in the near-tip region is reduced compared to the applied (far-field) value, are examined with reference to fracture toughness, sustained-load cracking and fatigue crack propagation behavior in metals, ceramics and composites. Sources of shielding are described in terms of mechanisms relying on crack path deflection and meandering, on the production of elastically constrained zones which envelop the crack (zone shielding), and on the generation of wedging, bridging or sliding forces between the crack surfaces (contact shielding). Examples of such **extrinsic** toughening are taken primarily from the crack closure and deflection of fatigue cracks, by mechanisms involving cyclic plasticity, corrosion debris and tortuous crack path morphologies, and from the toughening of brittle materials, by transformation, microcracking and ligament toughening mechanisms.

1.1. INTRODUCTION

In fracture mechanics terms, the extension of a crack can be considered to be driven by the presence of a **"crack driving force"** and opposed by the **resistance** of the **microstructure.** Here the crack driving force is generally defined by some characterizing parameter, such as the stress intensity K or path-independent integral J, which describes the dominant stress and deformation fields in the vicinity of the crack tip from a knowledge of crack size, applied load and geometry. Crack advance is thus restrained by lowering the applied load or by "toughening"* the material, e.g., through compositional or microstructural modification.

In alloy design, it is generally the perception that toughening is achieved by increasing the inherent microstructural resistance, e.g., by coarsening particle spacings, changing bond strengths, increasing ductility, etc. This process hereafter is termed **intrinsic toughening.** However, in many material systems, particularly with brittle fracture in ceramics (1) and fatigue in

*Toughening is used in the general sense here to describe material factors which impede crack extension, both in increasing fracture toughness and in retarding sub-critical crack growth by stress corrosion or fatigue.

metals (2), the actual source of toughness is distinctly different and arises from mechanisms of **crack tip shielding**, where toughness is achieved, i.e., crack extension is impeded, by mechanical, microstructural and environmental factors which locally reduce the crack driving force. This process is termed **extrinsic toughening.**

The initial aim of the present study is to provide a comprehensive review of the mechanistic origin and effect of such crack tip shielding in metals, ceramics and composites. Particular emphasis is placed on extrinsic shielding which arises from fatigue crack closure effects in metallic alloys and transformation toughening in ceramics. The study is subsequently extended to include three detailed independent investigations on crack propagation in two widely different material systems, namely, pressure vessel steels and a transformation toughened partially stabilized zirconia ceramic. Each study is designed to elucidate the separate roles of intrinsic and extrinsic toughening during crack propagation under different loading and environmental conditions. Finally, the general implications of extrinsic toughening, on crack extension behavior under monotonic and cyclic loading, is discussed. In particular, the discussion focuses on an important recent range of advanced structural ceramic and ceramic-matrix composites. Intensive scientific research in the last decade has resulted in major advances in the extrinsic toughening of these ceramics. However, the work undertaken in this study seems to indicate that these materials, contrary to conventional wisdom, may as a result become susceptible to cyclic fatigue degradation. Based on these considerations, possible mechanisms of such cyclic fatigue damage are discussed and suggestions for future research are presented.

Due to the considerable subject breadth of the present undertaking, each individual study has been compartmentalized and is reported as a complete study, usually associated with each chapter. Therefore, although the underlying concepts and implications of intrinsic and extrinsic toughening are maintained and apparent throughout the work, the continuity of each individual study is nevertheless preserved.

1.2. MECHANISMS OF INTRINSIC TOUGHENING

Intrinsic toughening mechanisms involve processes which predominate **ahead of the crack tip.** Typically, they pertain solely to a specific fracture mode, such as cleavage fracture induced by cracking of particles or microcracks in brittle materials, or ductile fracture from the coalescence of microvoids formed via interface decohesion (or cracking) of inclusion particles. This is in direct contrast to extrinsic mechanisms which generally result from processes occurring in the **wake** of an advancing crack. While the microstructural details of intrinsic processes are in general quite well understood, only fairly simplistic models exist for the

operation of these mechanisms in the highly triaxial field surrounding a crack tip, which it is necessary to consider for the prediction of fracture toughness.* These models are generally based on the concept of a critical fracture stress being exceeded across a microstructurally-significant characteristic distance for brittle fracture, e.g., the Ritchie-Knott-Rice model for cleavage fracture toughness (Figure 1.1(a)) (3), or a stress-state modified critical strain being exceeded over a characteristic distance for ductile fracture (Figure 1.1(b)), as recently reviewed for stationary and moving cracks by Ritchie and Thompson (4).

More recently, such intrinsic models have been reformulated on a stochastic basis and involve, for example, the statistics of sampling an array of fracture-inducing particles within the crack tip field ahead of the tip (5). Such probabilistic approaches are particularly useful for the more brittle ceramic materials which contain a strength dispersion due to the presence of surface machining flaws and interior microcracks (6). The approach is based on the Weibull fracture theory which takes the material volume under stress into consideration. This volume effect, which ultimately determines the final integrity, is based on a weakest-link statistical theory where failure of a single link or flaw implies catastrophic failure of the component. Most recent advances in this area have been the incorporation of the Batdorf theory which, based on Griffith fracture mechanics, specifies crack shape, size, and orientation, and includes multiaxial fracture criteria and the effects of shear sensitive cracks (7).

These approaches have been utilized principally for modelling the intrinsic fracture toughness behavior of metallic alloys (3-5, and see Chapter 3) and ceramics (6). They have yet to be utilized (in association with crack tip shielding models) to define the influence of microstructural features on the toughness and subcritical crack growth resistance of extrinsically toughened materials. In particular, in ceramic and ceramic-matrix composite materials, fracture behavior is likely to be far more of a compromise between intrinsic and extrinsic mechanisms. In addition, where crack propagation occurs under cyclic loading conditions, the effect of repeated loading and unloading cycles on decreasing the intrinsic toughness, by processes of accumulated damage ahead of the crack tip, requires further attention.

---

*Intrinsic mechanisms describing processes involved in the growth of fatigue cracks are even less understood, in part due to the lack of realistic analytical solutions describing the stress and deformation fields in the vicinity of a crack tip in the presence of cyclic plasticity.

1.3. GENERAL CONSIDERATIONS OF EXTRINSIC TOUGHENING

1.3.1. "Crack Driving Force"

The so-called "driving force" for crack growth is generally described by a field **characterizing parameter.** This is defined by *characterizing the stress and deformation fields local to the region* at the crack tip, usually through the use of asymptotic continuum analyses, and determining the functional form of the singular crack tip field which is appropriate for the primary mechanism of deformation, i.e. for the prevailing constitutive relationship. Provided this field can be considered to "*dominate*" the *local* stresses and strains over a region which is large compared to the scale of microstructural deformation and fracture events in the vicinity of the tip, the scalar amplitude of the field is taken as *the characterizing parameter* and can be used as a correlator of crack extension. By similitude, cracks are then assumed to extend at equal rates when subject to equal "driving forces".

Best known examples of this approach are for stationary cracks *subjected to tensile (Mode I) opening loads. For material* obeying a linear elastic constitutive law, in the limit of $r \to 0$, the asymptotic crack tip stress field is given as a function of the polar angle θ and distance r from the tip by (8,9):

$$\sigma_{ij}(r,\theta) \to \frac{K_I}{\sqrt{2\pi r}} \; f_{ij}(\theta) \tag{1.1}$$

where f_{ij} is a dimensionless function of θ. Here, crack advance for small-scale yielding conditions can be characterized in terms of the stress intensity factor, K_I. Alternatively, for elastic-plastic *material obeying a nonlinear elastic constitutive law* ($\bar{\varepsilon}/\varepsilon_0 = \alpha(\bar{\sigma}/\sigma_0)^n$), the limiting asymptotic field is given by the so-called HRR singularity (10,11), in terms of the flow stress σ_0, flow strain ε_0 and work hardening exponent n, e.g.

$$\sigma_{ij}(r,\theta) \to \sigma_0 \left(\frac{J}{\alpha\sigma_0\varepsilon_0 I_n r}\right)^{\frac{1}{n+1}} \tilde{\sigma}_{ij}(\theta,n) \tag{1.2a}$$

$$\varepsilon_{ij}(r,\theta) \to \alpha\varepsilon_0 \left(\frac{J}{\alpha\sigma_0\varepsilon_0 I_n r}\right)^{\frac{1}{n+1}} \tilde{\varepsilon}_{ij}(\theta,n) \tag{1.2b}$$

1.3. GENERAL CONSIDERATIONS OF EXTRINSIC TOUGHENING

1.3.1. "Crack Driving Force"

The so-called "driving force" for crack growth is generally *described by a field characterizing parameter.* This is defined by characterizing the stress and deformation fields local to the region at the crack tip, usually through the use of asymptotic continuum analyses, and determining the functional form of the singular crack tip field which is appropriate for the primary mechanism of deformation, i.e. for the prevailing constitutive relationship. Provided this field can be considered to *"dominate" the local* stresses and strains over a region which is large compared to the scale of microstructural deformation and fracture events in the vicinity of the tip, the scalar amplitude of the field is taken as the characterizing parameter and can be used as a correlator of crack extension. By similitude, cracks are then assumed to extend at equal rates when subject to equal "driving forces".

Best known examples of this approach are for stationary cracks subjected to tensile (Mode I) opening loads. For material obeying a linear elastic constitutive law, in the limit of $r \to 0$, the asymptotic crack tip *stress field is given as a function of the polar angle* θ and distance r from the tip by (8,9):

$$\sigma_{ij}(r,\theta) \to \frac{K_I}{\sqrt{2\pi r}} \; f_{ij}(\theta) \tag{1.1}$$

where f_{ij} is a dimensionless function of θ. Here, crack advance for small-scale yielding conditions can be characterized in terms of *the stress intensity factor,* K_I. *Alternatively,* for elastic-plastic material obeying a nonlinear elastic constitutive law ($\bar{\varepsilon}/\varepsilon_0 = \alpha(\bar{\sigma}/\sigma_0)^n$), the limiting asymptotic field is given by the so-called HRR singularity (10,11), in terms of the flow stress σ_0, flow strain ε_0 and work hardening exponent n, e.g.

$$\sigma_{ij}(r,\theta) \to \sigma_0 \left(\frac{J}{\alpha\sigma_0\varepsilon_0 I_n r}\right)^{\frac{1}{n+1}} \tilde{\sigma}_{ij}(\theta,n) \tag{1.2a}$$

$$\varepsilon_{ij}(r,\theta) \to \alpha\varepsilon_0 \left(\frac{J}{\alpha\sigma_0\varepsilon_0 I_n r}\right)^{\frac{1}{n+1}} \tilde{\varepsilon}_{ij}(\theta,n) \tag{1.2b}$$

where $\tilde{\sigma}_{ij}$, $\tilde{\varepsilon}_{ij}$ and I_n are dimensionless functions of θ and n, and α is a material constant of order unity. Here, crack advance can be characterized by the path-independent integral J (9,12), at least provided crack extension is limited (4). Similar characterizing parameters can be defined for creeping solids in terms of constitutive laws for primary and secondary creep. This approach provides a basis for the parameter C^*, the rate-dependent or viscous analog of J (13,14).

As characterizing parameters remain undetermined by the asymptotic analyses, they are generally computed from a complete analysis of the applied loading and geometry. Such solutions for K_I and J applicable to a wide variety of cracking situations are now tabulated, for example, in several handbooks (15-17), and are used with regularity in fracture mechanics based design and lifetime calculations and for characterizing crack extension in standard crack initiation and crack propagation tests. Although the adoption of these solutions rely on global considerations of crack size, overall geometry and applied loading conditions, they are assumed to guarantee a characterization of the local field. However, where the local, near-tip "driving force", actually experienced at the crack tip, differs from this nominal or applied "driving force", due to some local mechanical, microstructural or environmental phenomenon in the vicinity of the crack tip, the crack can be considered to be experiencing crack tip shielding, or in some cases anti-shielding. For small-scale yielding under monotonic loading conditions, this can be expressed as:

$$K_{tip} = K_I - K_s, \tag{1.3}$$

where K_{tip} is the local near-tip stress intensity, K_I is the applied or nominal stress intensity, and K_s is the stress intensity due to shielding. Under cyclic loading, this expression can be written as:

$$\Delta K_{tip} = \Delta K - K_s, \tag{1.4}$$

where ΔK_{tip} is the local near-tip stress intensity range, and the applied stress intensity range, ΔK, is given by $K_{max} - K_{min}$. The objective of extrinsic toughening is thus to enhance K_s.

As rates of sub-critical crack growth, by mechanisms such as fatigue, stress corrosion and hydrogen-assisted cracking, are generally found to exhibit a power law dependence upon the driving force, extrinsic toughening may be extremely potent in reducing crack extension rates. For this reason, crack tip shielding can provide a general approach to toughening in the widest spectrum of materials, ranging from the primary mechanism of toughening brittle ceramics to the retardation of fatigue crack growth rates in ductile metals.

1.3.2. Mechanisms of Crack Tip Shielding

Mechanisms of extrinsic toughening may be categorized into several distinct classes (2,18). These classes involve crack tip shielding from a) crack deflection and meandering, b) nonlinear or dilated zones surrounding the wake of the crack, termed "zone shielding", c) wedging, bridging and/or sliding between crack surfaces, termed "contact shielding", and d) combined zone and contact shielding. Individual micro-mechanisms are illustrated schematically in Figure 1.2. Distinctions between these classes of shielding are important as they cause reductions in the local "driving force" via different routes. These, in turn, have implications on how their potency changes with cyclic versus monotonic loading and with increasing versus decreasing stress intensities.

Although under monotonic loading, shielding simply results in a reduction in the local "driving force", under cyclic loading the effect may take different forms, schematically illustrated in Figure 1.3. Since the principal "driving force" for fatigue crack advance, under small-scale yielding for example, is the range of stress intensity, ΔK may be reduced locally by a decrease in K_{max} and a smaller decrease in K_{min}, as with crack deflection; a decrease in K_{max} and an increase in K_{min}, as with bridging or sliding; or simply an increase in K_{min}, as in wedging.

The nature of the shielding mechanism, or combination of mechanisms involved, will thus dictate the specific behavior observed. For example, crack deflection produces a multiplicative reduction in the local Mode I stress intensity, and thus may be expected to have an equal effect at all stress intensity levels. Shielding from enclaves of plastic zones or dilated zones of material undergoing phase transformation, microcracking or void formation conversely produces a fixed reduction in local stress intensity, at least for a constant equilibrium zone size. As the degree of shielding is related to the zone size (see section 1.5), zone shielding mechanisms are favored at high stress intensity levels, but are generally less potent in fatigue as the range of stress intensity remains unchanged, although the mean K_I or load ratio ($R \approx K_{min}/K_{max}$) is reduced. Contact shielding through wedging, conversely, raises the local stress intensity under monotonic loading, yet reduces the driving force for fatigue by opposing the closing of the crack. This latter process is the essence of the well-known phenomenon of fatigue crack closure whereby the nominal ΔK range is reduced by effectively raising K_{min}. The effect of crack closure is therefore favored at low stress intensities where crack tip opening displacements are smallest. Contact shielding through bridging (e.g. ligament or fiber toughening), or sliding (e.g. sliding crack surface interference), results in a reduced driving force for both monotonic and cyclic crack extension as these mechanisms oppose both the opening and closing of the crack.

The following sections examine broadly the various categories of extrinsic toughening, and describe the individual mechanical, *microstructural and environmental micro-mechanisms responsible* for such processes in a diverse range of materials, including, metals, ceramics, concrete, polymers and composites, subjected to monotonic and cyclic loading.

1.4. CRACK DEFLECTION AND MEANDERING

Crack deflection, whereby the Mode I **"crack driving force"** is locally reduced by deviations of the crack path from the surface of maximum tensile stress, has been shown to play a significant role in governing the toughness and rate of sub-critical crack growth in a wide range of materials, from the toughness of brittle ceramics (19) to fatigue crack growth in ductile metallic alloys (20). Solutions for various idealized deflection geometries are available for both elastic and nonlinear elastic cracks. As an example, the Cotterell and Rice solution (21) for a simply kinked crack (Figure 1.2), subjected to a nominal Mode I stress intensity K_I, can be expressed in terms of the kink angle Θ and **local** Mode I and Mode II stress intensities k_1 and k_2 along the kink:

$$k_1 = \cos^3(\Theta/2)\ K_I \qquad (1.5a)$$

$$k_2 = \sin(\Theta/2)\ \cos^2(\Theta/2)\ K_I \qquad (1.5b)$$

This solution applies provided the length b of the deflected portion is small compared to the total crack length, although the magnitude of the changes in stress intensity are kink size independent. In the general case, which includes twisting of the crack, the local crack tip "driving force", K_{tip}, (for coplanar growth along the deflected portion) can then be estimated in terms of the maximum strain energy release rate, G:

$$K_{tip} = \sqrt{EG} = [k_1^2\ (1-\nu^2) + k_2^2\ (1-\nu^2) + k_3^2\ (1+\nu)]^{0.5} \qquad (1.6)$$

where k_3 is the local Mode III stress intensity, E is Young's modulus, and ν is Poisson's ratio. For the simply tilted crack in Figure 1.2, reduction in "crack driving force" for in-plane deflections of, say, 30 and 90 deg are thus of the order of 10 and 50%, respectively; much larger reductions can be achieved with associated twisting of the crack.

The size, rather than simply the angle, of the deflected crack segment can have an effect on the kinetics of crack advance, as it

dictates the extent of crack extension which experiences the reduced "driving force". Accordingly, shielding through crack deflection can be more significant in affecting sub-critical crack growth rates, such as by fatigue. By considering both the changes in apparent growth rate and local "driving force" for repeated (two-dimensional) crack segments involving a deflection angle θ, a deflected distance b and undeflected distance c, the effective crack-tip stress intensity range, ΔK_{tip}, and growth rate, da/dN, of an idealized (linear elastic) deflected crack have been estimated to be (20):

$$\Delta K_{tip} = \left\{ \frac{b \cos^2(\theta/2) + c}{b + c} \right\} \Delta K_L \qquad (1.7a)$$

$$da/dN = \left\{ \frac{b \cos\theta + c}{b + c} \right\} (da/dN)_L \qquad (1.7b)$$

where $(\Delta K)_L$ and $(da/dN)_L$ are the nominal stress intensity range and growth rate of the linear undeflected Mode I crack, respectively.

By promoting crack deflection through the inclusion of particles with high aspect ratios, increases in fracture toughness by up to a factor of 3 have been claimed for ceramic materials (22). Moreover, the phenomenon can be extremely important during the fatigue of metallic alloys where the deflection of the crack path may additionally induce shielding from the wedging of enlarged fracture surface asperities (20,23).

1.5. ZONE SHIELDING

1.5.1. Introduction

Most material systems exhibit an inelastic zone of material that surrounds a crack and varies in geometric form in response to the applied stress field ahead of the crack tip. Such zones are typically exemplified by the plastic zone in metals, a microstructurally "damaged" zone in ceramics and a "crazed" zone in polymers. In some systems, however, the specific mechanism of deformation responsible for the zone may lead to a substantial reduction of the stress fields in the region of the crack tip. The crack tip is thus effectively shielded from the remotely applied stress. The general form of the crack tip stress fields may therefore be characterized by two stress intensity factors in the presence of a process zone as shown in Figure 1.4. Outside the process zone, for a linear elastic material under small scale yielding, eqn. 1.1 may be written as:

$$\sigma_{ij}(r,\theta) \rightarrow \frac{K_I}{\sqrt{2\pi r}} f^o_{ij}(\theta) \qquad (1.8)$$

where K_I is the stress intensity determined from the applied loads. Assuming that the non-linear deformation mechanism has saturated in the process zone and hence, the material once more behaves linear elastically, the stress fields near the crack tip may be characterized by another stress intensity factor, K_{tip}, such that:

$$\sigma_{ij}(r,\theta) \rightarrow \frac{K_{tip}}{\sqrt{2\pi r}} f^i_{ij}(\theta) \qquad (1.9)$$

The extent of zone shielding is finally obtained by rearranging eqn. 1.3 to obtain:

$$K_S = K_I - K_{tip} \qquad (1.10)$$

This form of "zone shielding" was first quantitatively studied in ceramic systems containing a dispersion of metastable zirconia particles which transform from a monoclinic to tetragonal crystal structure in the high stress fields ahead of a crack tip. When confined to a region surrounding the crack, shielding results from the dilatational and shear strains associated with the transformation, and is termed transformation toughening (24-28). The concept of such shielding has subsequently found more general application in the explanation of microcrack toughening in ceramics (29-31), crack tip dislocation shielding (32,33), crack wake plasticity in metals (34), and void formation and growth in rubber toughened polymers (35).

It is important to emphasize that the above mechanisms of shielding, which will be individually discussed in more detail in the following sections, results primarily from the zone left behind in the wake of a stably advancing crack. Indeed, the zone at the tip of a stationary crack may in some instances lead to local increases in the crack tip fields (anti-shielding) (27) and decreases in the intrinsic toughness (30). This is in contrast to the significant toughening effect observed in austenitic steels which undergo a deformation-induced martensitic transformation. Here the principal effect of the transformation plasticity has been suggested to stabilize plastic flow by accommodating flow localization ahead of the crack tip (36). This mechanism might also provide some contribution to toughening in transformation toughened ceramics, however, theoretical understanding is limited and beyond the scope of the present review.

Finally, the deformation mechanism responsible for the process zone may result in modification of the crack tip geometry or changes in the intrinsic toughness of the crack tip material. These effects may produce significant alteration of the final measured toughness in addition to the zone shielding effect. A number of possibilities are immediately apparent and are schematically illustrated in Figure 1.5. The most simple case involves the crack remaining atomically sharp typical of most brittle materials. Here only the shielding contribution to the final toughness need be considered. However, where blunting of the crack tip occurs, characteristic of metallic alloys, the synergistic effect of both blunting and shielding contribute to the final toughness. Where crack tip processes occur to degrade the intrinsic toughness, such as microcracking in ceramic systems and void formation in metals, the counteracting influences of a reduced intrinsic toughness and shielding from the process zone need be assessed. Lastly, changes of the intrinsic toughness due to phase transformation of material at the crack tip, or when the crack intercepts a second phase, should also be considered.

1.5.2. Transformation Toughening

Transformation toughening, in which shielding is achieved from the stress-induced phase transformation of material surrounding a crack, has proved to be a potent toughening mechanism in a variety of primarily brittle material systems. A number of independent theoretical approaches have been advanced to account for the extent of toughening that may be attributed to the principally dilatant transformation strains. The initial approach of McMeeking and Evans (25) was based on direct calculation of the modified crack tip stress fields using Eshelby transformation and weight function techniques. Subsequent more general thermodynamic approaches are based on Griffith concepts (37) or by adopting energy balance integrals (26). Most recently, in a detailed account of the mechanics of transformation toughening, Rose (38) has used a continuous distribution of strain centers to represent the inelastic strain due to the transformation. Shielding is then characterized by perturbations in the complex potentials which are used to describe the stress fields, due to strain centers in the vicinity of the crack tip. In general, these models have resulted in reasonably consistent results.

Common to these theoretical approaches is the requirement to specify the transformation zone shape. While early approaches considered only the hydrostatic component of the crack tip field as the transformation criterion (25,26), later works have attempted to include shear effects (27,38-40). Depending on the selected transformation criterion, marked differences in the shape of the frontal transformation zone may result. As the attendant toughening, K_s, not only scales with the process zone height H, but is modified by the frontal zone morphology, specification of the zone shape is important (28,38,39).

The extent of shielding (K_S) may derive from the frontal process zone has been shown to be K_S for the case of purely dilatational transformation strains and hydrostatic nucleation criterion (25,26). However, if shear strains are included in the analysis, marginal contributions to shielding may result depending on particle shape and orientation effects (27). As the transformation zone extends into the wake of a stably advancing crack, R-curve behavior, where resistance to further crack advance increases, obtains and is depicted in Figure 1.6. Steady state shielding results after a crack extension of approximately 5H. The magnitude of the maximum toughening increment predicted for a purely dilatational transformation which does not reverse in the wake, and when all particles in the zone transform (supercritical transformation), has an asymptotic value (25,26):

$$K_S = 0.22\ E\ f_v\ \varepsilon^T_{ij}\ \sqrt{H}\ /(1-\nu) \qquad (1.11)$$

where f_v in the volume fraction of transforming particles, and ε^T_{ij} is the transformation strain. The transformation zone width is given by:

$$H = \frac{\sqrt{3}(1+\nu)^2}{12\pi}\left(\frac{K_I}{\sigma_c}\right)^2 \qquad (1.12)$$

where σ_c is the critical hydrostatic stress to initiate transformation. The inclusion of shear and particle shape and orientation effects have revealed that substantially more toughening may result than the purely dilatational case (27). In addition, it has been suggested that where transformation proceeds by shear localization in the process zone, damage in the form of microcracks are accumulated by the intersection of shear bands and grain boundaries, therefore providing an additional component of dilatational strain in the zone which will enhance the toughening effect (39). The results of these considerations have been summarized in (28).

The most comprehensive experimental data demonstrating transformation toughening and associated R-curve behavior, that is, increasing toughness with crack propagation, has been obtained in zirconia and alumina ceramics containing partially stabilized zirconia particles as a dispersed phase (41-44). The stress-induced transformation of these particles from the tetragonal to monoclinic crystal structure is accompanied by an unconstrained volumetric expansion of 4 - 6% (45,46) and a shear component of about 14% (47). Typical volume fractions, f_v, of particles of 0.3 to 0.5 (48) result in total dilatational strains, e_{d_t} of 0.012 to 0.03. The concomitant increase in toughness presently achievable in a Mg-PSZ, for example,

is from an untoughened matrix of 3 MPa$\sqrt{m}$ to 14 MPa$\sqrt{m}$ (41,44,49).

Experimental measurement of R-curve behavior in transformation toughened materials is difficult and often exacerbated by near surface residual compression due to specimen preparation procedures, contributions from other extrinsic toughening mechanisms, such as microcrack shielding, deflection and branching, and uncertainty in the location on the R-curve (28,43). A comparison of theoretical and measured R-curves of a MgO-PSZ ceramic, displaying characteristically large increases in toughness with initial crack propagation, is shown in Figure 1.7 (from ref. 44). Note the complexities introduced by different test methods (surface cracks compared to through thickness cracks) can lead to variations of the measured R-curves. Suppression of transformation toughening in the same material by heat-treatment results in a significantly reduced R-curve reflecting microcracking and crack branching effects (50).

The effect of transformation toughening is also apparent on other forms of subcritical crack propagation behavior. The beneficial effect of a reduced near tip driving force due to transformation toughening on the environmentally-enhanced sustained-load crack growth behavior of both zirconia and alumina ceramics has been investigated by Becher (51,52). A marked reduction of slow crack growth velocity in these toughened ceramics, compared to untoughened versions, was apparent in moist air and water environments.

The effect of transformation toughening on crack propagation under cyclic loading conditions is less clear. Rates of cyclic crack propagation in materials exhibiting susceptibility to fatigue are generally more dependent on the range of stress intensity, rather than the mean or maximum levels (53). As zone shielding mechanisms influence K_{max} and K_{min} equally, and hence do not alter the range of stress intensity, potential benefits may only be derived from a reduction of the mean stress.

In metallic alloys, studies of low cycle fatigue behavior in unstable austenitic steels subject to a strain-induced martensitic transformation, in which a positive volume expansion occurs, have revealed that at small strain amplitudes where the transformation is limited to a region surrounding the crack, improvements in fatigue life may result (54-56). However, at high strain amplitudes and in less stable austenite where the extent of transformation is large and not confined to a zone surrounding the crack, fatigue behavior may be independent of the extent of transformation (57) or exhibit a reduced fatigue life (55,56). Results of these early studies have been reviewed by Hornbogen (58) and retardation of fatigue crack propagation rates rationalized in terms of the internal compressive stresses associated with the transformed zone.

Conversely, it is generally considered that conventional monolithic ceramics do not suffer significant degradation by cyclic fatigue based primarily on the very limited crack tip plasticity

apparent in these materials (59-61). In ceramics toughened by zone shielding mechanisms, however, the resulting nonlinear stress-strain response of material in the transformation zone suggests the strong possibility of fatigue effects under cyclic loading conditions. Such fatigue crack propagation behavior under tension-tension loading in a transformation-toughened zirconia ceramic was first observed in the present study, and results are presented in Chapter 4. Akin to fatigue behavior in metals, cyclic crack growth rates are found to show similar dependencies on cyclic frequency, load ratio and alternating stress intensity range (Chapter 4). It would therefore appear that the non-linear behavior of material elements in the region of the crack tip associated with transformation toughening may induce significant susceptibility to fatigue crack propagation in materials normally not prone to fatigue degradation.

1.5.3. Microcrack Toughening

Analogous to the role of a dilatational phase transformation in transformation toughened materials, the formation of microcracks in regions of high stress fields ahead of a crack tip in brittle materials may lead to a dilated microcrack zone and hence an attendant toughening enhancement. Specification of the dilatation, ε^M_{ij}, allows the toughness to be predicted by adopting similar procedures developed for transformation toughening (25,26). The analysis, however, differs in two important respects: firstly, the intrinsic toughness of the microcracked material directly ahead of the crack tip is degraded; and secondly, the bulk modulus of the microcracked material in the process zone is reduced (30,31,62-64).

For brittle materials, studies on porous glasses (65) indicate that an appropriate choice for the decay in intrinsic toughness with increasing volume fraction of microcracks, f_m, might be:

$$K^m_0 = K_0(1-f_m) \tag{1.13}$$

where K^m_0 and K_0 are the intrinsic toughnesses of the material with and without microcracks, respectively. In addition, solutions of the bulk modulus of the microcracked material (66) allow the dilatational component of the strain induced by non-interacting microcracks to be written in terms of the prior residual stress on the microcrack plane, σ_R, as (28,67):

$$M_{ij} = \frac{16(1-\nu^2)}{3}\frac{\sigma_R f_m}{E_0} \tag{1.14}$$

where E_0 is the modulus of the uncracked material.

It follows from the analytic development of (30,63) that the frontal process zone does not produce an appreciable change in

toughness, due to the counteracting influences of crack tip shielding from the initial microcracking zone and degradation of the intrinsic toughness. The maximum predicted shielding increment obtained from a fully developed microcracked process zone exhibits the form:

$$K_S = 0.21\ E_D\ \varepsilon^M_{ij}\ \sqrt{H}\ /(1 - \nu) \qquad (1.15)$$

where H is the zone height. Similar to transformation toughening, R-curve behavior naturally obtains for process zone sizes intermediate of the frontal and fully developed zone (30). Comparison of the magnitude of transformation toughening with microcrack toughening, eqn. 1.11 with eqn. 1.15, reveal that for similar zone sizes, H, and dilatational strains, $e^T_{ij} \approx \varepsilon^M_{ij}$, the mechanisms are comparably effective. However, as the microcracked toughening increment is superimposed on a degraded intrinsic toughness (eqn. 1.13), the effect of microcrack shielding may be offset particularly at larger f_m.

Microcrack toughening and associated R-curve behavior have been observed in a number of material systems including polycrystalline Al_2O_3 and ZrO_2 ceramics (28,31), and in concrete and rocks (68,69). Microcracking is particularly susceptible to residual stress fields which when superimposed on the applied crack tip fields initiate microcracks. Nucleation therefore occurs at sites of thermal contraction anisotropy among randomly orientated grain boundaries (28,31), thermal contraction mismatch around inclusions, and in the matrix between intergranular particles with large facet lengths (28,62). In addition, particles undergoing phase transformation induce residual tensile stresses that may initiate microcracks (62). Preliminary analysis of the simultaneous transformation and microcracking situation have revealed that more potent shielding may be expected than for transformation toughening alone (70).

1.5.4. Dislocation Shielding

The generation of a distribution of dislocations in the plastic zone ahead of a crack tip is expected in materials which exhibit plastic behavior. In particular, between the extremes of truly ductile materials which exhibit gross plasticity, and ideally brittle materials which fail by pure brittle cleavage with no discernible plasticity, a class of materials exist in which cracks remain atomically sharp, but are surrounded by a zone of dislocations generated by the high stress fields associated with the crack tip (71). For example, in situ TEM observation of shear cracking of Mo and W (72), and stainless steel (73) has revealed the presence of dislocation distributions ahead of sharp crack tips in Mode III separation.

The question then arises as to the interaction of the dislocations with eachother, and more specifically, their role in

modifying the applied crack tip stress fields. In addition, if the production (or annihilation) of dislocations results in a blunting reaction at the crack tip then a concomitant decrease in the stress intensity of the blunted crack tip results. The combined effect of blunting and dislocation shielding processes on the crack tip stress fields may be approximated by:

$$\sigma_{tip} = \sigma_{app}\sqrt{c/\rho} \quad - \quad \sigma_{shield} \tag{1.16}$$

where c is the crack length and ρ the root radius.

At present, only a limited number of crack tip dislocation configurations have been treated analytically (32,33,71). These results do, however, provide a basis for understanding more complex loading modes and material defect configurations. For the trivial case of a screw dislocation with Burgers vector b, situated a distance c ahead of a semi-infinite Mode III shear crack (Figure 1.8(a)), the analysis indicates that the crack tip stress intensity factor, K_D, close to the crack tip due to the presence of the dislocation is given by (32):

$$K_D = - \frac{\mu b}{\sqrt{2\pi c}} \cos(\theta/2) \tag{1.17}$$

where μ is the shear modulus. If the dislocation is generated by the crack tip stress fields then the applied stress intensity K_{III} and the stress intensity due to the dislocation K_D have opposite signs and net shielding obtains. A simple extension of the analysis indicates that for an array of 2N-1 dislocations situated on a circle, radius r, around the crack tip (Figure 1.8(b)), the resultant shielding stress intensity is (32):

$$K_D = - \frac{\mu b}{\sqrt{2\pi c}} \left(\frac{4N}{\pi}\right) \qquad \text{for } N > 10. \tag{1.18}$$

The combined effects of a large number of dislocations may therefore be expected to produce a significant effect on the dislocation shielding component (for example, a value of $K_D \approx 50$ MPa$\sqrt{m}$ has been estimated from eqn. 1.18 for typical values of μ, b, c and N characteristic of steels (32)) and hence the final measured fracture toughness. In addition, knowledge of dislocation and crack-tip interactions has also been used to assess the extent of shielding expected in brittle transformation toughened ceramic materials where the transformation strains are represented by dislocation dipole configurations (33).

1.5.5. Other Forms of Zone Shielding

A number of additional forms of zone shielding have been postulated which involve constrained zones formed by processes of crack wake plasticity (35) and void formation and growth (35,74). In the case of zones formed from crack wake plasticity, shielding is assumed to derive from the irreversible plastic deformation of material associated with the crack tip plastic zone. Some progress has been made in the understanding of contained plasticity associated with crack tips (9), however, analytical solutions are mathematically difficult, particularly in the case of tensile (Mode I) opening under plane strain conditions. With the introduction of plasticity, added complexities resulting from finite geometry changes at the crack tip must also be considered if an accurate description of local conditions is desired. Nevertheless, estimates of the extent of toughening from plastic dilatation have been undertaken, particularly when enhanced by the presence of ductile particle dispersions. Typical material systems include rubber precipitate toughened polymers (35) and ductile phase toughened ceramics, which at present is limited to two composite systems: Al_2O_3/Al and WC/Co (1). Here the plasticity induced zone shielding tends to be increased by ductile particles having small size and low yield strengths (1).

The dilatation associated with the formation and growth of voids in a zone of material surrounding a crack has also been suggested as a potential form of shielding (1,35). In particular, the marked reduction in the stress singularity ahead of a crack exposed to the growth of cavitation damage in the crack tip field has been analyzed (74). In the present study, estimates of the shielding from hydrogen attack damage in the form of creep-enhanced methane bubble formation in a zone surrounding a crack in a low alloy steel are presented in Chapter 3. In the majority of these preliminary studies, however, certain conjectures have been required to obtain a final result. These have included the neglect of the influence of the holes on the plastic crack tip stress field and interactions between holes. Caution should therefore be exercised in applying these results in a fully quantitative sense.

Although perhaps not primarily a zone shielding mechanism, an important additional form of toughening may result from the plasticity associated with the crack tip in materials which exhibit elastic-plastic constitutive behavior. In particular, this effect is related to the nonproportional straining of material near the crack plane of a growing crack, compared to the predominantly proportional plastic straining of material elements near a stationary crack. Analysis of the deformation field traveling with an advancing plane-strain crack has been attempted and the functional form of the near tip crack profile revealed for a elastic-plastic solid (75,76). It is shown that, neglecting any large-scale crack tip geometry changes, whereas the strains decay as $1/r$ ahead of a stationary crack, for a moving crack, the strain singularity is weaker, decaying as a function of $\ln(1/r)$. This effect therefore necessarily leads to

characteristic resistance curve behavior and stable crack growth for initial crack extension.

1.6. CONTACT SHIELDING

1.6.1. Introduction

Contact shielding involves physical contact between mating crack surfaces, either directly, through the presence of fracture surface asperities or with fibers in a composite, or through the presence of an external medium, such as with corrosion debris or the entry of a fluid. The principal mechanisms of such contact are through wedging inside the crack, bridging across the crack, sliding between crack surfaces and combinations of these modes. In general, since the degree of shielding will be largest when the extent of crack opening is comparable with the size of the contacting entity, in contrast to zone shielding, contact shielding is enhanced at low stress intensities where the crack tip opening diplacements are smallest. Furthermore, where wedging is involved, although significant shielding can be achieved under cyclic loading, the effect under monotonic loads may be quite different and lead to local increases in the crack tip "driving force", i.e. to anti-shielding.

1.6.2. Wedging

Corrosion debris-induced crack closure: It is now realized that insoluble corrosion products formed within slowly growing cracks exposed to active environments can significantly affect their subsequent crack extension rates. This occurs by a mechanical wedging action which can either promote sustained-load cracking or retard cracking under cyclic loads where the size of the products becomes comparable with the crack tip opening displacements (77,78). The latter shielding phenomenon, termed oxide-induced crack closure, causes a reduction in the local stress intensity range through an effective increase in K_{min}, and has been found to have significant effects on fatigue crack growth at very low, near-threshold stress intensities. Notable examples are where crack surface oxides and calcareous deposits are formed during corrosion fatigue in structural steels tested, respectively, in moist air and sea water (79,80).

The concept of shielding by oxide-induced crack closure in fatigue can be simply modelled by considering the excess corrosion deposit as a rigid wedge, of thickness s comparable with the crack opening displacement, extending along the crack length a distance 2a behind the crack tip (81). Assuming only a mechanical closure phenomenon arising from the wedge and ignoring hysteresis and inelastic effects, the resultant stress intensity at the crack tip due to the wedge is given by:

$$K_R = \frac{s\,E}{4(1-\nu^2)\sqrt{\pi\ell}} \qquad (1.19)$$

Note from Eqn. 1.19 that deposits in the immediate vicinity of the crack tip have a dominating influence in the development of shielding by this mechanism.

During a fatigue cycle, contact between the crack surfaces will occur on unloading when the stress intensity reaches a value $K_R = K_{cl}$, referred to as the closure stress intensity. Using conventional fatigue terminology, the "driving force" for crack advance is reduced from the nominal ΔK to an effective value, given by:

$$\Delta K_{eff} = K_{max} - K_{cl} \qquad (1.20)$$

provided the excess oxide thickness exceeds the minimum crack opening displacement imposed by the fatigue cycle. In terms of the general nomenclature used in the present review (Eqn. 1.4), $\Delta K_{eff} = \Delta K_{tip}$, with the shielding stress intensity given by:

$$\begin{aligned} K_s &= K_{cl} - K_{min} && (K_{cl} > K_{min}) \\ &= 0 && (K_{cl} \leq K_{min}) \end{aligned} \qquad (1.21)$$

Contact shielding during fatigue crack growth from crack closure induced by the formation of crack surface corrosion deposits is promoted by a) small crack tip opening displacements (i.e. at low stress intensity ranges), comparable with the size of the debris, b) low load ratios, which facilitate fretting between the crack walls through small crack tip opening displacements, c) highly oxidizing media, which generate excess corrosion deposits, d) rough fracture surfaces, which at low ΔK levels again facilitates fretting, and e) lower strength materials, where again the extent of corrosion debris is enhanced due to greater fretting (82).

As wedge shielding is only relevant where the size of the wedge and the crack opening displacements are comparable, oxide-induced crack closure is most effective during fatigue crack propagation at near-threshold levels, typically below 10^{-9} m/cycle. For example, near-threshold fatigue crack growth rates at low load ratios in structural steels are significantly faster in dry helium gas, and slower in water or steam, compared to behavior in room air (82). This surprising effect can be primarily attributed to the generation of thicker oxide films, and hence greater shielding, for tests in the oxidizing environments. No such effect is apparent at high load

ratios or at higher ΔK levels. In such lower strength materials, the thickness of these films can be far larger than the natural limiting oxide thickness due to fretting oxidation between the crack walls. The accumulation of debris here arises from a continual breaking and reforming of oxide scale due to repeated contact and inelastic Mode II displacements between the crack surfaces.

Aside from its contribution to the role of environment and load ratio in influencing near-threshold behavior, contact shielding from oxide-induced closure also results in a strong effects of yield strength on ΔK_{TH} values, as oxides films are enhanced in lower strength materials. However, with steels of higher tensile strength and in the majority of aluminum alloys, the degree of fretting oxidation appears much reduced, with the result that, except in very oxidizing environments, the thickness of the oxide films remains small compared to the crack tip opening displacements such that the contribution to shielding from this mechanism becomes negligible (82).

Fracture surface roughness-induced crack closure: A more general source of contact shielding during cyclic crack growth arises from the wedging action of fracture surface asperities, where crack tip opening displacements are small and where significant Mode II crack tip shear displacements occur (23,83-85). Such roughness-induced fatigue crack closure is thus most effective at near-threshold stress intensities, particularly where the crack path morphology can be made tortuous and locally mixed-mode by frequent crack deflection. Such irregular crack profiles are promoted in coarse planar slip materials, e.g., in coherent particle hardened systems such as underaged aluminum alloys and certain Ni-based superalloys where a faceted crystallographic mode of crack growth is often observed at low ΔK levels, and in duplex microstructures, e.g., in dual-phase steels and α/β titanium alloys where a meandering crack path can be achieved through frequent deflection at the harder phase (82).

The concept of shielding by roughness-induced closure arises from the premature contact of fracture surfaces asperities on unloading due to mismatch from the irreversible nature of inelastic crack tip displacements and slip-step oxidation. The extent of wedge shielding thus depends upon the degree of fracture surface roughness and the extent of Mode II crack tip displacements. For example, from simple two-dimensional geometric modelling of the process, the closure stress intensity at the point of first asperity contact has been given as (23):

$$K_{cl} = K_{max} \sqrt{\frac{2\gamma X}{1 + 2\gamma X}} \qquad (1.22)$$

where γ is a measure of surface roughness taken as the ratio of height h to width w of asperities and X is the ratio of Mode II to Mode I crack tip displacements. Although only a first order model, experimental results in a range of ferrous and non-ferrous alloys have been found to be in reasonable agreement with this relationship.

Contact shielding during fatigue crack growth from roughness-induced closure is similarly most effective at low stress intensity ranges. It is promoted by a) small crack tip opening diplacements, comparable with the size of the asperities, b) low load ratios, again to minimize crack tip opening, c) inelastic crack tip deformation and oxidation of slip-steps, which can lead to a mismatch of mating portions of the crack surfaces on unloading, d) small plastic zone sizes, of order of grain size, which encourages single shear (Stage I) mechanisms of crack advance, e) coarse-grained materials and microstructures hardened with coherent shearable precipitates capable of inducing coarse planar slip, where crack paths are crystallographic, and f) crack deflection mechanisms, induced by stress-state, environment, duplex microstructures and load excursions, where crack paths may be highly nonlinear.

Roughness-induced crack closure has been found to play a significant role in influencing fatigue crack growth in a wide range of materials. For example, the beneficial effects in reducing near-threshold crack growth rates (at low load ratios) of coarse grain sizes in ferritic steels and titanium alloys (86), underaged or planar slip microstructures in precipitation-hardened aluminum and nickel-based alloys (87), and dual phase microstructures in steels and α/β titanium alloys (88,89), have been directly traced to enhanced shielding from rougher fracture surfaces. The largest effects, however, are seen in duplex microstructures, as shown by the results for duplex ferritic-martensitic structures in low carbon steels (90). By modifying the proportion and primarily the morphology of the two phases by intercritical heat-treatment, significant deflection of the crack path can be achieved, with corresponding large increases in closure (i.e., K_{cl}/K_{max} approaching 0.9). The result for Fe-2Si-0.1C and AISI 1008 steels is threshold ΔK_{TH} values of approximately 20 MPa$\sqrt{m}$ without loss in strength, thought to be the largest thresholds reported to date for a metallic material (90). However, consistent with extrinsic toughening mechanisms, crack initiation resistance (evaluated in terms of the fatigue limit) was not similarly enhanced.

In the present investigation, the effects of both forms of wedging mechanisms, namely, oxide- and roughness-induced crack closure, are examined on influencing the fatigue crack propagation behavior in several classes of structural pressure vessel steels (2.25Cr-1Mo, 3Cr-1.5Mo and a Mn-Mo-Ni steel) under different environmental conditions. The results of these studies are reported in Chapter 2.

1.6.3. Bridging

Crack bridging is most prominent in whisker- and fiber-reinforced composites where the matrix fails leaving a region of unbroken fibers spanning the crack wake; the intact fibers act as bridges and inhibit crack opening. Such shielding is promoted in ceramic-matrix composites where interface debonding occurs, i.e., where the fibers are strong but the interfacial shear strength between fiber and matrix is weak. This topic has been extensively studied by Evans (1).

Understanding of the role of crack bridging in influencing the fracture and fatigue of metal-matrix composites is considerably less advanced. This is in part because many such composites are designed with strong fiber/matrix interfaces and thus do not develop crack bridging to any significant degree. An exception is a laminated aluminum alloy composite bonded together by an arimid fiber reinforced adhesive. Since the strength of the laminate/matrix interface is comparatively weak, crack propagation in these hybrid alloys is impeded both by delamination along the interface and consequent bridging of the unbroken laminated sheets (91).

1.6.4. Sliding

Sliding crack surface interference: A prominent characteristic of non-Mode I crack growth is the interaction (i.e., rubbing) between sliding crack surfaces. This phenomenon has been shown to be a very potent shielding mechanism during fatigue crack growth in Mode III (anti-plane shear), i.e., in torsionally-loaded samples, where it is referred to as **sliding crack surface interference** or torsional crack closure (92,93). Mechanisms of interference involve friction, abrasion, fretting debris formation and interlocking of fracture surface asperities, enabling the broken portion of the specimen to carry a portion of the applied torque. It further leads to heating of the specimen and obstruction of fractographic details. Since this mechanism acts to oppose equally both the "opening" and "closing" of the crack, similar to bridging mechanisms, the effect in fatigue is to reduce the range of local "driving force", at a constant mean value.

1.6.5. Combined Wedging Plus Bridging

Fluid pressure-induced crack closure: Contact shielding can also occur in liquid environments through the hydrodynamic action of fluid within the crack (fluid pressure-induced crack closure). Due to the approaching velocity of the crack walls, such fluids can generate an internal fluid pressure, which acts as a wedge to oppose the closing, and to a lesser extent as a bridge to oppose the opening, of the crack under cyclic loading (94,95). The mechanism has been shown to be important during fatigue crack propagation in oil environments, e.g., for rolling contact fatigue in lubricated bearings, where the rate of crack growth, at fixed nominal ΔK, becomes a function of the

kinematic viscosity of the oil.

1.7. COMBINED ZONE AND CONTACT SHIELDING

1.7.1. Plasticity-Induced Crack Closure

The original concept of crack closure, as described by Elber (96), was considered to arise from the elastic constraint of material surrounding the plastic zone enclave in the wake of the crack tip. Crack wake material elements had previously been plastically stretched at the tip. Closure then resulted from interference between crack surfaces due to the misfit strains. Such shielding induced by cyclic plasticity, which has been described analytically (34) and numerically (97-99), is generally considered to be more prevalent under plane stress conditions and in thus more significant at higher stress intensity levels.

1.7.2. Phase Transformation-Induced Crack Closure

The stress- or strain-induced phase transformation of material surrounding a crack, analogous to transformation toughening reviewed in section 1.5.2, can produce an additional crack closure mechanism. Examples of materials in which this effect may occur include shape memory alloys and metastable stainless steels. Here, if the transformation from an austenitic to martensitic phase, which occurs locally in the region of the crack tip, involves a positive volume change, the constraint of the surrounding material will place such regions under compression. In addition to the expected zone shielding which may then arise (section 1.5.2), enhanced crack closure effects are also expected during fatigue crack propagation as a result of the reduced crack opening displacements associated with the transformation strains. However, the effect in fatigue has not been carefully documented, nor analyzed for the more realistic case where deformation involves significant deviatoric strains under cyclic loading conditions.

1.8. CONCLUDING REMARKS

The mechanisms of intrinsic and extrinsic toughening have been discussed, particularly with regard to the potent crack tip shielding that may derive from the latter. Although some mechanisms of extrinsic shielding have long been known to operate during fatigue in metallic alloys, their full potential has only recently been realized with the development of an impressive range of advanced material systems, particularly in the area of ceramic and composite materials, which rely on mechanisms of extrinsic shielding to enhance toughness. These materials now have the capability of offering a unique set of properties commonly not available in more traditional materials.

1.9. REFERENCES

1. A. G. Evans, In Fracture Mechanics: 20th Symposium, ASTM STP in press, American Society for Testing and Materials, Philadelphia, PA., 1987.

2. R. O. Ritchie and W. Yu, In Small Fatigue Cracks, R. O. Ritchie and J. Lankford, eds., TMS-AIME, Warrendale, PA, 167-89, 1986.

3. R. O. Ritchie, J. F. Knott and J. R. Rice, J. Mech. Phys. Solids, 21, 395-410, 1973.

4. R. O. Ritchie and A. W. Thompson, Met. Trans. A, 16A, 233-248, 1985.

5. T. Lin, A. G. Evans and R. O. Ritchie, J. Mech. Phys. Solids, 34, 477-497, 1986.

6. A. G. Evans, J. Am. Ceram. Soc., 61, 302-308, 1978.

7. L. M. Sheppard, Adv. Mater. Pro., 130, 64-66, 1986.

8. G. R. Irwin, In Structural Mechanics: Proceedings of the 1st Symposium on Naval Structural Mechanics, J. N. Goodier and N. J. Hoff, eds., Pergamon, New York, 557-591, 1958.

9. H. Liebowitz, ed., Mathematical Fundamentals, vol. 2 of Fracture, Academic, New York, 1968.

10. J. R. Rice and G. F. Rosengren, J. Mech. Phys. Solids, 16, 1-12, 1968.

11. J. W. Hutchinson, J. Mech. Phys. Solids, 16, 13-31, 1968.

12. J. R. Rice, J. App. Mech., 35, 379-86, 1968.

13. H. Riedel and J. R. Rice, In Fracture Mechanics: 12th Symposium, ASTM STP 700, American Society for Testing and Materials, Philadelphia, PA, 112, 1980.

14. A. Saxena, In Fracture Mechanics: 17th Volume, ASTM STP 905, American Society for Testing and Materials, Philadelphia, PA, 185, 1986.

15. G. C. Sih, Handbook of Stress Intensity Factors, Lehigh University, Bethlehem, PA, 1973.

16. D. P. Rooke and D. J. Cartwright, Compendium of Stress Intensity Factors, H. M. Stationary Office, London, 1976.

17. H. Tada, P. C. Paris and G. R. Irwin, The Stress Analysis of Cracks Handbook, Del Research, Hellertown, PA, 1973.

18. R. O. Ritchie, R. H. Dauskardt and R. M. Cannon, Lawrence Berkeley Report No. LBL-20656, University of California, Berkeley, CA, 1987.

19. K. T. Faber and A. G. Evans, Acta. Metall., 31, 565-76, 1983.

20. S. Suresh, Met. Trans. A, 16A, 249-60, 1985.

21. B. Cotterell and J. R. Rice, Int. J. Fract., 16, 155, 1980.

22. H. Ruf and A. G. Evans, J. Am. Ceram. Soc., 66, 328-32, 1983.

23. S. Suresh and R. O. Ritchie, Met. Trans. A, 13A, 1627-31, 1982.

24. R. C. Garvie, R. H. Hannink, and R. T. Pascoe, Nature (London), 258, 703-704, 1975.

25. R. M. McMeeking and A. G. Evans, J. Am. Ceram. Soc., 65, 242-45, 1982.

26. B. Budiansky, J. W. Hutchinson, and J. C. Lambropoulos, Int. J. Solids Struct., 19, 337-55, 1983.

27. J. C. Lambropoulos, Int. J. Solids Struct., 22, 1083-1106, 1986.

28. A. G. Evans and R. M. Cannon, Acta Metall., 34, 761-800, 1986.

29. N. Claussen, J. Steeb and R. F. Pabst, Am. Ceram. Soc. Bull., 56, 559, 1977.

30. A. G. Evans and K. T. Faber, J. Am. Ceram. Soc., 67, 255-60, 1984.

31. M. Ruhle, A. G. Evans, R. M. McMeeking, P. G. Charalambides and J. W. Hutchinson, Acta Metall., 35, 2701-10, 1987.

32. B. S. Majumdar and S. J. Burns, Acta. Met., 29, 579-88, 1981.

33. R. J. Seyler, S. Lee and S. J. Burns, In Science and Technology of Zirconia II, The American Ceramics Society, Columbus, OH, 213-24, 1981.

34. B. Budiansky and J. W. Hutchinson, J. App. Mech., 45, 267-76, 1978.

35. A. G. Evans, Z. B. Ahmad, D. G. Gilbert and P. W. R. Beaumont, Acta. Metall., 34, 79-87, 1986.

36. G. B. Olson and M. Cohen, In Mechanical Properties and Phase Transformations in Engineering Materials, E. R. Parker Symp., S. D. Antolovich, R. O. Ritchie and W. W. Gerberich, eds., TMS, PA, 367-90, 1986.

37. D. B. Marshall, A. G. Evans and M. Drory, In Fracture Mechanics of Ceramics - vol. 5 and 6, eds. R. C. Bradt, A. G. Evans, D. P. H. Hasselman and F. F. Lange, Plenum Press, New York, 1982.

38. L. R. F. Rose, Proc. R. Soc. Lond. A, 412, 169-97, 1987.

39. I-Wei Chen, J. Am. Ceram. Soc., 69, 181-89, 1986.

40. J. C. Lambropoulos, J. Am. Ceram. Soc., 69, 218-22, 1986.

41. D. B. Marshall, J. Am. Ceram. Soc., 69, 173-80, 1986.

42. P. F. Becher, Acta Metall., 34, 1885-91, 1986.

43. A. H. Heuer, J. Am. Ceram. Soc., 70, 689-98, 1987.

44. D. B. Marshall and M. V. Swain, "Crack Resistance Curves in Magnesia-Partially-Stabilized Zirconia", Rockwell International Science Center, Thousand Oaks, CA, 1987, to be published.

45. R. J. H. Hannink, K. A. Johnston, R. T. Pascoe and R. C. Garvie, Adv. Ceram., 3, 116, 1981.

46. E. C. Subbarao, Adv. Ceram., 3, 1, 1981.

47. W. M. Kriven, W. L. Fraser and S. W. Kennedy, Adv. Ceram., 3, 82, 1981.

48. M. V. Swain, R. H. Hannink and R. C. Garvie, Fract. Mech. Ceram., 6, 339, 1983.

49. M. V. Swain, Acta. Metall., 33, 2083-91, 1985.

50. M. V. Swain and R. J. H. Hannink, Adv. Ceram., 11, 1984.

51. P. F. Becher, J. Mat. Sci., 21, 297-300, 1986.

52. P. F. Becher, J. Am. Ceram. Soc., 66, 485-488, 1983.

53. P. C. Paris and F. Erdogan, J. Basic Eng., Trans. ASME, Ser. D, 85, 528-34, 1963.

54. A. Pineau and R. Pelloux, Metall. Trans., 5, 1103-12, 1974.

55. D. Hennessy, G. Steckel and C. Alstetter, Metall. Trans., 7, 415-24, 1976.

56. G. Franke and C. Alstetter, Metall. Trans., 7, 1719, 1976.

57. G. R. Chanani and S. D. Antolovich, Metall. Trans., 5, 217-29, 1974.

58. E. Hornbogen, Acta Met., 26, 147-52, 1978.

59. A. G. Evans, Int. J. Fract., 16, 485-98, 1980.

60. A. G. Evans and M. Linzer, Ibid., 12, 217-22, 1976.

61. A. G. Evans and E. R. Fuller, Metall. Trans., 5, 27-33, 1974.

62. A. G. Evans and K. T. Faber, J. Am. Ceram. Soc., 64, 394-98, 1981.

63. A. G. Evans and Y. Fu, Acta Metall., 33, 1525-31, 1985.

64. G. D. Bowling, K. T. Faber and R. G. Hoagland, J. Am. Ceram. Soc., 70, 849-54, 1987.

65. J. Zwissler and A. Adams, Fracture Mechanics of Ceramics, eds. R. C. Bradt, D. P. H. Hasselman, F. F. Lange and A. G. Evans, 6, 211-41, Plenum, New York, 1983.

66. B. Budiansky and J. O'Connell, Int. J. Solids Struct., 12, 81, 1976.

67. J. W. Hutchinson, Acta Metall., 35, 1605-19, 1987.

68. L. Peck, C. C. Barton and R. B. Gordon, J. of Geophys. Res., 90, 11533-46, 1985.

69. J. Labuz, S. P. Shah and C. H. Dowding, Int. J. of Rock Mech. and Mining Sci., 22, 85-98, 1985.

70. K. T. Faber, Adv. Ceram., 11, 293, 1984.

71. J. R. Rice and R. Thomson, Philos. Mag., 29, 73 - 97, 1874.

72. S. Kobayashi and S. M. Ohr, Proc. 37th Ann. Meeting of EMSA, ed. G. W. Bailey, 424, 1979.

73. S. M. Ohr and J. Narayan, Phil. Mag., A41, 81, 1980.

74. M. D. Thouless, C. H. Hsueh and A. G. Evans, Acta Metall., 31, 1675-87, 1983.

75. J. R. Rice and E. P. Sorensen, J. Mech. Phys. Solids, 26, 163-86, 1978.

76. W. J. Drugan, J. R. Rice and T. -L. Sham, J. Mech. Phys. Solids, **30**, 447-73, 1982.

77. A. T. Stewart, Eng. Fract. Mech., **13**, 463, 1980.

78. R. O. Ritchie, S. Suresh and C. M. Moss, J. Eng. Mat. Technol., **102**, 293, 1980.

79. S. Suresh and R. O. Ritchie, Eng. Fract. Mech., **18**, 785, 1983.

80. P. M. Scott, T. W.Thorpe and D. R. V. Silvester, Corr. Sci., **23**, 559, 1983.

81. S. Suresh, A. F. Blom and C. J. Beevers, *In* Fatigue Thresholds, J. Backlund, A. F. Blom and C. J. Beevers, eds., EMAS Ltd., Warley, U. K., **1**, 391, 1982.

82. S. Suresh and R. O. Ritchie, In Fatigue Crack Threshold Concepts, D. L. Davidson and S. Suresh, eds., TMS-AIME, Warrendale, 227, 1984.

83. N. Walker and C. J. Beevers, Fat. Eng. Mat. Struct., **1**, 135, 1979.

84. K. Minakawa and A. J. McEvily, Scripta Met., **6**, 633, 1981.

85. W. W. Gerberich, W. Yu and K. Esaklul Metall. Trans. A, **15A**, 875, 1984.

86. G. T. Grey, J. C. Williams and A. W. Thompson, Metall. Trans. A, **14A**, 421, 1983.

87. R. D. Carter, E. W. Lee. E. A. Starke and C. J. Beevers, Metall. Trans. A, **15A**, 555, 1984.

88. V. B. Dutta, S. Suresh and R. O. Ritchie, Metall. Trans. A, **15A**, 1193, 1984.

89. J. E. Allison, In Fracture Mechanics: 18th Symposium, ASTM STP 945, American Society for Testing and Materials, Philadelphia, PA, 1987.

90. J. -K. Shang, J. -L. Tzou and R. O. Ritchie, Metall. Trans. A, **18A**, 1613, 1987.

91. R. Marissen, Eng. Fract. Mech., **19**, 261, 1984.

92. H. Nayeb-Hashemi, F. A. McClintock and R. O. Ritchie, Metall. Trans. A, **13A**, 2197, 1982.

93. E. K. Tschegg, Mater. Sci. Eng., **54**, 127, 1982.

94. K. Endo, T. Okada, K. Komai and M. Kiyota, Bull. JSME, 15, 1316, 1972.

95. J. -L. Tzou, C. H. Hsueh, A. G. Evans and R. O. Ritchie, Acta Metall., 33, 117, 1985.

96. W. Elber, Eng. Fract. Mech., 2, 37, 1970.

97. J. C. Newman, In Mechanics of Crack Growth, ASTM STP 590, American Society for Testing and Materials, Philadelphia, PA, 281, 1976.

98. A. F. Blom and D. K. Holm, Eng. Fract. Mech., 22. 997, 1985.

99. N. A. Fleck, Eng. Fract. Mech., 25, 441, 1986.

1.10. FIGURES

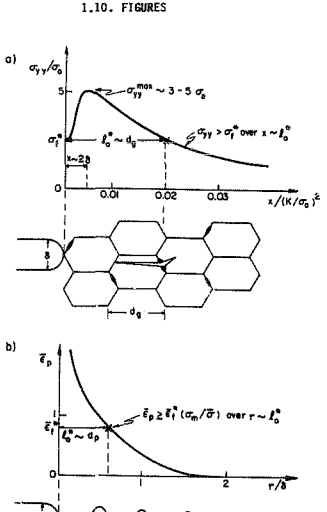


Figure 1.1 Schematic idealization of microscopic fracture criteria pertaining to (a) critical stress-controlled model for cleavage fracture (RKR), and (b) stress-modified critical strain-controlled model for microvoid coalescence. Such models provide a micro-mechanical description of intrinsic toughness. σ_f^* and $\bar{\varepsilon}_f^*$ are the critical fracture stress and critical equivalent plastic strain, respectively, and ℓ_0 the characteristic distance.

EXTRINSIC TOUGHENING MECHANISMS

1. CRACK DEFLECTION AND MEANDERING

2. ZONE SHIELDING
   - — transformation toughening
   - — microcrack toughening
   - — crack wake plasticity
   - — crack field void formation
   - — residual stress fields
   - — crack tip dislocation shielding

3. CONTACT SHIELDING
   - — wedging:
     - corrosion debris-induced crack closure
     - crack surface roughness-induced closure
   - — bridging:
     - ligament or fiber toughening
   - — sliding:
     - sliding crack surface interference
   - — wedging + bridging:
     - fluid pressure-induced crack closure

4. COMBINED ZONE AND CONTACT SHIELDING
   - — plasticity-induced crack closure
   - — phase transformation-induced closure



Figure 1.2 Schematic representation of the classes and mechanisms of crack tip shielding. Such processes impede crack propagation by locally reducing the "crack driving force".

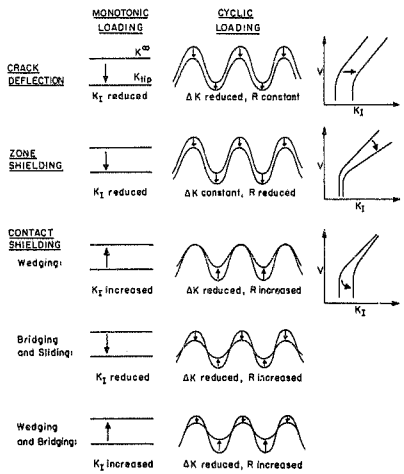


Figure 1.3 Effect of specific crack tip shielding mechanism of the "crack driving force", e.g., the stress intensity K_I, and crack velocity, v, under monotonic and cyclic loading.

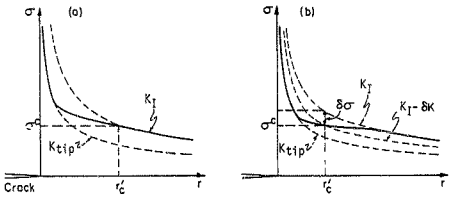


Figure 1.4 The modified crack tip stress fields in the presence of a transformation zone assuming (a) that the field outside the zone is not modified by the zone, and (b) including a possible reduction of the field outside the zone due to the presence of the zone.

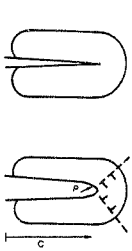


Figure 1.5 Deformation mechanisms occurring in the vicinity of the crack tip may result in modifications to the crack tip geometry or the intrinsic toughness. Possible scenarios include (a) the crack remaining atomically sharp, (b) blunting of the crack tip, (c) degradation of the intrinsic toughness, and (d) changes of the intrinsic toughness due to phase transformation or the interception of second phases.

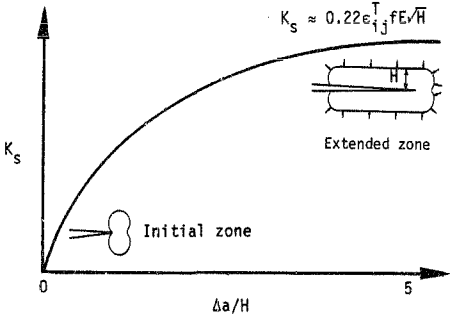


Figure 1.6 Variation of shielding with extension of the transformation zone into the wake of a stably advancing crack showing the initial frontal zone and the steady-state zone. R-curve behavior for intermediate zone sizes is predicted.

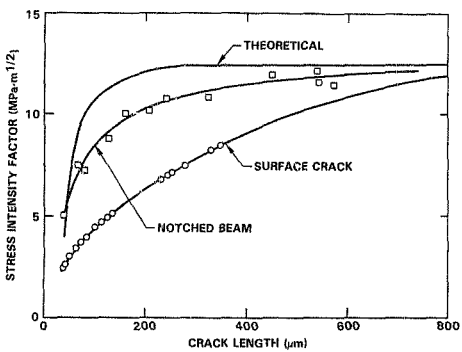


Figure 1.7 R-curves for a MgO-PSZ material. Curves indicating data for "small" surface cracks and "large" cracks in double cantilever beam tests are compared to theoretical predictions.

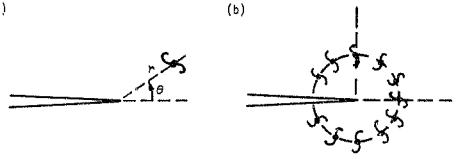


Figure 1.8 Crack tip dislocation configurations indicating (a) a screw dislocation off the symmetry plane of the crack, and (b) a circle of 2N - 1 dislocations around the crack tip.

CHAPTER 2: FATIGUE CRACK PROPAGATION BEHAVIOR IN PRESSURE VESSEL STEELS FOR HIGH PRESSURE HYDROGEN SERVICE

ABSTRACT

The fatigue crack propagation behavior of heavy-section pressure vessels steels is reviewed, with specific emphasis on alloys commonly utilized for high pressure hydrogen service. Existing data has been surveyed and new data are presented, for both base plate and weldments, on crack growth in steels exposed to in situ gaseous hydrogen environments, where hydrogen embrittlement is the principal concern, and after prior exposure to high pressure/high temperature hydrogen environments, where hydrogen attack becomes critical. It is shown that at the lower growth rates, where the majority of fatigue life is obtained, the influence of hydrogen on crack growth rates may in certain cases be surprisingly small, a result which appears to originate from the mutually offsetting effects of environmental damage and increased crack tip shielding. Such shielding, which reduces the local "crack driving force", may arise from fracture surface corrosion debris, heavily deflected crack paths and compressive zones around the crack tip (due to dilation induced by methane bubble formation).

2.1. INTRODUCTION

Economical large-scale coal conversion processes require the use of extremely large, thick-section pressure vessels, capable of containing mechanically and chemically hostile, hydrogen-containing environments at high temperatures and pressures (1). Material requirements for such applications involve tough, weldable steels, with sufficient hardenability to maintain uniform properties throughout plate thicknesses up to 300-400 mm, yield strengths in excess of 350 MPa, and sufficient creep, fatigue and environmental degradation resistance to withstand hydrogen (+ H_2S) atmospheres at gas pressures of typically 20 MPa and temperatures up to 550°C (1-3). In recent years, several low alloy steels have been identified a candidate materials for such applications, including ASTM A387, A542 and A533B, and 3Cr-Mo steels. Strength, ductility, toughness and creep properties of these materials are generally well documented (e.g., refs. 1-5), although data on the resistance to fatigue crack propagation are not commonly available.

To meet this need, studies in recent years have focused on examining the mechanics and mechanisms of crack growth in structural alloys, specifically with respect to the roles of low temperature

damage from hydrogen embrittlement and high temperature/pressure damage from hydrogen attack (6-14). Studies have concentrated on examining behavior at lower growth rates (down to ~ 10^{-11} m/cycle), as this regime dominates overall life in defect-tolerant lifetime calculations. In the present study, new data on fatigue crack propagation in experimental pressure vessel steels and weldments are presented and compared with existing results on a number of commercial steels which have been considered for high pressure hydrogen service. The study therefore severs as a compendium of the fatigue properties of these materials under selected environmental conditions.

More importantly, however, the investigation elucidates the roles of intrinsic and extrinsic toughening effects during crack growth in a metallurgically more traditional metallic alloy system. Consistent explanations of both new and existing data is demonstrated using these concepts. It is shown that the detrimental effect of hydrogen environments in accelerating fatigue crack advance is often reduced at lower growth rates, due primarily to the retarding influence of crack tip shielding (15,16). Such shielding, which results in the crack tip experiencing a reduced local "driving force" (i.e., a lower near-tip ΔK), acts to offset microstructural damage from environmental attack.

2.2. EXPERIMENTAL PROCEDURES

The steels investigated were selected to provide a wide range of response to varying testing conditions and hydrogen environments. Materials from existing studies included several classes of 2.25Cr-1Mo steels (ASTM designations A387 Class 2 Grade 22, A542 Class 2 and A542 Class 3), and a Mn-Mo-Ni (ASTM designation A533B Class 2) nuclear pressure vessel steel. Data from the weld and heat-affected-zone (HAZ) regions of a thick-section A387-2-22 steel weldment are also included. New data is presented on one commercial (Japanese Steel Works, JSW) and two experimental (3Cr-1.5Mo-0.2V and 3Cr-1.5Mo) 3Cr-Mo pressure vessel steels. In addition, the fatigue properties of the weld and HAZ regions of thick-section JSW and 3Cr-1.5Mo steel weldments were also assessed. The materials, together with their chemical composition and ambient temperature mechanical properties, are listed in Tables I and II, respectively. Details of heat treatments and microstructures are presented in Table III.

Fatigue crack propagation rates were measured using either manual or computer controlled decreasing (load shedding) or increasing stress intensity range techniques on 10-12.5 mm thick compact tension C(T) specimens machined principally in the T-L orientation. Fatigue data are presented in the form of crack growth rate per cycle, da/dN, as a function of the nominal stress intensity range, ΔK. Tests were conducted at frequencies between 1 and 500 Hz (primarily at 50 Hz) on electro-servo-hydraulic testing machines in

temperature-controlled environments of moist laboratory air (30% relative humidity) and dehumidified gaseous hydrogen (138 kPa).

Crack lengths were continuously monitored using d.c. electrical potential techniques, whereas the extent of crack closure was assessed using a back-face strain compliance method. The stress intensity at crack closure, K_{cl}, was calculated at the point of first crack surface contact during unloading by defining the deviation from linearity of the elastic compliance curves (13). Closure values were computed in situ during the testing procedure using high speed computer data acquisition and control equipment. Based on such data, the effective (near-tip) cyclic driving force", ΔK_{eff}, locally experienced at the crack tip was calculated as $K_{max} - K_{cl}$, where $K_{cl} \geq K_{min}$ (i.e. load ratios, $R = K_{min}/K_{max}$) were maintained in the range 0.05 with the threshold stress intensity range, ΔK_{TH}, below which cracks are presumed dormant, defined at a maximum growth rate of 10^{-11} m/cycle.

Previous tests in gaseous hydrogen environments were conducted using an internally sealed chamber, locally clamped to the test piece. Gas purity and temperature were preserved by means of an extensive purification and temperature control system (14). In the present study, prior microstructural damage in the form of hydrogen attack was achieved by prolonged exposure of oversized specimen blanks to gaseous hydrogen in high pressure autoclaves. Various combinations of time, temperature and hydrogen pressure were selected for the A387-2-22 and the AE538 steels (13), and the 3Cr-Mo and JSW steels, and are listed in Table IV. Following exposure, the material was held at 200°C for 24 hours to eliminate the effects of any reversible hydrogen embrittlement caused by dissolved atomic hydrogen. Further experimental details are described elsewhere (13,14).

As an indication of the effect of the microstructural damage on material toughness, ductile to brittle transition curves were determined using Charpy V-notch impact toughness tests. Specimens were tested at temperatures ranging from -78°C to 100°C. In addition, plane strain fracture toughness tests to determine $J_R(\Delta a)$ resistance curves were conducted using 20% side-grooved, 25 mm thick, compact C(T) testpieces. Crack initiation toughness was estimated from J_{Ic} ($= K_{Ic}^2/E'$) values, in accordance with revision 83-3 of ASTM Standard E813-83, where $E' (= E/(1-\nu^2))$ is the effective Young's modulus for plane strain and ν is Poisson's ratio.

Fatigue crack propagation studies in the HAZ regions were conducted by growing cracks perpendicularly through the HAZ at constant $\Delta K = 17$ MPa$\sqrt{m}$ in the JSW and $\Delta K = 12$ MPa$\sqrt{m}$ in the 3Cr-1.5Mo steel weldments. C(T) specimens were cut from appropriate locations in the weldment to contain the HAZ perpendicular to the direction of crack growth. A load ratio $R = 0.05$ was used and the loads were continuously adjusted using computer control in order to maintain the required constant ΔK. As an indication of the variation of tensile properties through the HAZ regions, Vickers micro-hardness

traverses were performed on appropriately cut and polished sections in the regions of interest. Tensile tests were also conducted on 6.4 mm diameter specimens of 32 mm gauge length, machined from selected locations in the weldment.

2.3. RESULTS

To facilitate comparison with other ferrous alloys, values of the fatigue threshold ΔK_{TH} for the pressure vessel steels assessed in the present study are plotted as a function of yield strength in Figure 2.1, and indicate the characteristic trend of decreasing thresholds with increasing strength [8,17]. Detailed results for the three classes of alloys investigated are described in the following sections.

Table I. Chemical Composition (wt-%) of Alloys Investigated.

Material	C	Mn	Si	Ni	Cr	Mo	P	S	Cu	V
3Cr-1.5Mo-.2V	0.14	0.49	0.22	0.50	2.95	1.50	.006	.003	-	.21
3Cr-1.5Mo	0.15	0.51	0.25	0.55	3.03	1.52	.012	.003	.10	-
JSW	0.14	0.45	-	0.18	3.06	1.00	.007	.009	-	.29
A387-2-22	0.12	0.42	0.25	0.14	2.48	1.06	.013	.020	.16	-
A542-2	0.14	0.44	0.22	0.61	2.28	0.92	.010	.010	-	-
A542-3	0.12	0.45	0.21	0.11	2.28	1.05	.014	.015	.12	-
A533B-2	0.25	1.29	0.16	0.63	0.07	0.42	.010	.007	-	-

Table II. Ambient Temperature Mechanical Properties.

Material	Yield Strength (MPa)	UTS (MPa)	Redn Area (%)	K_{Ic} ($MPa\sqrt{m}$)	K_{Iscc} (H_2 gas) ($MPa\sqrt{m}$)
3Cr-1.5Mo-0.2V	676	821	74	-	-
3Cr-1.5Mo	555	717	73	479	-
JSW	503	621	72	228	-
A387-2-22	290	500	76	286	80
A542-2	759	820	56	-	80
A542-3	500	610	77	295	85
A533B-2	648	767	73	217	-

Table III. Heat Treatment and Microstructure.

Material	Heat Treatment	Microstructure
3Cr-1.5Mo-.2V	slow cooled/tempered	100% bainite
3Cr-1.5Mo	slow cooled/tempered	100% bainite
JSW	slow cooled/tempered	100% bainite
A387-2-22	normalized/tempered	60-90% bainite/40-10% ferrite
A542-2	quench and tempered	100% martensite
A542-3	quench and tempered	100% bainite
A533B-2	oil quenched/tempered	100% martensite

Table IV. Hydrogen Exposure Schedules.

Material	Condition	Exposure			Code
		Time (hours)	Temp. (°C)	Pressure (MPa)	
3Cr-1.5Mo-.2V	severe	1000	600	17.2	SE
3Cr-1.5Mo	severe	1000	600	17.2	SE
JSW	severe	1000	600	17.2	SE
A387-2-22	severe	1000	550	13.8	SE
A387-2-22	unexposed	1000	550	(molten salt)	UE
A533B	unexposed	-	-	-	UE
	light	72	550	13.8	LE
	normal	240	550	17.2	NE
	severe	1000	550 +	13.8	
		96	600	17.2	SE
	very severe	1000	550 +	13.8	
		480	600	17.2	VSE

2.3.1. Exposure to Gaseous Hydrogen (Hydrogen Embrittlement)

2.25Cr-1Mo Steels: The fatigue crack propagation behavior of A387-2-22, A542-3 and A542-2 steels, showing the typical influence of dry gaseous hydrogen and moist air at a frequency of 50 Hz and load ratios between 0.05 and 0.80, are presented in Figures 2.2, 2.3 and 2.4, respectively (7,9,14). Crack propagation rates appear to exhibit two distinct regimes of hydrogen-affected cracking, characteristic of the test environment, frequency, load ratio and stress intensity range (12).

Behavior appears to result from a mutual competition between hydrogen embrittlement mechanisms, which accelerate growth rates, and resulting crack tip shielding, which retards growth rates (15). At low growth rates below $\sim 10^{-8}$ m/cycle, near-threshold crack propagation rates are observed to be decreased significantly, and threshold ΔK_{TH} values increased, for tests in moist air environments compared to gaseous hydrogen. This difference is particularly marked at low load ratios where, in moist air, fretting oxidation between crack surfaces promotes extensive corrosion deposits, causing enhanced crack tip shielding from premature contact across the crack (oxide-induced crack closure) (6,7). This is the primary reason for slower growth rates in air compared to gaseous hydrogen below 10^{-8} m/cycle. Moreover, it is the reason such differences diminish at high load ratios where closure, from the wedging effect of the oxide, becomes less effective due to the larger crack tip opening displacements, similar to behavior observed in other dehumidified environments, including argon (6), helium (7), oxygen (9,14) and silicone/paraffin oils (18). From the high R results in the present alloys, the accelerating influence of gaseous hydrogen on crack growth rates can be seen to be quite small when subjected to high frequency loading in the near-threshold regime.

With increasing growth rates the difference in crack propagation behavior for the moist air and hydrogen environments initially decreases. However, above typically 10^{-6} m/cycle, a hydrogen embrittlement contribution to cracking may be observed, particularly at lower frequencies, resulting in a sharp enhancement in propagation rates compared to behavior in moist air (12). This effect, which is concurrent with a fracture mode transition to predominantly intergranular cracking, has been shown to be promoted by decreasing frequency and increasing load ratio (12). Such hydrogen-assisted cracking at lower frequencies is particularly evident in higher strength pressure vessel steels (Figures 2.2 and 2.3), which generally are more susceptible to embrittlement.

2.3.2. Prior Exposure to High Pressure Hydrogen (Hydrogen Attack)

2.25Cr-1Mo Steels: Fatigue crack propagation behavior of A387-2-22 in the heat treated (HT) and severely hydrogen exposed (SE) conditions is shown in Figure 2.5 for load ratios of 0.05 and 0.75 (13). In addition, results are given for a thermally exposed condition (UE) having the same 1000 hour/550°C thermal treatment as the SE condition. Although behavior is almost identical at higher growth rates, below $\sim 10^{-9}$ m/cycle (R = 0.05), near-threshold growth rates are apparently reduced and threshold ΔK_{TH} values increased following hydrogen exposure. This somewhat surprising result can again be traced to the offsetting effects of hydrogen damage and shielding, in the latter case from enhanced crack closure from thermal softening, although the degree of hydrogen damage in this steel was clearly slight. The fact that behavior in the hydrogen exposed SE condition is essentially identical to that in the unexposed UE condition is consistent with this notion.

3Cr-Mo Steels: The effect of hydrogen attack damage on the room temperature Charpy V-notch toughness ductile to brittle transition curve for the 3Cr-1.5Mo steel is presented in Figure 2.6. With the introduction of microstructural damage, the steel shows a reduction in the upper shelf energy of approximately 10 to 50 J, and a shift of 50°C in the 54 J (40 ft-lb) transition temperature to higher temperatures. It has, however, been previously reported that the increase in the transition temperature may in part be attributed to temper embrittlement which may occur due to the elevated temperatures associated with the hydrogen attack procedure (3). The effects of prior exposure to hydrogen attack is further illustrated by the $J_R(\Delta a)$ resistance curves for the unattacked and attacked 3Cr-1.5Mo steel shown in Figure 2.7. (Note that the unexpectedly high toughness of the unattacked material has resulted in the test specimen not being in compliance with the ASTM standard thickness requirement. The result is, however, included for comparative purposes.) Although a reduction in fracture toughness K_{Ic} from 480 MPa$\sqrt{m}$, in the unattacked condition, to 339 MPa$\sqrt{m}$ in the attacked material is apparent, this reduction is comparatively minor compared to the devastating effect of a similar exposure on the toughness of steels containing less stable iron and alloy carbides. Detailed studies of the effect of microstructural damage in these lower alloyed steels are reported in the following section and in Chapter 3.

Fatigue crack propagation behavior and corresponding closure data for the 3Cr-1.5Mo-0.2V, 3Cr-1.5Mo and JSW steels prior to and following prolonged high temperature/high pressure hydrogen exposure are shown in Figures 2.8(a) and (b), respectively. These alloys, like 2.25Cr-1Mo steels, offer good resistance to hydrogen attack due to the precipitation of stable alloy carbides, such as V_4C_3, $M_{23}C_6$, and MgC (3,19). Although the effect of prior hydrogen damage is apparent under monotonic loading, behavior under cyclic loading shows little influence. This again may be explained by the offsetting effects of microstructural damage which results in a reduced intrinsic toughness, and crack tip shielding which promotes the extrinsic toughness component. In the present example, only the effect of increased crack deflection due to the hydrogen damage is apparent under monotonic loading conditions. However, under cyclic loading, the associated additional increase in the potent roughness induced closure mechanism is also apparent and results in a marked increase in the extrinsic shielding component.

Mn-Mo-Ni Steels: The hydrogen attack resistance of the lower alloyed Mn-Mo-Ni steels, such as nuclear pressure vessel grade A533B, tends to be quite low as the primary hardening carbides, i.e., Fe_3C and Mo_2C, are relatively unstable in the presence of hydrogen (20,21). Correspondingly, such steels generally show a dramatic degradation in strength, ductility and toughness properties following damage from hydrogen attack. This takes the form of weakened prior austenite grain boundaries from the nucleation and coalescence of small methane gas bubbles, formed by the reaction of ingressed

hydrogen with carbon in the steel (21). Reductions in K_{Ic} fracture toughness values from over 200 MPa$\sqrt{m}$ to less than 30 MPa$\sqrt{m}$ with the severe damage following prolonged exposure are not uncommon (20).

The corresponding effect of hydrogen attack on fatigue crack propagation, however, is surprisingly minor, once more owing to the offsetting influence of crack tip shielding. This is illustrated in Figure 2.9 for progressive degrees of hydrogen damage in A533B-2 steel following prior hydrogen exposure (13). Growth rates above $\sim 10^{-9}$ m/cycle are essentially identical except where severe degrees of attack, in the SE and VSE structures, result in accelerated crack extension rates as instability is approached. Conversely, at lower growth rates below $\sim 10^{-9}$ m/cycle, crack propagation rates and threshold ΔK_{TH} values are only marginally influenced by very severe prior hydrogen damage.

Such behavior has been found to be associated with significantly enhanced crack tip shielding in the severely damaged structures, as shown by the back-face strain measurements of the closure stress intensity K_{cl} in Figure 2.10 (13). Metallographic studies of the fatigue crack profiles clearly show that this shielding originates from crack deflection and resultant crack closure induced by fracture surface asperity contact (roughness-induced crack closure), caused by the tortuous morphology of the crack path as it follows severely damaged prior austenite grain boundaries. Such shielding is sufficient to offset the accelerating effect of the environmental damage (13,20). A more detailed analysis of the above results, in which quantitative variations in both intrinsic and extrinsic toughness are estimated, is presented in Chapter 3.

2.3.3. Influence of Load Ratio

High mean stresses superimposed upon cyclic loading generally cause an increase in fatigue crack propagation rates, principally from a reduction in shielding from crack closure (12). This is shown by results (6,10) for A387-2-22 and A542-3 steels tested in moist air at 50 Hz (Figures 2.11(a) and 2.12(a)). Consistent with explanations based on closure, above $\sim 10^{-8}$ m/cycle, growth rates in moist air are largely insensitive to load ratio, while at near-threshold levels, growth rates are markedly increased, and threshold ΔK_{TH} values decreased, with increasing R. The latter observation, however, is only apparent up to a critical load ratio where the closure stress intensity becomes comparable with K_{min} (6). At higher load ratios, closure effects become minimal with the result that near-threshold growth rates and ΔK_{TH} values become independent of R.

Behavior as a function of load ratio is essentially similar in dry gaseous hydrogen, as illustrated in Figures 2.11(b) and 2.12(b) (6,10). However, above $\sim 10^{-8}$ m/cycle where differences in crack growth rates in air and hydrogen at low frequencies are due primarily to hydrogen embrittlement, increasing the load ratio causes the sharp acceleration from hydrogen-assisted cracking to occur at lower

values of K_{max} (12). Conversely, at near-threshold levels where slower growth rates in moist air result primarily from enhanced oxide-induced closure, increasing the load ratio minimizes the closure contributions such that behavior in air and hydrogen (at high frequencies) becomes comparable.

2.3.4. Influence of Cyclic Frequency

The role of cyclic frequency in influencing fatigue crack propagation rates in A542-3 2.25Cr-1Mo steel at near-threshold levels is shown in Figure 2.13 (22). Data are presented, from tests in moist air at R = 0.1, for frequencies ranging from 1 to 500 Hz (sine wave), and show that the slowest growth rates, and highest thresholds, occur at intermediate frequencies. Based on back-face strain K_{cl} measurements and Auger spectroscopy of fracture surface corrosion deposits, such behavior could be rationalized in terms of contributions from oxide-induced crack closure, as the variation in ΔK_{TH} values was found to relate directly to changes in the magnitude of ΔK_{eff} and in the thickness of crack surface oxide films.

2.3.5. Influence of Temperature

Temperature effects on fatigue crack propagation in A387-2-22 steel over the range 28 to 110°C (R = 0.05) are shown in Figure 2.14 for atmospheres of moist air and dry gaseous hydrogen environments (14). Results show that crack growth rates are increased, and ΔK_{TH} values decreased, with increasing temperature, although the effect of temperature diminishes at higher growth rates. Results at 110°C in hydrogen gas, however, oppose this trend and show significantly higher threshold values.

2.3.6. Influence of Weld and HAZ Microstructures

Results illustrating the fatigue crack propagation behavior of A387-2-22 steel in the base, heat-affected-zone (HAZ) and weld metal regions of a thick section weldment are shown in Figure 2.15, again for environments of moist air and dry gaseous hydrogen (R = 0.05 and 0.8) (14). Microstructural characteristics and strength levels for the three weldment regions are listed in Table V.

Results show that, whereas crack propagation behavior is similar at high load ratios and above $\sim 10^{-8}$ m/cycle, at near-threshold levels (R = 0.05) growth rates are faster, and threshold ΔK_{TH} values lower, in the weld metal and particularly HAZ regions, compared to the base plate. Such results are again consistent with concepts of crack tip shielding as the extent of crack closure (from both the plasticity-induced and roughness-induced mechanisms) becomes diminished in the higher strength weld and HAZ regions, where the finer microstructures promote a more linear crack path (14).

Table V. Microstructural Characterization and Yield Strength of SA387-2-22 Steel Weldment.

Region in Weldment	Microstructure	Yield Strength (MPa)
Base plate	ferrite-bainite	345
HAZ	fine bainite	476
Weld metal	coarse bainite	423

Optical examination of Nital etched sections of the baseplate, HAZ and weldmetal of the 3Cr-1.5Mo and JSW steel weldments revealed an apparently ferrite-free, fully bainitic microstructure in all regions. Typical representative optical micrographs of the HAZ regions are presented in Figures 2.16(a) and 2.17(a). The finer bainitic microstructure of the HAZ is clearly apparent compared to the coarser microstructure of the baseplate and weldmetal. The results of the microhardness traverse through this region are presented in Figures 2.16(b) and 2.17(b). In both weldments a microstructurally "hard zone" exists in the HAZ immediately adjacent to the fusion boundary. In the JSW weldment, a "soft zone" comprising an over-tempered microstructure was apparent on the opposite side of the HAZ (Figure 2.17). Microstructural characteristics and yield strengths of the 3Cr-1.5Mo steel weldment are summarized in Table VI.

Table VI. Microstructural Characterization and Yield Strength of 3Cr-1.5Mo Steel Weldment.

Region in Weldment	Microstructure	Damage Condition	Yield Strength (MPa)
Base plate	coarse bainite	unattacked	558
		attacked	544
HAZ	fine bainite	unattacked	
Weld metal	coarse bainite	unattacked	840
		attacked	772

The fatigue crack propagation behavior of the 3Cr-1.5Mo steel weldmetal in both the unattacked and attacked condition was found to

be essentially similar to the data for the 3Cr-Mo steels presented in Figure 2.8. Growth rates were marginally increased, and threshold ΔK_{TH} values slightly decreased in the hydrogen attacked weldmetal compared to the unattacked material. The fatigue crack growth rate at constant $\Delta K = 12$ MPa$\sqrt{m}$ for cracks growing perpendicularly through the HAZ region, both prior to and after hydrogen attack, are shown in Figures 2.18(a) and 2.18(b), respectively. The crack growth rate is plotted as a function of distance through the HAZ. Both sets of data indicate increased crack propagation rates in the HAZ regions. The minimal effect of prior microstructural damage from exposure to hydrogen attack on the growth rates observed is apparent by comparison of the data in Figure 2.18. Crack growth rates in the base plate material are relatively unaffected, and those in the weldmetal marginally increased, by the prior exposure to hydrogen attack as was confirmed by separate tests in these regions.

Results of the fatigue crack growth rate and corresponding crack closure level through the HAZ at a constant $\Delta K = 10$ MPa$\sqrt{m}$ in the JSW steel weldment is shown in Figure 2.19(a) and 2.19(b), respectively. Similar to the 3Cr-1.5Mo steel weldment, the maximum growth rate was observed in the HAZ region. Results are rationalized in terms of crack tip shielding from crack closure associated with reductions in both plasticity- and roughness-induced mechanisms. Plasticity-induced closure, favored by a lower flow stress, is diminished in the higher strength HAZ region. In addition, the finer microstructure of the HAZ promotes a more linear crack path and hence reduces the roughness-induced closure contribution. Such behavior is consistent with the closure data presented in Figure 2.19(b) which indicates a decreased level of closure in the HAZ region.

2.4. DISCUSSION

In the present study, existing fatigue crack propagation data of several commercial steels for hydrogen-containing thick-section pressure vessel applications has been reviewed and compared with new data on three recent 3Cr-Mo pressure vessel steels. Specifically, the respective roles of hydrogen embrittlement, hydrogen attack, load ratio, temperature, cyclic frequency and weldment microstructure have been examined in several classes of 2.25Cr-1Mo, 3Cr-Mo, and Mn-Mo-Ni ferritic, bainitic and martensitic steels, tested in ambient pressure gaseous hydrogen and moist air environments. In general, optimum crack growth resistance is found in the lowest strength microstructures, such that when normalized with respect to strength level, these steels show largely similar growth rate behavior. The more leanly alloyed Mn-Mo-Ni steels, however, are less resistant to damage from hydrogen attack.

Environmentally-assisted crack growth is observed above $\sim 10^{-8}$ m/cycle, particularly at lower frequencies, in both hydrogen embrittled and prior hydrogen attacked microstructures. At lower

growth rates, however, approaching near-threshold levels, behavior has been considered in terms of the mutual competition of environmental damage, which promotes crack growth, and the resultant crack tip shielding, which retards it. Such shielding leads to a reduction in crack extension rates, not by increasing the resistance of the microstructure (i.e., by intrinsic toughening mechanisms) but rather by decreasing the local "driving force" actually experienced at the crack tip (i.e., by extrinsic toughening mechanisms). Salient micro-mechanisms of shielding, pertinent to the present material/environment systems, are illustrated schematically in Figure 2.20.

In moist environments, shielding from the wedging action of corrosion debris (oxide-induced closure (6-8)) acts to offset the accelerating effect of corrosion fatigue processes (active path corrosion and hydrogen embrittlement) (Figure 2.20(a)). Accordingly, near-threshold growth rates in 2.25Cr-1Mo steels are found to be much slower in water or wet gaseous hydrogen compared to dry gaseous hydrogen (10). Similarly, growth rates are faster at room temperature in dry air or dry oxygen, compared to moist air (9,14). A more general form of shielding, however, arises where environmental processes lead to a change in crack path (Figure 2.20(b)). In the present work, the steels subjected to extensive damage from prior hydrogen attack, which show markedly reduced toughnesses, are found to show only marginally accelerated fatigue crack growth rates at near-threshold levels. Here, the grain boundary damage from methane bubble formation results in a meandering intergranular crack path, which promotes shielding from both reduced local stress intensities due to deflection out of the Mode I plane (23) and, more importantly, from the resultant crack closure from fracture surface asperity contact (roughness-induced closure (24-26)). Similar mutually offsetting effects of roughness-induced closure and environmental damage have been reported for hydrogen embrittled low alloy steels following hydrogen charging (27).

Although as yet unproven, crack propagation in steels subjected to **in situ** high pressure/high temperature hydrogen environments may be impeded by an additional form of shielding, induced by preferential hydrogen attack damage in the form of creep-enhanced methane bubble formation in the process zone at the crack tip (Figure 2.20(d)). Since the bubble formation involves dilation, the elastic constraint of surrounding material will result in the crack growing into a region of compression, analogous to microcrack toughening in ceramics and rocks (28). Thus, with respect to hydrogen attack, it is conceivable that **prior** hydrogen exposure, where bubbles nucleate throughout the microstructure, may well be more damaging than **in situ** exposure, where bubbles form preferentially at the tip, since zone shielding will only occur in the latter case. (Estimates of the extent of extrinsic shielding from **in situ** exposure to hydrogen attack are presented in Appendix I of Chapter 3.)

Finally, although the deflection, wedge and zone shielding

mechanisms described provide a potent means in these steels to restrict the accelerating influence of aggressive hydrogen-containing environments, it must be remembered that in particular situations the effect of these mechanisms can become muted. Related studies in steels and aluminum alloys have shown that this can arise with superimposed high mean stresses (7-12), following compressive overloads (29), and in the presence of physically small cracks (<1 mm) or cracks emanating from notches (15,30-32). In these instances, care must be taken in interpreting and applying conventional laboratory data (i.e., based on "long crack", low R, compact tension testing) to predict service behavior, as the role of crack tip shielding may differ markedly between test and service conditions.

2.5. SUMMARY AND CONCLUSIONS

Based on a study of fatigue crack propagation behavior in a series of 2.25Cr-1Mo, 3Cr-Mo and Mn-Mo-Ni pressure vessel steels suitable for thick-section, high pressure hydrogen service, data have been provided on the variation in growth rates (da/dN) with nominal stress intensity range (ΔK) as a function of environmental damage (hydrogen embrittlement and hydrogen attack), temperature, weld/HAZ microstructure, load ratio and frequency. It is reasoned that at near-threshold levels, where the majority of fatigue life is spent, environmental contributions to crack growth under cyclic loading may be offset by a local reduction in the "crack driving force" from mechanisms of crack tip shielding. Primary micro-mechanisms of such shielding relevant to the present steels have been identified, in terms of crack deflection and crack closure induced by corrosion debris, fracture surface asperties, and void-induced dilation in the elastically-constrained crack tip process zone.

2.6. REFERENCES

1. R. W. Swindeman, R. D. Thomas, R. K. Nanstad and C. J. Long, "Assessment of the Need for an Advanced High-Strength Cr-Mo Steel for Construction of Third-Generation Gasifier Pressure Vessels," Report No. ORNL/TM-8873, Oak Ridge National Laboratory, Oak Ridge, TN, Oct. 1984.

2. R. M. Horn, R. J. Kar, V. F. Zackay and E. R. Parker, J. Mat. for Energ. Syst., 1, 77, 1979.

3. R. O. Ritchie, E. R. Parker, P. N. Spencer and J. A. Todd, J. Mat. for Energ. Syst., 6, 151, 1984.

4. G. S. Sangdahl and M. Semchyshen, eds., Application of 2.25Cr-1Mo Steel for Thick Wall Pressure Vessels, ASTM STP 755, Amer. Soc. Test. and Matl., Philadelphia, PA, 1982.

5. D. P. Edmonds, T. B. Cox, J. F. King, R. K. Nanstad, R. A. Swift and R. M. Swindeman, "Evaluation of 3Cr-1.5Mo-0.1V Steel as a Gasifier Pressure Vessel Alloy," Report No. ORNL-6106, Oak Ridge National Laboratory, Oak Ridge, TN, Jan. 1985.

6. R. O. Ritchie, C. M. Moss and S. Suresh, J. Eng. Mat. Tech., Trans. ASME, Series H, 102, 293, 1980.

7. S. Suresh, G. F. Zamiski and R. O. Ritchie, Metall. Trans. A, 12A, 1435, 1981.

8. S. Suresh, G. F. Zamiski and R. O. Ritchie, Application of 2.25Cr-1Mo Steel for Thick Wall Pressure Vessels, ASTM STP 755, Amer. Soc. Test. and Matl., Philadelphia, PA, 49, 1982.

9. R. O. Ritchie, Fatigue Thresholds, Proc. First Intl. Conf., J. Backlund, A. F. Blom, and C. J. Beevers, eds., EMAS Ltd., Warley, U.K., 1, 503, 1982.

10. S. Suresh and R. O. Ritchie, Eng. Fract. Mech., 18, 785, 1983.

11. R. O. Ritchie, S. Suresh and P. K. Liaw Ultrasonic Fatigue, J. M. Wells, O. Buck, L. D. Roth, and J. K. Tien, eds., TMS-AIME, Warrendale, PA, 443, 1982.

12. S. Suresh and R. O. Ritchie, Metal Science, 16, 529, 1982.

13. R. D. Pendse and R. O. Ritchie, Metall. Trans. A, 16A, 1491, 1985.

14. R. Fuquen-Molano and R. O. Ritchie, "Investigation of Factors Affecting Near-Threshold Fatigue Crack Growth in Low Alloy Pressure Vessel Steels," Final Report to DOE on Contract No. EX-

76-A-01-2295 TO 40, Massachusetts Institute of Technology, Cambridge, MA, 1981.

15. S. Suresh and R. O. Ritchie, Fatigue Crack Growth Thresholds Concepts, D. L. Davidson and S. Suresh, eds., TMS-AIME, Warrendale, PA, 227, 1984.

16. R. O. Ritchie, R. H. Dauskardt and R. M. Cannon, Lawrence Berkeley Report No. LBL-20656, University of California, Berkeley, CA, 1987.

17. R. O. Ritchie, Int. Metals Reviews, 20, 205, 1979.

18. J.-L. Tzou, C. H. Hseuh, A. G. Evans and R. O. Ritchie, Acta Metall., 33, 117, 1985.

19. T. George, E. R. Parker and R. O. Ritchie, Mat. Sci. Tech., 1, 198, 1985.

20. R. D. Pendse and R. O. Ritchie, Modeling Environmental Effects on Crack Initiation and Propagation, R. H. Jones and W. W. Gerberich, eds., TMS-AIME, Warrendale, PA, 1986.

21. P. Shewmon, Mat. Sci. Tech., 1, 2, 1985.

22. V. B. Dutta and R. O. Ritchie, unpub ished work, Lawrence Berkeley Laboratory, University of California, Berkeley, 1983.

23. S. Suresh, Metall. Trans. A, 14A, 2375, 1983.

24. N. Walker and C. J. Beevers, Fat. Eng. Mat. Struct., 1, 135, 1979.

25. K. Minakawa and A. J. McEvily, Scripta Met., 15, 633, 1981.

26. S. Suresh and R. O. Ritchie, Metall. Trans. A, 13A, 1627, 1982.

27. K. A. Esaklul, A. Wright and W. W. Gerberich, Scripta Met., 17, 1073, 1983.

28. D. R. Clarke, Comm. Amer. Cer. Soc., 67, C-15, 1984.

29. E. Zaiken and R. O. Ritchie, Eng. Fract. Mech., 22, 35, 1985.

30. J. Schijve, Fatigue Thresholds, Proc. First Int. Conf., J. Bachlund, A. F. Blom, and C. J. Beevers, eds., EMAS Ltd., Warley, U.K., 2, 881, 1982.

31. S. Suresh and R. O. Ritchie, Int. Metals Reviews, 29, 445, 1984.

32. R. O. Ritchie and J. Lankford, Mater. Sci. Eng., 84, 11-16, 1986.

2.7. FIGURES

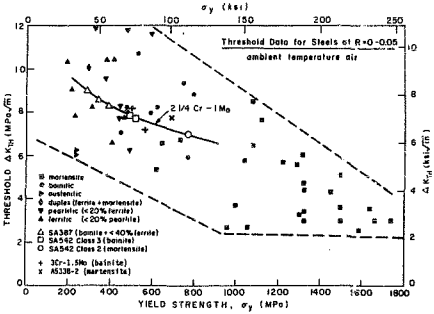


Figure 2.1 Variation of fatigue threshold stress intensity range, ΔK_{TH} (at low load ratios), as a function of yield strength for a wide range of steels (8), showing results for the 2.25Cr-1Mo, 3Cr-Mo, and Mn-Mo-Ni steels in the present study.

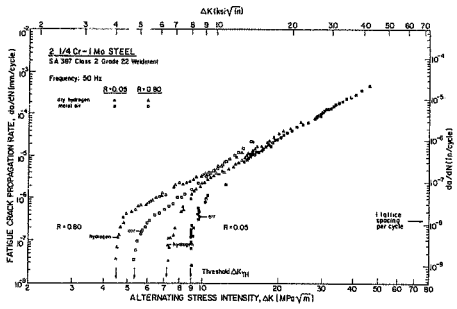


Figure 2.2 Fatigue crack propagation behavior of a normalized (thick-section) ferritic-bainitic 2.25Cr-1Mo steel (A387-2-22), showing the influence of moist air and dry gaseous hydrogen (138 kPa) environments at R=0.05 and 0.80 (6,14).

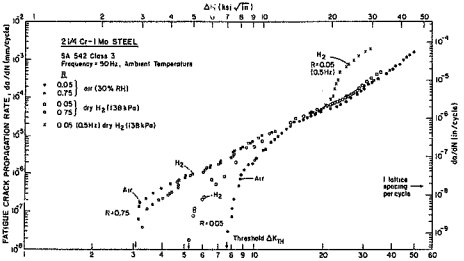


Figure 2.3 Fatigue crack propagation behavior of a quenched and tempered (thick-section) fully bainitic 2.25Cr-1Mo steel (A542-3), showing the influence of moist air and dry gaseous hydrogen (138 kPa) environments at low and high frequencies at R=0.05 and 0.75 (7,12).

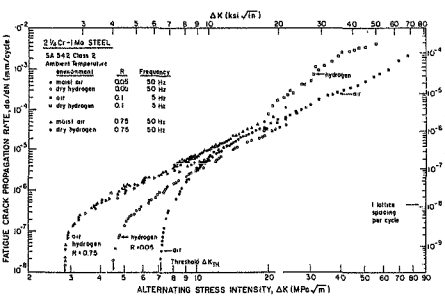


Figure 2.4 Fatigue crack propagation behavior of a quenched and tempered fully martensitic 2.25Cr-1Mo steel (A542-2), showing the influence of moist air and dry gaseous hydrogen (138 kPa) environments at low and high frequencies at R=0.05 and 0.75 (7,9,12).

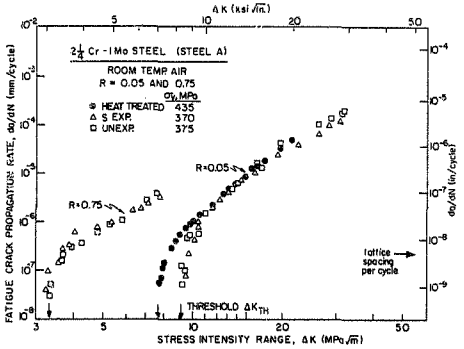


Figure 2.5 Fatigue crack propagation behavior for a normalized *ferritic-bainitic* 2.25Cr-1Mo steel (A387-2-22), at load ratios of R = 0.05 and 0.75, showing influence of prior 1000 hr exposure to gaseous hydrogen at 13.8 MPa pressure (550°C). Results are for heat treated (HT), hydrogen attacked (SE), and unexposed (UE) conditions (13).

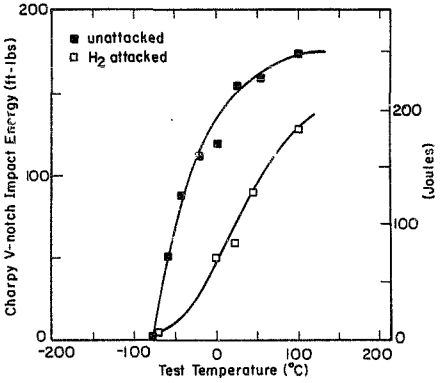


Figure 2.6 Charpy V-notch transition curves for the 3Cr-1.5Mo steel showing the effect of microstructural damage from exposure to high temperature/pressure hydrogen environments.

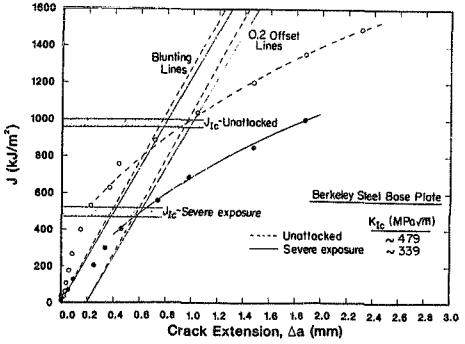


Figure 2.7 $J_R(\Delta a)$ resistance curves for the 3Cr-1.^{5}Mo steel indicating the effect of hydrogen attack on the crack initiation toughness J_{Ic}.

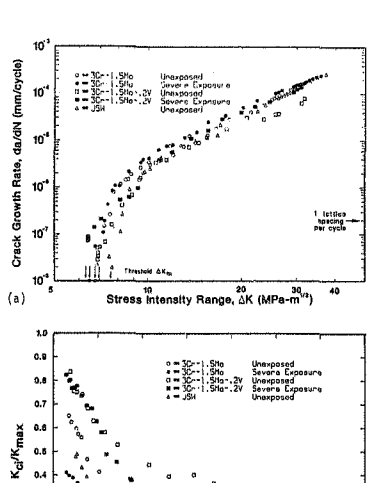


Figure 2.8 Fatigue crack propagation behavior of slow-cooled fully bainitic 3Cr-Mo steels (3Cr-1.5Mo, 3Cr-1.5Mo-0.2V, and JSW steel), showing influence of prior 1000 hr exposure to gaseous hydrogen at 17.2 MPa pressure (600°C) on (a) crack growth rates, and (b) crack closure.

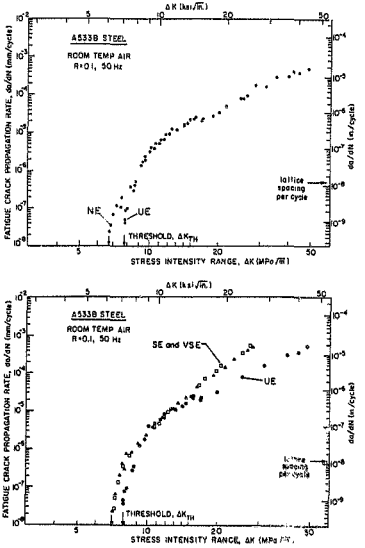


Figure 2.9 Fatigue crack propagation behavior of a bainitic Mn-Mo-Ni nuclear pressure vessel steel (A533B-2), tested at R = 0.10, showing influence of prior damage from hydrogen attack. Results are given for the unexposed (UE) condition, and following 240 hr (NE), 1096 hr (SE), and 1480 hr (VSE) exposures to gaseous hydrogen at 13.8-17.2 MPa pressure (550-600°C) (13,20).

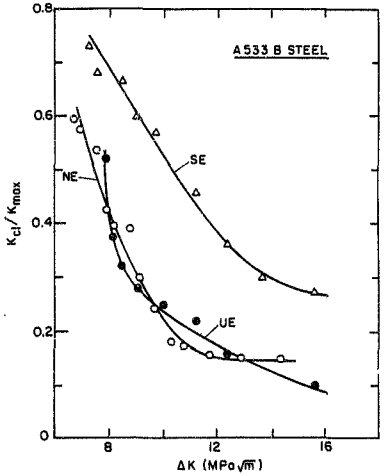


Figure 2.10 Experimentally measured variation in fatigue crack closure in A533B-2 steel corresponding to growth rate data in Figure 2.9. Results show the ratio of closure to maximum stress intensity, K_{cl}/K_{max}, as a function of ΔK, and indicate higher levels of crack tip shielding in the severely hydrogen attack damage microstructure (SE) (13).

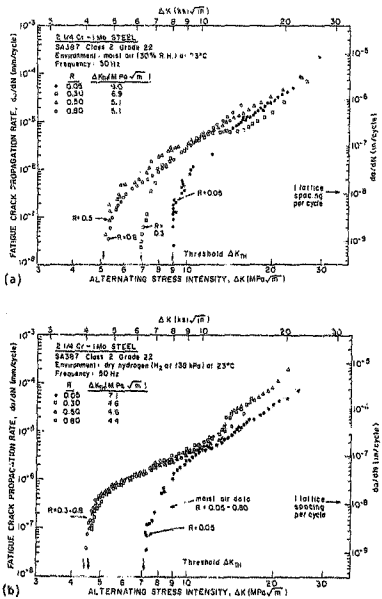


Figure 2.11 Fatigue crack propagation behavior of normalized 2.25Cr-1Mo A387-2-22 steel tested in (a) moist air and (b) dry gaseous hydrogen (138 kPa) at high frequencies (50 Hz), showing the influence of load ratio for R varying between 0.05 and 0.80 (6,14).

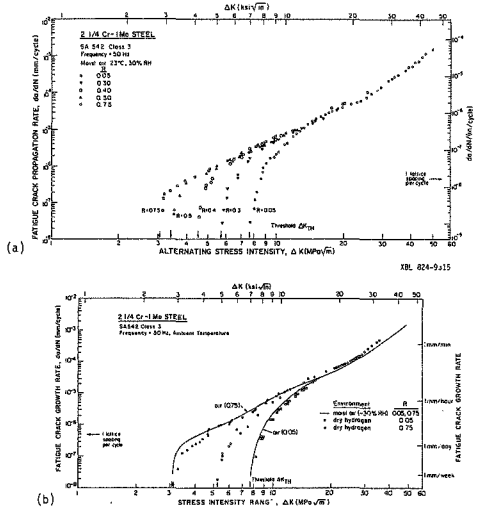


Figure 2.12 Fatigue crack propagation behavior of quenched and tempered 2.25Cr-1Mo A542-3 steel tested in (a) moist air and (b) dry gaseous hydrogen (138 kPa) at high frequencies (50 Hz), showing the influence of load ratio for R varying between 0.05 and 0.75 (7,10).

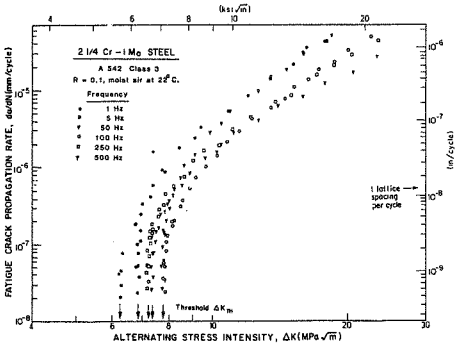


Figure 2.13 Influence of cyclic frequency (1 to 500 Hz) on fatigue crack propagation behavior in quenched and tempered fully bainitic 2.25Cr-1Mo steel (A542-3), tested at R = 0.1 in moist air (22).

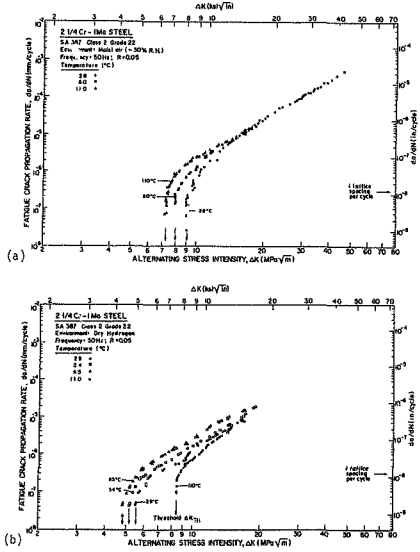


Figure 2.14 Influence of temperature (28-110°C) on fatigue crack propagation behavior in normalized ferritic-bainitic 2.25Cr-1Mo steel (A387-2-22), tested at R = 0.05 in (a) moist air and (b) dry gaseous hydrogen (138 kPa) (14).

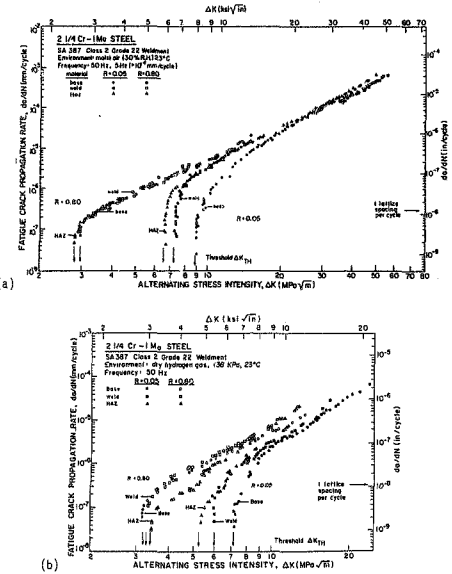


Figure 2.15 Fatigue crack propagation behavior in a thick-section weldment of normalized 2.25Cr-1Mo stee, (A387-2-22), showing comparison of growth rates in base plate, HAZ and weld metal microstructures in (a) moist air and (b) dry gaseous hydrogen (138 kPa) at R = 0.05 and 0.80 (`4).

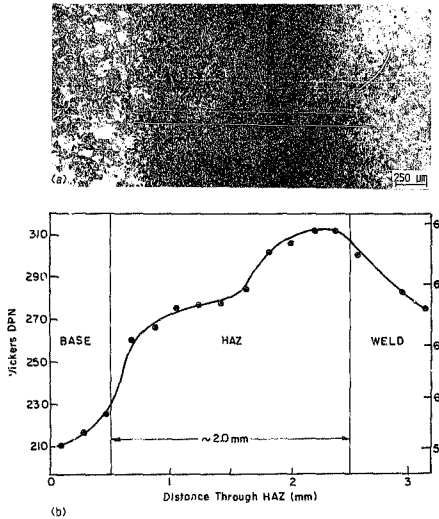


Figure 2.16 Microstructural and hardness characterization of the HAZ in the 3Cr-1.5Mo steel weldment, showing (a) a representative optical micrograph indicating the finer bainitic microstructure of the HAZ, and (b) the Vickers microhardness variation through the same region.

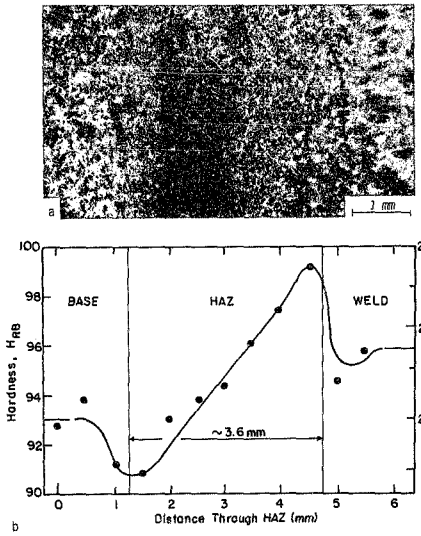


Figure 2.17 Microstructural and hardness characterization of the HAZ in the JSW steel weldment, showing (a) a representative optical micrograph indicating the finer bainitic microstructure of the HAZ, and (b) the Vickers microhardness variation through the same region.

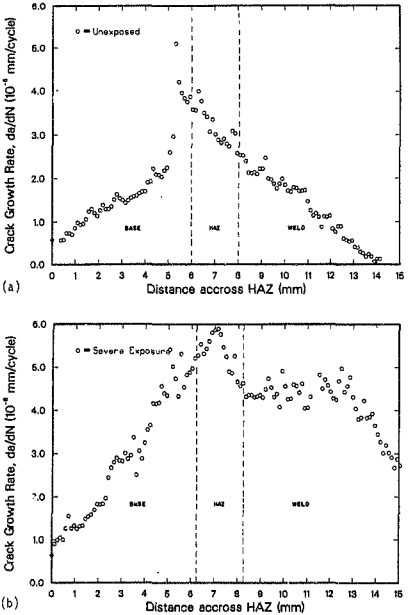


Figure 2.18 Fatigue crack propagation behavior of the 3Cr-1.5Mo steel weldment showing the variation of the crack growth rate (da/dN) as a function of the distance through the HAZ at a constant $\Delta K = 12$ NPa$\sqrt{m}$, both (a) prior to, and (b) after the introduction of microstructural damage associated with hydrogen attack.

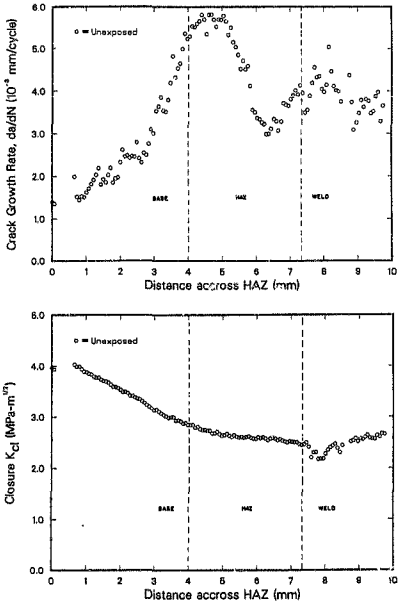


Figure 2.19 Fatigue crack propagation behavior of the JSW steel weldment showing (a) the variation of the crack growth rate (da/dN) as a function of the distance through the HAZ at a constant ΔK = 12 MPa$\sqrt{m}$, and (b) the level of crack closure.

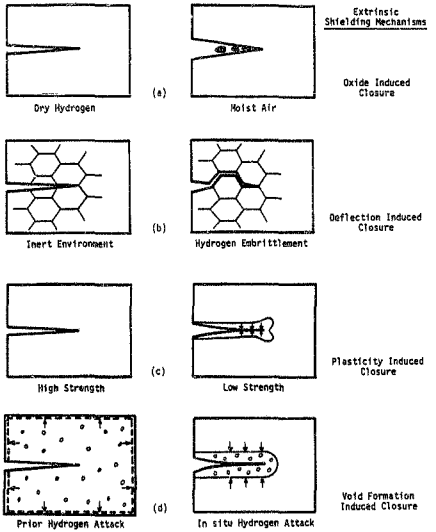


Figure 2.20 Schematic illustration of micro-mechanisms of crack tip shielding relevant to the present study, showing wedge shielding from (a) oxide-induced closure, and (b) deflection and roughness-induced closure, and zone shielding from (c) plasticity-induced closure and (d) from compressive zones around the crack due to the dilatant growth of methane bubbles (in situ hydrogen attack).

CHAPTER 3: EFFECTS OF PRE-EXISTING GRAIN BOUNDARY MICROVOID DISTRIBUTIONS ON FRACTURE TOUGHNESS AND FATIGUE CRACK GROWTH IN LOW ALLOY STEEL

ABSTRACT

The role of dispersions of pre-existing grain boundary microvoids is investigated in fracture toughness and fatigue crack propagation behavior in a low alloy steel. Microvoid damage is achieved by prior exposure of the steel to gaseous hydrogen atmospheres at high temperatures and pressures, where carbon within the steel reacts with ingressed hydrogen to nucleate methane bubbles along prior austenite grain boundaries (hydrogen attack). It is shown that, whereas the crack initiation and crack growth toughness (i.e., K_{IC} and the tearing modulus) are severely degraded, even for comparatively mild degrees of microvoid damage, rates of sub-critical crack growth by fatigue remain relatively unaffected. Such results are interpreted in terms of a mutual competition between microstructural damage generated by the grain boundary microvoids, which promotes crack growth by lowering the intrinsic resistance of the microstructure, and the resulting tortuous crack paths, which extrinsically retard crack growth at low stress intensities by lowering the local crack tip "driving force" (crack tip shielding). As shielding effects are minimized at high stress intensities, the degradation in intrinsic toughness is related to changes in ductility by means of a stress-modified critical strain model for ductile fracture, where the presence of small microvoid clusters is shown to promote coalescence through the easier onset of plastic strain localization. Fatigue behavior, conversely, is dominated by extrinsic shielding mechanisms and is modeled in terms of two-dimensional models of crack deflection and roughness-induced crack closure.

3.1. INTRODUCTION

Microstructural damage in the form of micro-porosity is frequently encountered in materials. Mechanically, it typically results in a degradation of tensile and impact toughness properties, and is most often associated with the formation of a dispersion of microvoids at phase or grain boundaries. Such void formation may arise from improper fabrication of the material; e.g., shrinkage porosity in alloys exhibiting a wide solidification range (1) and gas bubble formation due to insufficient out-gassing prior to casting

(2), or may be associated with the particular operating environment; e.g., creep cavitation at high temperatures (3), severe radiation-induced damage (4), or from hydrogen attack in materials exposed to high temperature, high pressure hydrogen environments (5).

Mechanistically, the introduction of a dispersion of microvoids may be expected to produce significant effects on crack propagation behavior under both monotonic and cyclic loading conditions. Under monotonic loading, where crack extension occurs at a high stress intensity comparable to that of the fracture toughness, K_{Ic}, the presence of a **pre-existing** microvoid dispersion in ductile materials will encourage the onset of plastic strain localization (6) and consequently lower the critical fracture strain associated with ductile fracture. This results in a reduced **intrinsic** resistance to crack growth (i.e., lower intrinsic toughness[1]). Where microvoids form preferentially at the crack tip, e.g., with **in situ** creep or hydrogen attack damage, this may be offset by mild **extrinsic toughening** from the constraint of the resulting zone of dilated material surrounding the crack (see Appendix I). The significance of the latter effect, however, which is analogous to microcrack toughening in brittle materials (9), is generally small in ductile materials due to their high intrinsic toughness (8).

Conversely, where crack extension may proceed at a lower "driving force", e.g., under cyclic loading, the effect of a dispersion of microvoids may involve significant contributions from both extrinsic and intrinsic effects (10). In addition to the extrinsic toughening from a surrounding dilated zone of microvoids, more potent crack tip shielding can develop in fatigue from crack deflection and, in particular, fatigue crack closure. Crack closure, which results in a reduction in the stress intensity range, ΔK_{eff}, locally experienced at the crack tip, is in general developed by the presence of cyclic plasticity in the wake of the tip (11), or more importantly at low crack tip opening displacements by the wedging action of corrosion debris (12-14), fracture surface asperities (15-17), or fluid pressure within the crack (18). Thus, the possible accelerating effect of a dispersion of grain boundary microvoids may be offset by shielding from enhanced crack deflection and roughness-induced crack closure, as the fatigue crack attempts to follow a more tortuous intergranular path (e.g., ref. 10).

The objective of the present work is to investigate the effects of a dispersion of pre-existing grain boundary microvoids, of

---

[1]The distinction is drawn here between **intrinsic** toughening, where crack growth is impeded by mechanisms which increase the microstructural resistance to crack advance, and **extrinsic** toughening, where crack growth is impeded by mechanisms which **locally** reduce the "crack driving force", i.e., through crack tip shielding (7,8).

progressively increasing size and density, on crack propagation under monotonic and cyclic loading. Specifically, studies are performed on a low alloy steel, where grain boundary microvoid dispersions are achieved by prior exposure to high temperature/high pressure gaseous hydrogen environments through **hydrogen attack**, i.e., from nucleation, growth and eventual coalescence of small methane bubbles, formed by the chemical reaction of ingressed hydrogen with carbon in the steel. It is found that **intrinsic toughness** is severely degraded by the presence of the microvoids, essentially by promoting the earlier onset of incipient plastic strain localization of the intervoid matrix, a process exacerbated by the presence of small microvoid clusters in the highly triaxial stress fields ahead of the crack tip. In marked contrast, the rates of fatigue crack growth are largely unchanged, observations which are attributed to the mutual competition between microstructural damage, which accelerates crack advance, and the resulting crack tip shielding, which acts to retard it.

3.2. EXPERIMENTAL PROCEDURES

The alloy investigated was a Mn-Mo-Ni nuclear pressure vessel steel, ASTM A533B Class 2, of composition shown in Table I. Air induction melted ingots, prepared by Lukens Steel Co., were first upset forged and cross-rolled to 35 mm thick plate, before austenitizing at 1000°C (1 h), oil quenching, and tempering at 650°C (4 h).

Table I. Composition of A533B Class 2 Steel in Wt Pct

C	Mn	Mo	Ni	Cr	Si	P	S	Al	Fe
0.25	1.29	0.42	0.63	0.07	0.16	0.010	0.007	0.02	bal

Controlled distributions of pre-existing grain boundary microvoids were obtained through the process of hydrogen attack, involving the nucleation of methane filled bubbles at grain boundary carbides, and their progressive coarsening with prolonged exposure to high pressure/high temperature hydrogen gas (5). Resistance to such damage is a prime function of the carbon activity, and hence of the thermodynamic stability of the precipitated carbides (5,19,20). The low alloy A533B steel, hardened primarily by the relatively unstable Fe_3C carbide, was therefore particularly susceptible to attack.

Exposure to gaseous hydrogen was performed on oversized blanks of heat-treated material in high pressure autoclaves for various combinations of time, temperature and hydrogen pressure. Exposure sequences were selected to achieve increasing microvoid size and density. As listed in Table II, increasing degrees of exposure up to 1480 hr at temperatures between 550 and 600°C were utilized for hydrogen pressures in the range 14 to 17 MPa (2000 to 2500 psi). To avoid confusion with hydrogen embrittlement effects, this was followed by a 4 h 'baking' treatment at 180°C to minimize the amount of residual hydrogen within the steel.

Table II. Specific Heat Treatment Schedules for Hydrogen Exposure

Condition	Exposure	Code
Unexposed	-	UE
Light Exposure	72 hr at 550°C in 13.8 MPa hydrogen	LE
Normal Exposure	240 hr at 550°C in 17.2 MPa hydrogen	NE
Severe Exposure	1000 hr at 550°C in 13.8 MPa hydrogen + 96 hr at 600°C in 17.2 MPa hydrogen	SE
Very Severe Exposure	1000 hr at 550°C in 13.8 MPa hydrogen + 480 hr at 600°C in 17.2 MPa hydrogen	VSE

Early stages of hydrogen damage were monitored by density measurements of the degree of swelling, and are noted in terms of the percent change in specific volume, ΔV.

Fracture toughness tests to determine $J_R(\Delta a)$ resistance curves were performed on 25 pct (V-notched) side-grooved, 25 mm thick, compact C(T) test pieces, machined in both L-T and S-T orientations. Crack initiation toughness was estimated from J_{Ic} ($= K_{Ic}^2/E'$) values, in accordance with ASTM Standard E813-83, where E' ($= E/(1 - \nu^2)$) is the effective Young's modulus for plane strain and ν is Poisson's ratio. Crack growth toughness was estimated from the slope of the resistance curve (dJ/da), and is expressed in terms of the tearing modulus ($T_J = E/\sigma_0^2 \cdot dJ/da$), in accordance with the proposed ASTM standard (21), where σ_0 is the flow stress. In all tests, unloading compliance methods were used to monitor crack extension.

Rates of fatigue crack propagation down to 10^{-11} m/cycle were measured under manual load shedding conditions using 10 mm thick C(T) specimens, machined in the L-T orientation. Tests were conducted at 50 Hz in room temperature air (22°C, 45 pct relative humidity) at a load ratio ($R = K_{min}/K_{max}$) of 0.1, using electrical potential

methods to monitor crack length and back-face strain compliance methods to assess the extent of crack closure (described in ref. 7).

To provide detailed characterization of the basic microstructures and the dispersion and size of grain boundary microvoids, suitably polished sections, thin foils and carbon extraction replicas were examined using optical, scanning (SEM) and transmission electron (TEM) microscopy. In addition, carbon extraction techniques were employed to study the cavitated *intergranular fracture surfaces at higher magnification using a* Phillips 400 scanning transmission electron microscope (STEM), equipped with an energy dispersive X-ray attachment.

3.3. RESULTS

3.3.1. Characterization of Microstructural Damage

Prior to hydrogen exposure, the unattacked microstructure (hereafter designated UE) was tempered martensite (Figure 3.1). Observation at higher magnification (Figure 3.2) revealed coarse M_3C (Fe rich + Mo,Ni,Mn,Cr) carbides ($\sim$ 0.23 μm in diameter) along prior *austenite grain and martensite lath boundaries, and fine needle*-shaped intralath M_2C (Mo rich + Fe) carbides ($\sim$ 0.08 μm in diameter) in the matrix. Room temperature mechanical properties are listed in Table III.

Following light exposure (72 h at 550°C in 14 MPa hydrogen, termed LE), the microstructure remained essentially unchanged, although thin foil TEM revealed that the prior austenite grain boundaries were decorated with bubbles of diameter $\sim$ 0.1 μm and spacing $\sim$ 0.6 μm (Table IV). Indicative of incubation stages of attack, mechanical properties, with the exception of toughness and ductility, were largely unaffected (Table III).

With more prolonged exposure (240 h) in 17 MPa hydrogen (termed NE), coarsening of the carbide dispersions, typical of extended tempering, was apparent. Mean M_3C and M_2C carbide sizes were 0.30 μm and 0.12 μm, respectively. Methane bubbles, of mean diameter 0.6 μm and spacing $\sim$ 1 μm, could be readily detected in micrographs (Figure 3.1). Gas pressure inside the bubbles was estimated to be of the order of 20 MPa (10). With such damage, considerable swelling and decarburization were apparent, leading to a 30 pct loss in strength and a twentyfold reduction in ductility.

Detailed metallographic examination of the early stages of void formation (LE and NE) indicated that, although all boundaries exhibited a relatively uniform background volume fraction of voids, small clusters of microvoids formed preferentially on boundaries parallel to the rolling plane, with a mean cluster spacing of $\sim$ 20 μm. Initial cluster sizes of a few void spacings in the LE condition

Table III. Room Temperature Mechanical Properties Before and After Exposure

Condition	Yield Strength (MPa)	UTS (MPa)	Redn Area (pct)	True Fract Strain	Charpy Impact Toughness DBTT (°C)	Charpy Impact Toughness Upper Shelf (J)	J_{Ic} (kJ/m)	K_{Ic} (MPa$\sqrt{m}$)	T_R
UE (L-T)	648	767	73.0	1.27	-150	142	208	217	162
(S-T)	630	750	70.0	1.20	-	-	170	197	47
LE (L-T)	632	748	53.0	0.87	-	-	84	138	14
(S-T)	630	770	12.5	0.13	-	-	-	58	1
NE (L-T)	440	505	3.5	0.05	-	-	-	57	4
(S-T)	440	-	-	0.04	-	-	-	30	1
SE (L-T)	242	315	5.0	-	+10	20	-	-	-
VSE (L-T)	240	310	5.5	-	-	-	-	-	-

Table IV. Microstructural Characterization of Hydrogen Damage

Condition	Carbon Content (wt pct)	Volume Change, ΔV (pct)	Bubble Size (μm)	Bubble Spacing (μm)	Grain Boundary Vol. Fract. V_{fgb}
UE	0.250				
LE	0.230	0.10	0.1	0.6	0.02
NE	0.090	2.10	0.6	1.1	0.25
SE	0.018	2.52	0.9	-	0.30
VSE	0.009	2.50	0.9	-	0.30

grew rapidly with increasing exposure, eventually to form fissures via coalescence of grain boundary bubbles. Incipient fissure formation is shown in Figure 3.3 for the NE condition.

Scanning electron microscopy of the fracture surfaces following hydrogen exposure indicated an intergranular fibrous or cavitated

fracture surface along prior austenite grain boundaries, as shown for the NE structure in Figure 3.4(a,b). Close examination revealed the presence of small particles in the fracture surface dimples, which, using extraction replicas in the STEM, EDS and electron diffraction techniques, were found to be primarily Fe-rich M_3C carbides (Figure 3.4(c,d)). This finding lends support to the notion of carbide-assisted nucleation of bubbles, and furthermore suggests that the presence of carbon in the form of the less stable Fe_3C carbide is not rate limiting in the earlier stages of hydrogen attack.

With prolonged exposure in 17 MPa hydrogen at 600°C (termed SE), structures showed severe damage indicative of rapid attack stages, i.e., considerable swelling ($\Delta V \sim 2.5$ pct), extensive decarburization, and a microstructure devoid of its martensitic lath character. Such damage resulted in a twofold loss in strength and dramatic decreases in ductility (by a factor of 15) and impact toughness (ductile-to-brittle transition temperature, DBTT, increased by $\sim$ 160°C) (Table III). Further increases in exposure time in 17 MPa hydrogen (VSE condition) resulted in no further changes in properties, indicating that the damage had reached saturation.

3.3.2. Effects of Pre-Existing Microvoids on Fracture Toughness

The effects of grain boundary microvoid formation on crack initiation (K_{IC}, J_{IC}) and growth (T_R) toughness are illustrated by the $J_R(\Delta a)$ resistance curves for both orientations in Figure 3.5; data are listed in Table III. It is apparent that progressively increasing degrees of microvoid size and density in the LE and NE structures have a devastating influence on fracture toughness. K_{IC} values were decreased by factors of up to 6 by prolonged exposure in the NE structure, the S-T orientations consistently showing the lower toughness. The effect on crack growth toughness was even more striking; tearing modulus T_R values were reduced by factors of over 40 in the NE structure, compared to behavior in the unexposed condition.

Fractographically, unattacked surfaces consisted largely of primary void growth around MnS inclusions, linked by inclined shear band regions (void sheets) containing numerous smaller oblate voids formed at carbides (Figure 3.6). With light hydrogen exposure (LE), there was additional evidence of intergranular facets, decorated with closely spaced 0.1 μm diameter spherical bubbles. Following more extensive exposure (NE), fracture surfaces comprised 100 pct cavitated intergranular facets, the bubbles being somewhat larger ($\sim$ 0.6 μm) and more widely spaced (Table IV). The grain boundary volume fraction of voids, estimated using the method outlined in Appendix II, varied from $\sim$ 2 pct in the LE structure to $\sim$ 30 pct in the SE and VSE structures.

The marked reduction in toughness with progressively coarser microvoids appears to be consistent with a change in the ductile

fracture mechanism, specifically related to easier plastic strain localization in structures containing methane bubbles. In unattacked and mildly attacked microstructures containing few pre-existing microvoids, failure occurs in the classical ductile manner by primary void growth and coalescence. In attacked microstructures containing extensive microvoid dispersions, conversely, failure involves almost immediate coalescence of pre-existing voids along grain boundaries.

To provide a first order micro-mechanical model for such behavior, we consider a stress-modified critical strain criterion for crack initiation by ductile fracture (22-24). Using a constitutive law for A533B steel of the form:

$$\frac{\bar{\varepsilon}_p}{\varepsilon_o} = \alpha\left(\frac{\bar{\sigma}}{\sigma_o}\right)^n \tag{3.1}$$

where the work hardening exponent, n, is of order 10, we assume first that the Hutchinson, Rice and Rosengren (HRR) nonlinear elastic singular field (25,26) dominates the stresses and deformations in the vicinity of the stationary crack tip over the microstructural regions of interest:

$$\frac{\varepsilon_{ij}}{\varepsilon_o} = \alpha\left\{\frac{J}{\alpha\,\sigma_o\,\varepsilon_o\,I_n\,r}\right\}^{\frac{n}{n+1}} \tilde{\varepsilon}_{ij}(n,\theta) \tag{3.2}$$

σ_o and ε_o are the flow stress and strain, respectively, $\bar{\sigma}$ and $\bar{\varepsilon}_p$ are the equivalent stress and plastic strain, respectively, α is a material constant of order unity, J is the path independent integral, I_n is an integration constant weakly dependent on n, and $\tilde{\varepsilon}_{ij}$ is a dimensionless angular function of n and θ. Values of the latter two functions are documented elsewhere (27), although for the present steel, I_n is approximately 4.5.

To model failure, we consider the onset of ductile crack extension, at $J = J_{Ic}$, where the local equivalent plastic strain $\bar{\varepsilon}_p$ exceeds a critical fracture strain or ductility $\bar{\varepsilon}_p^*(\sigma/\bar{\sigma})$ over a characteristic microstructural dimension l_o^*, comparable with the mean spacing of the void initiating particles (Figure 3.7). The ductility, however, is specific to the appropriate degree of triaxiality in the region of the crack tip, defined in terms of the ratio of hydrostatic stress, σ, to equivalent stress, $\bar{\sigma}$ (23). Following Ritchie et al. (24), this implies that, for failure primarily by microvoid coalescence in a material with high n, the fracture toughness can be expressed as:

$$J_{Ic} \propto \sigma_o \bar{\varepsilon}_f^* \ell_o^* \tag{3.3}$$

where the constant of proportionality is given by $I_n/\tilde{\varepsilon}_{1j}$. Restated in terms of stress intensity, this gives (24):

$$K_{Ic} \propto (E' \sigma_o \bar{\varepsilon}_f^* \ell_o^*)^{0.5} \tag{3.4}$$

where the constant of proportionality is now $(I_n/\tilde{\varepsilon}_{1j})^{0.5}$.

Evaluation of Eqn. 3.4 involves estimating $\bar{\varepsilon}_f^*$ and l_o^*. In previous analyses (23,24), $\bar{\varepsilon}_f^*$ has been estimated experimentally by determining the change in ductility with stress-state, using circumferentially-notched tensile specimens for example, and choosing $\bar{\varepsilon}_f^*$ as the value of ductility appropriate to the stress-state in the vicinity of the crack tip. In the absence of such data, this local fracture strain (relevant to a fracture process region within a couple of crack tip displacements from a blunting crack tip) can be estimated (28) from the uniaxial fracture strains listed in Table III using Rice and Tracey's analysis (29) for the rate of void expansion in a triaxial stress field. This approach assumes, for a fixed distribution of particles, that the fracture strain at initiation, i.e., at the point of void impingement, is given by:

$$\bar{\varepsilon}_f^* \propto \frac{\ln(d_p/D_p)}{0.28 \exp(1.5\ \sigma/\bar{\sigma})} \tag{3.5}$$

where D_p and d_p are the mean void diameter and spacing, respectively. Using Eqn. 3.5, critical fracture strains ahead of the crack tip (where from Rice and Johnson's (30) and McMeeking's (31) blunting solutions, $\sigma/\bar{\sigma}$ is around unity) will thus be on the order of 2.9 times smaller than the uniaxial fracture strains (where $\sigma/\bar{\sigma}$ is 0.3). Estimated values of the crack tip fracture strains are listed in Table V. Also listed are the critical crack tip opening displacements, computed from $\delta_t \approx 0.5 J/\sigma_o$ (31). Note that the effect of methane gas pressure on void growth has been ignored, as the internal pressures are small compared to the crack tip stresses.

Using such values of $\bar{\varepsilon}_f^*$ and taking $\tilde{\varepsilon}_{1j}$ to be of order 0.1 for initial coalescence between 0 and 45 degrees to the crack plane (such that $(I_n/\tilde{\varepsilon}_{1j})^{0.5}$ is of order 6 to 7), Eqn. 3.4 is evaluated in Figure 3.8 by plotting the observed toughness versus $(E'\bar{\varepsilon}_f^* \bar{\sigma}_o)^{0.5}$. Two separate lineal segments are apparent. At high toughnesses, failure

Table V. Crack Tip Parameters at Fracture

Condition	K_{Ic} (MPa$\sqrt{m}$)	δ_t (μm)	$\bar{\varepsilon}_f^*$	$(r/\delta_t)^*$	l_o^* (μm)
UE (L-T)	217	150	0.44	0.43	60[a]
(S-T)	197	130	0.42	0.51	69[a]
LE (L-T)	138	70	0.30	0.79	55[a]
(S-T)	58	10	0.05	2.10	11[b]
NE (L-T)	57	15	0.02	3.00	33[b]
(S-T)	30	5	0.01	3.00	15[b]

[a]from Eqn. 3.6, [b]from Eqn. 3.4.

occurs by the primary growth of voids, until coalescence by shear localization along smaller microvoids around carbide particles. In this regime, a characteristic distance of order 60 μm is apparent. Although primary inclusion spacings in A533B may be somewhat smaller, this figure is not unreasonable for the spacing of the largest, active void-initiating particles. However, it is in contrast with behavior in ultrahigh strength steels where the larger inclusions play a relatively minor role (for fracture ahead of a sharp crack) and characteristic dimensions are on the order of the spacing of the finer carbide particles (32). Thus in lightly exposed structures, the role of the secondary network of pre-existing microvoids is to provide a mechanism for earlier localization, and hence for earlier coalescence, of the primary voids, resulting in reduced toughness.

At low toughnesses, failures consist almost entirely of coalesced bubbles along grain boundaries with little or no primary void growth. The characteristic distance in this regime appears to be significantly smaller and similar to the void cluster spacing of 20 μm (Figure 3.3). Here the relatively high volume fraction of pre-existing microvoids reduces the local ductility such that direct coalescence can occur very rapidly via localization of plastic strain within the cavitated grain boundary regions. As negligible plastic strains are required for either the initiation or growth of voids, significant reductions in toughness become apparent.

Such toughness behavior is essentially consistent with the analysis of Needleman and Tvergaard (33) for ductile fracture in materials containing both inclusions and sub-micron carbides. Here a reduction in the critical strain to initiate voids in the carbides led to substantially lower local failure strains within the high triaxial stress field of a crack tip, due to accelerated coalescence

of primary voids. However, in the present study, the dramatic difference in toughness of the two orientations of the LE condition *does not appear* to be consistent with the small difference in grain boundary microvoid volume fractions observed. In addition, the role of the microvoid clusters in providing active ductile fracture initiating sites requires closer examination.

The latter questions are examined in terms of the recent analyses of plastic flow localization due to non-uniform void distributions in an elastic-plastic solid. Specifically, the investigation of Ohno and Hutchinson (34) into the role of void clusters in promoting incipient flow localization in a voided solid, from the two extremes of a bifurcation solution, obtained for a **uniform** void distribution (35), to *the substantially reduced critical* strain from localization predicted by infinite band calculations of a **non-uniform** void distribution (36,37), is considered. In these analyses, it is shown that even small microvoid clusters may induce premature localization and hence reduced ductility, particularly at the high stress triaxialities typical of the region close to a crack tip in plane strain.

Although Ohno and Hutchinson's model (34) is based on a simplified representation of a voided material, the ductility results may nevertheless be employed in the stress-modified critical strain model to provide some indication of the trends in fracture toughness that may be expected from a uniform void dispersion and the subsequent influence of void clusters. In particular, the critical strain at *incipient plastic strain localization*, $(\varepsilon_Z^{\infty})_{cr}$, predicted by ref. 34 (for a stress state given by $\sigma_r = \sigma_\theta = \sigma_z/4$), is used in place of $\bar{\varepsilon}_f^*$ in Eqn. 3.4.

By first considering a uniform void distribution (*bifurcation* solution) and a constant characteristic distance, the decay in intrinsic toughness with increasing uniform void volume fraction, as *predicted from* Eqn. 3.4, *is shown* by the solid line in Figure 3.9. It is apparent that, for initial microvoid formation (volume fractions up to 0.01), marked decreases in toughness of up to 25 pct are to be expected, although further degradation requires fairly large increments in the void volume fraction (as *the function becomes* asymptotic with the horizontal axis). By considering the additional effect of small microvoid clusters, the Hutchinson and Ohno (34) *analysis* (*uniform* band solution) predicts significantly diminished toughness values, as shown by the upper broken line in Figure 3.9. The lower broken line indicates the synergistic effect of an increase in the microvoid cluster volume fraction and a decrease in the characteristic distance l_o^* *from 70 μm to 20 μm, similar to that* obtained in the present study. It is immediately apparent that the dramatic decrease in critical ductility predicted with the development of microvoid clusters by this model (34) is reflected in a similar decrease in the intrinsic fracture toughness of the material.

From these considerations, it is apparent that the marked deterioration in intrinsic toughness with hydrogen attack damage can be rationalized by the increased volume fraction of pre-existing microvoids, and particularly small microvoid clusters, in the microstructure. Specifically, the significant difference in toughness of the LE structure in the L-T and S-T orientations is consistent with the location of the microvoid clusters; their effect is partially masked in the L-T orientation where the crack plane cuts vertically through them (Figure 3.10).

The stress-modified critical strain approach used above is appropriate provided the critical fracture processes occur in a region dominated by HRR fields, typically $2\delta_t < r < 8\delta_t$. However, estimates of the crack opening displacements, δ_t, which range from 70 to 150 μm in the high toughness regime to 5 to 15 μm in the low toughness regime (Table V), indicate that HRR fields may not be dominant in all cases over the scale of fracture events. At low toughnesses, the characteristic distance is generally larger than δ_t, such that the HRR fields would be expected to be controlling. *However, in the high toughness regime, the characteristic distances* are well within two crack tip displacements of the crack tip, implying that the critical events occur in the finite strain field governed by the blunting solutions (30,31). Following Lee et al. (32), the critical strain local failure criterion now gives the ductile fracture toughness as:

$$K_{Ic} \sim \left\{ \frac{2\sigma_o E' l_o^*}{(r/\delta_t)^*} \right\}^{0.5} \qquad (3.6)$$

where $(r/\delta_t)^*$ is the critical value of (r/δ_t) corresponding to $\bar{\varepsilon}_p = \bar{\varepsilon}_f^*$ in the finite strain region. Estimates of $(r/\delta_t)^*$ were obtained using the strain distributions of Rice and Johnson (30) and McMeeking (31), for initial void coalescence between 0 and 45 degrees to the crack plane. *By setting* $r = l_o^*$, *characteristic distances were* recalculated for microstructures in the higher toughness regime and these are listed in Table V along with their respective $(r/\delta_t)^*$ values. It is apparent that whereas the finite strain criterion is more appropriate to microscopic failure processes in the unexposed and lightly damaged microstructures, values of l_o^* remain of the order of 60 μm.

3.3.3. Effest of Pre-Existing Microvoids on Fatigue Crack Propagation

The corresponding effect of progressively coarser distributions

of grain boundary microvoids on crack growth under cyclic loading is shown in Figure 3.11, with threshold data listed in Table VI (11). By comparing behavior after prolonged hydrogen exposure (NE structure) with the unexposed structure (UE) in Figure 3.11(a), pre-existing microvoids can be seen to have little influence on fatigue crack propagation. Above $\sim 10^{-9}$ m/cycle, growth rates were identical, whereas at near-threshold levels below $\sim 10^{-9}$ m/cycle, there was a marginal increase in growth rates in the damaged microstructures. Surprisingly, this minimal reduction in fatigue resistance with increasing grain boundary microvoid formation was not accentuated with more severe degrees of damage in the SE and VSE microstructures, although above 10^{-8} m/cycle the latter structures do show accelerated propagation rates as K_{Ic} is approached (Figure 3.11(b)).

Table VI. Threshold Data for Hydrogen Attacked and Unattacked Steel Displaying Increasing Degrees of Microvoid Formation

Condition	Nominal ΔK_{TH} (MPa$\sqrt{m}$)	Maximum K_{cl}/K_{max}	Lineal Roughness*	Effective ΔK_{TH} (MPa$\sqrt{m}$)
UE	7.8	0.52	1.07	4.2
NE	6.8	0.59	1.05	3.1
SE	7.0	0.73	1.52	2.1
VSE	7.0	0.70	1.51	2.3

*Ratio of total crack length to projected length on plane of maximum tensile stress.

Fractography associated with the fatigue failures at near-threshold and higher growth rates is shown in Figure 3.12. Fatigue surfaces are similar in the UE and NE structures and are predominantly transgranular. In the more heavily attacked SE and VSE structures, however, surfaces become predominantly intergranular, with grain boundary surfaces decorated with evidence of methane bubbles. Such cavitated intergranular facets persist to near-threshold levels where there is additional evidence of abrasion, presumably due to the softened condition of the heavily damaged decarburized material.

The lack of a marked deterioration in fatigue crack propagation resistance with increasing grain boundary microvoid formation is at first sight unexpected, particularly in light of the dramatic effect on toughness described above.[2] However, crack closure measurements (Figure 3.13) revealed that much higher closure stress intensities

[2]At high stress intensity ranges, severely damaged structures do show accelerated growth rates. This is a direct consequence of the decreased toughness, since growth rates are invariably enhanced as K_{max} approaches K_{Ic} (38,39). In damage-tolerant lifetime calculations, however, this regime generally has little impact on overall life as crack extension rates are too rapid.

were developed in voided structures, compared to undamaged and LE conditions. Since crack closure provides a potent mechanism for "shielding" the crack from the full applied "driving force", the effective stress intensity range actually experienced at the crack tip must be reduced in severely voided structures, and this will act to offset the decreased **intrinsic** resistance of these microstructures to crack growth (40). This is apparent by examining values of the effective stress intensity range at the threshold, defined in terms of $\Delta K_{eff} = K_{max} - K_{cl}$, where $K_{cl} \geq K_{min}$ (Table VI). Once closure is subtracted out, crack growth resistance decreases progressively with increasing damage.

Mechanistically, the enhanced crack shielding in severely damaged structures can be attributed to several factors. First, the extensive decarburization causes marked softening, which can promote contributions to closure induced by cyclic plasticity (40). Moreover, lower strength steels tend to suffer more abrasion between fracture surfaces (41), which results in excess fretting debris and *hence more oxide-induced closure* (12-14). However, the principal factor responsible for "shielding" in heavily grain boundary voided structures is associated with a substantially rougher crack path morphology where the crack follows an irregular path around cavitated grain boundaries (10). This is illustrated in Figure 3.14 by an extremely tortuous crack path profile for the SE structure (lineal roughness of over 1.5) in contrast to comparatively linear paths in the UE and NE structures (lineal roughnesses of order unity).

The extrinsic benefits of a meandering crack path are: (i) growth rates are effectively reduced by the longer path length of the crack, (ii) the local stress intensity at the tip is reduced (from crack deflection mechanics) whenever the crack deviates from the plane of maximum tensile stress (42), and most importantly (iii) the local stress intensity range is reduced due to enhanced roughness-induced crack closure (15-17) from mismatch between geometrically irregular crack surfaces, aided by inelastic crack tip shear displacements (43).

Modeling the influence of microstructural damage from a grain boundary microvoid dispersion on cyclic crack extension is complicated by opposing intrinsic and extrinsic factors. In the present work, changes in crack growth resistance are estimated by comparing predictions of the extent of crack tip shielding with the

observed growth rate behavior. The latter predictions are achieved by considering current models for the respective roles of crack deflection (42) and consequent roughness-induced crack closure (17).

Based on a linear elastic two-dimensional model, Suresh (42) has recently examined the role of crack deflection in fatigue, both in terms of the reductions in local stress intensity and the apparent changes in crack propagation rates. For an idealized non-planar crack with periodic tilts through an angle φ, where the lengths of the linear and deflected segments are c and s, respectively, the effective stress intensity range, Δk, in each segment of span $(c + s)$ was shown to be related to the nominal far-field ΔK through the expression:

$$\Delta k \approx \left(\frac{c \cos^2(\varphi/2) + s}{c + s} \right) \Delta K \qquad (3.7)$$

with the apparent average propagation rate of the tilted crack (da/dN), due to the longer crack path, given by:

$$\left(\frac{da}{dN}\right) \approx \left(\frac{c \cos\varphi + s}{c + s} \right) \left(\frac{da}{dN}\right)_L \qquad (3.8)$$

where $(da/dN)_L$ is the growth rate of the linear (undeflected) Mode I crack (42). Corresponding modeling for the fracture surface contact generated by the deflected crack has been analyzed by Suresh and Ritchie (17) using a simple, two-dimensional geometric model for roughness-induced crack closure. By assuming equal-sized fracture surface asperities, of height h and width w, the non-dimensional closure stress intensity at the point of first asperity contact on unloading is given by:

$$\frac{K_{cl}}{K_{max}} \approx \left(\frac{2\gamma X}{1 + 2\gamma X} \right)^{0.5} \qquad (3.9)$$

where γ is the non-dimensional surface roughness parameter, defined as (h/w), and X is the ratio of Mode II to Mode I inelastic crack tip

displacements.

Such considerations of crack tip shielding via crack deflection and closure are applied to the present crack growth rate behavior of the solid (UE) and voided (SE) microstructures in Figure 3.15. First, using the experimentally measured closure data in Figure 3.13, propagation rates are replotted in terms of an effective stress intensity range, ΔK_{eff}, in Figure 3.11(a), thereby demonstrating the significantly lower **intrinsic** crack growth resistance of the voided *microstructures once the extrinsic shielding effect is removed.* Second, the role of deflection is assessed by applying Eqns. 3.7 and 3.8 to such data, using the crack path profiles in Figure 3.14. The da/dN results for the UE condition are taken as a reference line with φ = 0 deg, since the crack path is essentially linear (see Figure 3.14). With deflection of such a linear crack, the reference fatigue crack growth curve will be shifted to the right to a degree dependent upon the deflection angle φ and c/(c + s). Quantifying the deflection of the crack path in the SE microstructure (e.g., from Figure 3.14(c)) is complex because the extent of crack path meandering is not uniform and tends to be more pronounced at lower growth rates. However, since the crack deflects along grain boundaries, c will be approximately a grain diameter. Accordingly, typical values of φ are taken between 45 and 75 deg with c/(c + s) between 0.25 and 0.50. Resulting predictions of the contribution from deflection only are plotted in Figure 3.15(b). Comparison of Figures 3.15(a) and 15(b) gives an indication of the relative contributions of crack deflection and crack closure to crack growth behavior in severely voided microstructures. It is apparent that *even with large degrees of deflection, the principal source of crack* tip shielding arises in this case from the crack closure effect, rather than any major reduction in ΔK from crack deflection mechanics.

The predictions of the reduction in local "crack driving force" clearly are first order, due to the simplicity and two dimensional nature of the models and the experimental uncertainty in closure measurements. However, the approach is instructive as it enables some ranking of the relative contributions of various shielding mechanisms. Moreover, it demonstrates the very potent effect of crack tip shielding in offsetting the lower intrinsic fracture resistance of extensively void damaged structures, where crack advance can proceed at low stress intensity levels.

3.4. CONCLUDING REMARKS

This study provides evidence that, although the presence of environmentally-induced grain boundary microvoids can markedly degrade fracture toughness, the role of such microstructural damage in accelerating sub-critical crack growth under cyclic loads may be considerably less potent. **This arises from a mutual competition of**

intrinsic mechanisms, where a dispersion of microvoids accelerates crack advance by lowering the intrinsic microstructural resistance to fracture, and extrinsic mechanisms, where the consequent generation of crack tip shielding through crack deflection and closure, retards crack advance by lowering the effective "driving force" actually experienced at the crack tip. In metals, the influence of the extrinsic mechanisms on fracture toughness is generally minimal due to their high intrinsic toughness, whereas during sub-critical crack growth, which occurs at much lower stress intensities, shielding can assume far greater relevance. In materials of low intrinsic toughness, conversely, extrinsic mechanisms provide major contributions to fracture toughness as well, as for example shown by the processes of transformation, microcrack and ligament toughening in ceramics (e.g., refs. 8 and 9).

Other examples of the offsetting effects of environmentally-induced microstructural damage and resulting shielding phenomena are the faster near-threshold propagation rates observed in lower strength steels tested in dry helium gas compared to moist air; a consequence of increased fretting oxidation debris formed on the crack surfaces, which promotes oxide-induced closure and offsets moisture-induced hydrogen-assisted growth in the air environment (12-14). Similarly, higher strength steels, cycled at near-threshold levels in ambient pressure gaseous hydrogen, often show far less evidence of accelerated growth rates, compared to hydrogen-assisted crack advance under monotonic loading, simply because the resulting hydrogen embrittlement gives rise to an intergranular crack path, which acts to retard cyclic crack growth through enhanced roughness-induced closure (44). Finally, closure due to the hydrodynamic action of fluids inside the crack may also counter the environmentally-assisted contribution to corrosion fatigue crack growth in liquid environments. Such fluid-induced closure has been demonstrated in viscous environments, and with sufficient fluid penetration into the crack can lead to values of K_{cl} approaching 50 pct of K_{max} (18).

3.5. CONCLUSIONS

Based on a study of the influence of grain boundary distributions of microvoids, induced by damage from hydrogen attack, on fracture toughness and fatigue crack propagation in a quenched and tempered ASTM A533B Class 2 steel, the following conclusions can be made.

1. The intrinsic toughness of A533B is severely degraded by the presence of pre-existing distributions of microvoids. Such microvoid distributions promote the earlier onset of plastic strain localization of the intervoid matrix, a process which is

exacerbated by the presence of small microvoid clusters in the highly triaxial stress state ahead of a crack tip.

2. Mild degrees of damage, in the form of 2 pct volume fraction of pre-existing grain boundary microvoids, led to 30 to 90 pct losses in ductility and to reductions in both crack initiation and crack growth fracture toughness, fracture occurring by classical primary void growth and coalescence.

3. Severe damage, in the form of 25 to 30 pct volume fraction of pre-existing grain boundary microvoids, led to abrupt losses in ductility (by > 90 pct), even larger reductions in crack initiation and growth toughness (by factors of $\sim$ 6 and $\sim$ 40, respectively), with fracture occurring by extensive intergranular cavitation.

4. Despite the dramatic influence on intrinsic toughness, even severe degrees of pre-existing microvoid damage had little apparent influence on fatigue crack propagation rates. In microstructures showing a 30 pct grain boundary volume fraction of microvoids, only minor increases in crack growth rates were observed below $\sim 10^{-9}$ m/cycle and above $\sim 10^{-7}$ m/cycle, and were associated with tortuous, cavitated intergranular fracture surfaces and large increases in measured crack closure.

5. The surprisingly small influence of distributions of pre-existing microvoids on fatigue crack propagation was attributed to a mutual competition between intergranular void-induced damage, which **accelerates** growth rates by **lowering** the intrinsic crack growth resistance of the microstructure, and crack shielding from the consequent deviation of the crack path, which acts to **decelerate** growth rates by extrinsically lowering the effective local "crack driving force". From simple models of crack deflection and roughness-induced closure, crack closure from the tortuous nature of the cavitated intergranular crack path is shown to provide the principal source of shielding.

3.6. REFERENCES

1. R. M. Brick, A. W. Pense and R. B. Gordon, Structure and Properties of Engineering Materials, 4th ed., McGraw-Hill, Inc., New York, NY, 1977.

2. E. Kato and A. Hirano. J. Iron Steel Inst. Japan, 69, 1425-32, 1985.

3. A. C. F. Cocks, Acta Met., 33, 129-37, 1985.

4. K. Miyakara, N. H. Packman and N. Igata, J. Nuclear Matls., 122, 624-8, 1984.

5. P. G. Shewmon, Metall. Trans. A, 7A, 279-86, 1976.

6. T. B. Cox and J. R. Low, Jr., Metall. Trans., 5, 1457-70, 1974.

7. R. O. Ritchie and W. Yu, in Small Fatigue Cracks, R. O. Ritchie and J. Lankford, eds., TMS-AIME, Warrendale, PA, 167-89, 1986.

8. R. O. Ritchie, R. H. Dauskardt and R. M. Cannon, Lawrence Berkeley Laboratory Report No. LBL-20656, University of California, Berkeley, Dec. 1985.

9. K. T. Faber and A. G. Evans, J. Amer. Cer. Soc., 67, 255-60, 1984.

10. R. D. Pendse and R. O. Ritchie, Metall. Trans. A, 16A, 1491-501, 1985.

11. W. Elber, Eng. Fract. Mech., 2, 37-45, 1970.

12. R. O. Ritchie, S. Suresh and C. M. Moss, J. Eng. Mater. Technol., Trans. ASME Series H, 102, 293-9, 1980.

13. A. T. Stewart, Eng. Fract. Mech., 13, 463-78, 1980.

14. S. Suresh, G. F. Zamiski and R. O. Ritchie, Metall. Trans. A, 12A, 1435-43, 1981.

15. N. Walker and C. J. Beevers, Fat. Eng. Mat. Struct., 1, 135-48, 1979.

16. K. Minakawa and A. J. McEvily, Scripta Met., 15, 633-6, 1981.

17. S. Suresh and R. O. Ritchie, Metall. Trans. A, 13A, 1627-31, 1982.

18. J.-L. Tzou, C. H. Hsueh, A. G. Evans and R. O. Ritchie, Acta Met., 33, 117-27, 1985.

19. O. W. Chung, J. A. Todd, J. K. Youngs and E. R. Parker, in Advanced Materials for Pressure Vessel Service with Hydrogen at High Temperatures and Pressures, M. Semchyshen, ed., ASME Vol. MPC-18, American Society for Mechanical Engineers, New York, NY, 25-52, 1982.

20. G. R. Odette and S. S. Vagarali, Metall. Trans. A, 13A, 299-303, 1982.

21. P. Albrecht, W. R. Andrews, J. P. Gudas, J. A. Joyce and F. J. Loss, J. Test. Eval., 10, 245-51, 1982.

22. F. A. McClintock, J. Applied Mech., Trans. ASME Series E, 35, 363-71, 1968.

23. A. C. Mackenzie, J. W. Hancock and D. K. Brown, Eng. Fract. Mech., 9, 167-88, 1977.

24. R. O. Ritchie, W. L. Server and R. A. Wullaert, Metall. Trans. A, 10A, 1557-70, 1979.

25. J. W. Hutchinson, J. Mech. Phys. Solids, 16, 13-31, 1968.

26. J. R. Rice and G. R. Rosengren, J. Mech. Phys. Solids, 16, 1-12, 1968.

27. C. F. Shih, Division of Engineering, Brown University Report No. MRL E-147, Providence, RI, June 1983.

28. R. D. Pendse and R. O. Ritchie, in Modeling Environmental Effects on Crack Growth Processes, R. H. Jones and W. W. Gerberich, eds., TMS-AIME, Warrendale, PA, 321-42, 1986.

29. J. R. Rice and D. M. Tracey, J. Mech. Phys. Solids, 17, 201-17, 1969.

30. J. R. Rice and M. A. Johnson, in Inelastic Behavior of Solids, M. F. Kanninen, W. G. Adler, A. R. Rosenfield, and R. I. Jaffee, eds., McGraw-Hill, New York, NY, 641-72, 1970.

31. R. M. McMeeking, J. Mech. Phys. Solids, 25, 357-81, 1977.

32. S. Lee, L. Majno and R. J. Asaro, Metall. Trans. A, 16A, 1633-48, 1985.

33. A. Needleman and V. Tvergaard, J. Mech. Phys. Solids, 32, 461, 1984.

34. N. Ohno and J. W. Hutchinson, J. Mech. Phys. Solids, 32, 63-85, 1984.

35. V. Tvergaard, Int. J. Fracture, 17, 389-407, 1981.

36. H. Yamamoto, Int. J. Fracture, 14, 347-65, 1978.

37. M. Sage, J. Pan and A. Needleman, Int. J. Fracture, 19, 163-82, 1982.

38. R. O. Ritchie and J. F. Knott, Acta Met., 21, 639-48, 1973.

39. R. O. Ritchie, Int. Met. Rev., 20, 205-30, 1979.

40. S. Surash and R. O. Ritchie, in Fatigue Crack Growth Threshold Concepts, D. L. Davidson and S. Suresh, eds., TMS-AIME, Warrendale PA, 227-61, 1984.

41. R. O. Ritchie, S. Suresh and P. K. Liaw, in Ultrasonic Fatigue, J. M. Wells, O. Buck, L. D. Roth, and J. K. Tien, eds., TMS-AIME, Warrendale, PA, 443-60, 1982.

42. S. Suresh, Metall. Trans. A, 14A, 2375-85, 1983.

43. D. L. Davidson, Fat. Eng. Mat. Struct., 3, 229-36, 1981.

44. K. A. Esaklul, A. G. Wright and W. W. Gerberich, Scripta Met., 17, 1073-78, 1983.

45. B. Budiansky, J. W. Hutchinson and J. C. Lambropoulos, Int. J. Solids Structures, 19, 337-55, 1983.

46. A. G. Evans, Z. B. Ahmad, D. G. Gilbert and P. W. R. Beaumont, Acta. Metall., 34, 79-87, 1986.

47. R. M. McMeeking and A. G. Evans, J. Amer. Cer. Soc., 65, 242-6, 1982.

48. D. B. Marshall, A. G. Evans and M. Drory, in Fracture Mechanics of Ceramics, R. C. Bradt, A. G. Evans, D. P. H. Hasselman, and F. F. Lange, eds., Plenum, New York, 289-307, 1983.

49. D. R. Clarke, J. Amer. Cer. Soc., 67, C-15-6, 1984.

50. J. W. Bristow, Br. J. Appl. Phys., 11, 81-5, 1960.

51. Anon, ASTM Standard ANSI/ASTM E112-80, Annual Book of ASTM Standards, Part 11, American Society for Testing and Materials, Philadelphia, PA, 186-220, 1980.

52. J. H. Richardson, Optical Microscopy for the Material Sciences, Marcel Dekker, Inc., New York, 603, 1971.

3.7. APPENDIX I

Crack Tip Shielding due to a Crack Tip Zone of Microvoids

The extent of extrinsic toughening from the in situ formation of microvoids in a zone surrounding the crack may be approximated by application of models developed for microcrack toughening in brittle materials (9). In the present analysis, only an initial indication of the shielding will be attempted; a more rigorous application of zone shielding models using J-integral techniques appropriate to ductile materials (45,46) is beyond the scope of the present study.

Calculations are based on the original model of Evans and co-workers (47,48) for toughening derived from a dilatant phase transformation in a zone surrounding a crack. The model is modified to account for the effect of void formation on reducing the bulk modulus, B, in the process zone (49), and assumes uniform void size and distribution.[4]

---

[4]For damage from hydrogen attack, the small effect of the methane gas pressure within the voids, which will tend to offset this reduction in bulk modulus, have been ignored.

A schematic illustration of a crack surrounded by a constrained dilatant zone is shown in Figure 3.A1. The resulting stress associated with the formation of voids, in a zone constrained by a rigid surrounding matrix, is given by (49):

$$P = \varepsilon B_{eff} \quad , \tag{3.A1}$$

where ε is the total unconstrained dilational strain of the voids, and B_{eff} is the effective bulk modulus of the process zone after void formation, which may be approximated in terms of the bulk modulus B of the surrounding matrix and the volume fraction Vf of microvoids, by (50):

$$B_{eff} = B\left[1 - \frac{16(1 - \upsilon^2)Vf}{9(1 - 2\upsilon)}\right] \tag{3.A2}$$

It follows from the analytical development of (47-49) that the maximum shielding obtained from a fully developed process zone is:

$$K_s = 0.22\ \varepsilon\ B_{eff}\sqrt{W} \qquad (3.A3)$$

where W is the zone height.

The applied stress intensity, K_{app}, associated with the remote loading, therefore, differs from the near tip stress intensity, K_{tip}, actually experienced at the crack tip, by the extent of shielding given by K_s, ie.:

$$K_{app} = K_{tip} + K_s \quad . \qquad (3.A4)$$

For a distribution of voids similar to those obtained in A533B (LE and NE conditions), assuming that $\varepsilon = Vf$, and equating the process zone height to the plastic zone size ($r_y \approx 1/2\pi\ (K_{IC}/\sigma_o)^2$, where K_{IC} is the critical stress intensity factor of the process zone), the resulting shielding stress intensities, K_s, are estimated in Table AI. It can be seen that the magnitude of shielding from a zone of microvoids surrounding the crack, i.e., from in situ damage, can be very significant for large microvoid volume fractions, even in materials of relatively high intrinsic toughness. Such shielding would not be expected in the present study on prior damage, as the

Table AI. Estimated Extrinsic Zone Shielding, K_s, for In Situ Void Formation in A533B

Condition	K_{IC} ($MPa\sqrt{m}$)	Vf	r_y (mm)	B_{eff}/B	K_s ($MPa\sqrt{m}$)
LE (L-T)	138	0.001	7.6	0.995	6
(S-T)	58	0.001	1.3	0.995	3
NE (L-T)	57	0.021	2.7	0.901	68
(S-T)	30	0.021	0.7	0.901	35

microvoids are uniformly dispersed on grain boundaries throughout the sample. Moreover, the shielding may be offset by a reduction of the intrinsic toughness of the material. This degradation may be

particularly severe with increasing void volume fractions in ductile materials, as is apparent in the present study for $Vf \geq 0.001$.[5]

[5]This is in contrast to brittle materials, which display a linear decay in intrinsic toughness with increasing microcrack volume fraction (9).

3.8. APPENDIX II

Estimation of Grain Boundary Volume Fraction of Microvoids

The average grain boundary volume fraction of microvoids, Vf_{gb}, was estimated from the specific volume change, ΔV, determined from density measurements.[6] The steel investigated had a grain size of

[6]Small changes in volume associated with the gradual loss of martensitic character of the microstructure and changes in carbide morphology during exposure to hydrogen have been ignored.

$\sim$ 30 μm and average intercept count, N_L, of 38 per mm (51). The grain boundary surface area per unit volume, S_V, may be related to N_L by the expression (52):

$$S_V \approx 2N_L \tag{3.A5}$$

where S_V has units of mm^2/mm^3. Thus, for the present study, S_V = 75 mm^2/mm^3. A uniform grain boundary distribution of spherical voids was assumed with a mean spacing of ℓ. If the width of the boundary is taken to be the mean void spacing then:

$$Vf_{gb} \approx \frac{\Delta V}{S_V \cdot \ell} \tag{3.A6}$$

where the values of V and ℓ are given in Table IV.

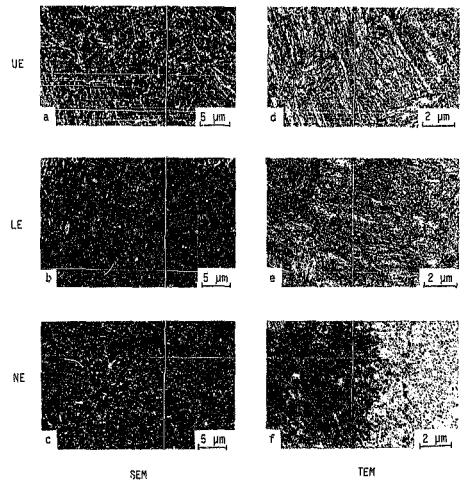


Figure 3.1 Microstructure of A533B steel in the unexposed (UE) and hydrogen pre-exposed (LE and NE) conditions. Micrographs on the left are from SEM of polished surfaces (etched in 2% nital); on the right from TEM of thin foils.

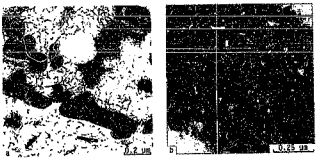


Figure 3.2 Typical carbide morphologies in the unexposed A533B steel showing the coarse interlath and grain boundary Fe-rich M_3C and fine needle-shaped intralath (Mo rich + Fe) M_2C carbides. (TEM carbon extraction replica.)

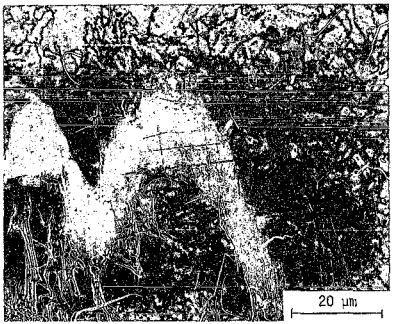


Figure 3.3 Optical micrograph showing incipient fissure formation from microvoid clusters in the NE condition.

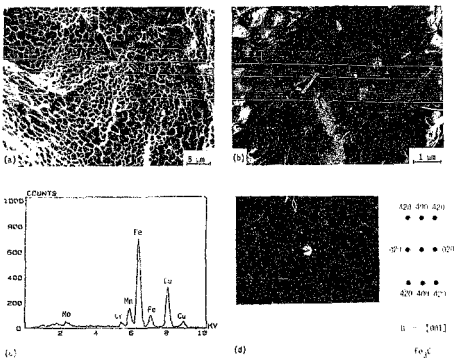


Figure 3.4 Severely cavitated intergranular fracture surface from fracture toughness test on A533B following NE. (a) SEM micrograph, (b) TEM of fracture surface extraction replica, and identification of particles using EDS and SAD in (c) and (d), respectively.

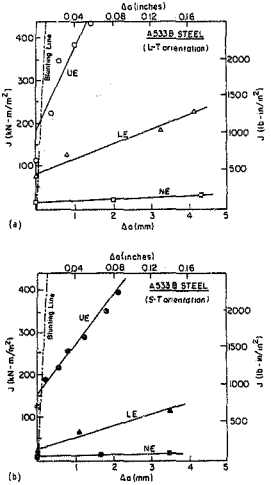


Figure 3.5 $J_R(\Delta a)$ resistance curves for the undamaged (UE) and grain boundary voided (LE and NE) conditions in A533B steel tested in the (a) L-T and (b) S-T orientations. Tests on C(T) specimens are used to determine the crack initiation fracture toughness, K_{Ic} and J_{Ic}, and the tearing modulus, T_R.

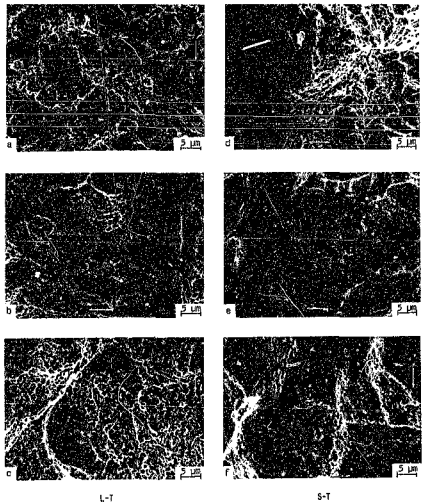


Figure 3.6 SEM fractographs of broken C(T) specimens in the unexposed UE and hydrogen exposed LE and NE conditions. Note the increasing incidence of methane bubble formation on grain boundaries with increasing hydrogen exposure. Arrows indicate general direction of crack growth.

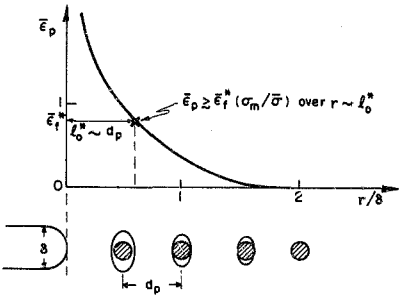


Figure 3.7 Schematic illustration of the stress-modified critical strain model for ductile fracture by microvoid coalescence.

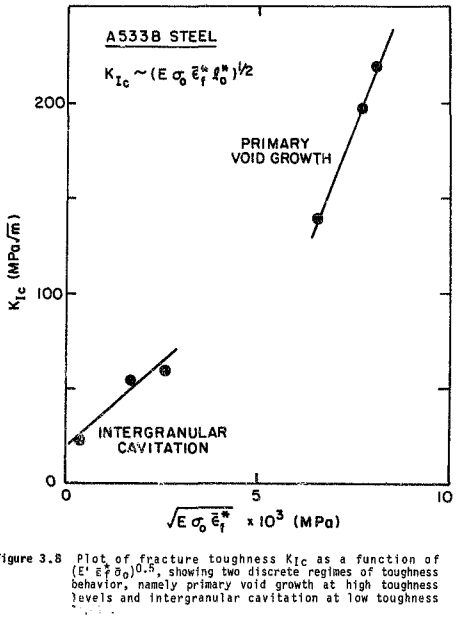


Figure 3.8 Plot of fracture toughness K_{Ic} as a function of $(E'\,\bar{\epsilon}_f^{*}\,\bar{\sigma}_0)^{0.5}$, showing two discrete regimes of toughness behavior, namely primary void growth at high toughness levels and intergranular cavitation at low toughness

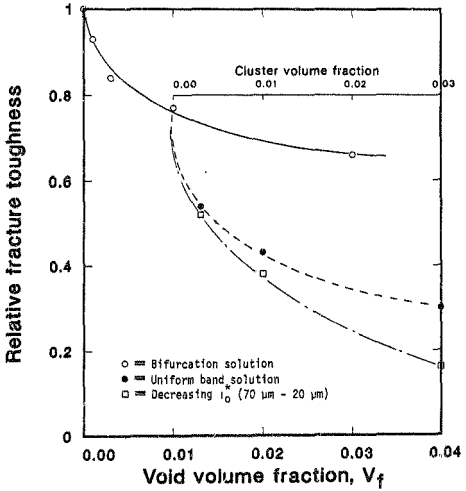


Figure 3.9 Predicted trends of the relative intrinsic toughness of an elastic-plastic solid with increasing background void volume fraction, Vf (solid line), microvoid cluster volume fraction above the background Vf of 0.01 (upper broken line), and the additional effect of decreasing the characteristic distance l_0^* (lower broken line).

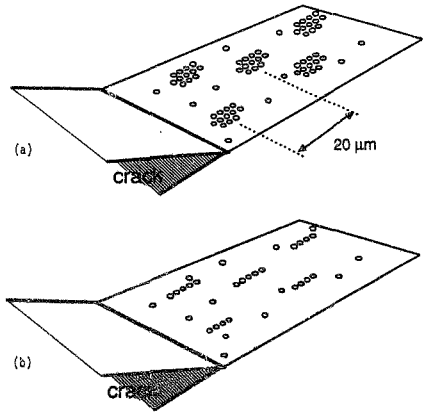


Figure 3.10 Extent of void clusters intersected by the crack plane in the (a) S-T, and (b) L-T orientations.

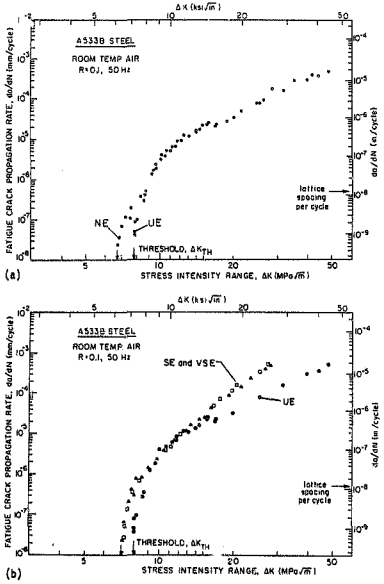


Figure 3.11 Fatigue crack propagation (da/dN) behavior as a function of the nominal stress intensity range (ΔK) in A533B steel at R = 0.1. Both (a) mild degrees (NE) and (b) severe degrees (SE and VSE) of pre-existing grain boundary microvoid formation have only a small influence on crack propagation rates, compared to behavior in the undamaged (UE) condition (after ref. 10).

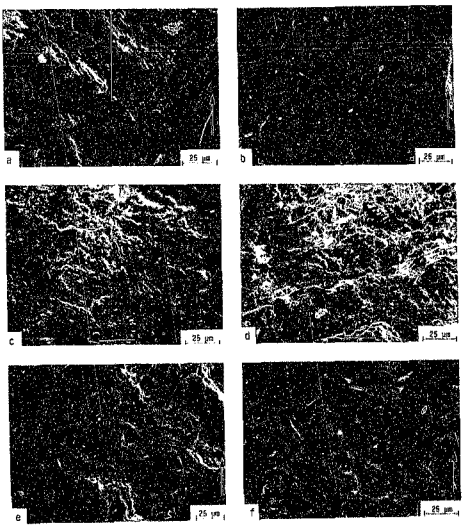


Figure 3.12 Scanning electron micrographs of fatigue fracture surfaces at near-threshold and higher growth rates in A533B steel, for varying degrees of grain boundary microvoid damage, showing UE structure at (a) ΔK = 8 MPa$\sqrt{m}$ and (b) ΔK = 30 MPa$\sqrt{m}$; NE structure at (c) ΔK = 7 MPa$\sqrt{m}$ and (d) ΔK = 29 MPa$\sqrt{m}$; and SE structure at (e) ΔK = 7 MPa$\sqrt{m}$ and (f) ΔK = 26 MPa$\sqrt{m}$. Arrows indicate general direction of crack growth.

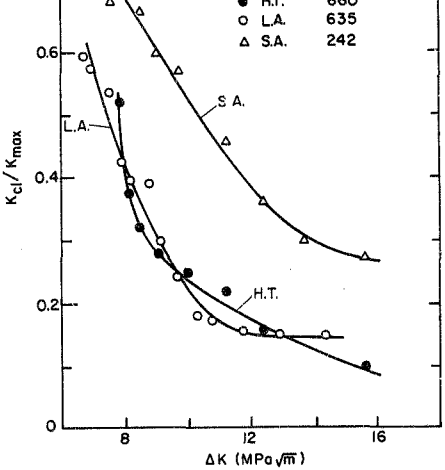


Figure 3.13 Experimentally measured variation of fatigue crack closure in A533B steel, for varying degrees of grain boundary microvoid damage, showing ratio of closure to maximum stress intensity, K_{cl}/K_{max}, as a function of K_I for undamaged (UE) and voided (NE and SE) microstructures. Note how increasing degrees of microvoid formation results in increased crack tip shielding through closure.

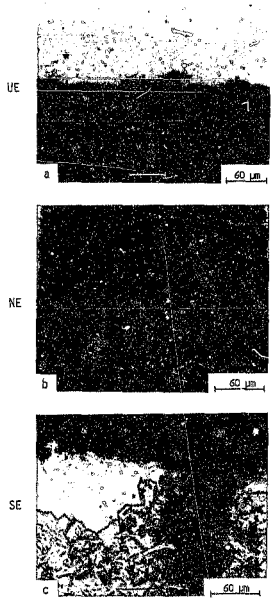


Figure 3.14 Near-threshold crack path morphologies, obtained in A533B steel from nickel-plated fracture surfaces, showing linear crack paths in (a) undamaged (UE) and (b) voided (NE) microstructures, and highly tortuous crack path in (c) extensively voided (SE) microstructure. Arrows indicate general direction of crack advance.

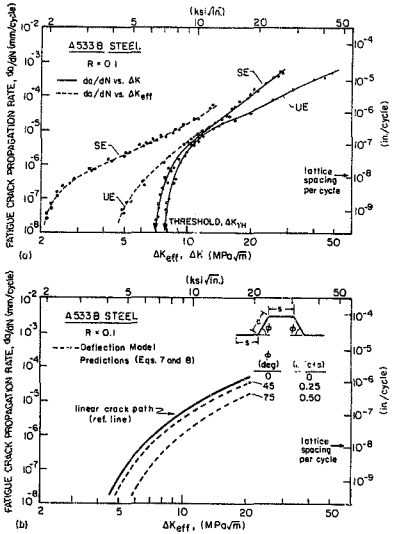


Figure 3.15 Respective roles of crack closure and crack deflection in influencing fatigue crack propagation in undamaged (UE) and extensively voided (SE) A533B steel, showing (a) experimental da/dN versus nominal ΔK data (from Figure 3.11) corrected for closure for da/dN versus ΔK_{eff} data, using experimental K_{cl} measurements; and (b) predictions of the effect of crack deflection using two-dimensional linear elastic deflection model (Eqns. 3.7 and 3.8) for φ = 45 to 75 deg with c/(c + s) = 0.25 to 0.5.

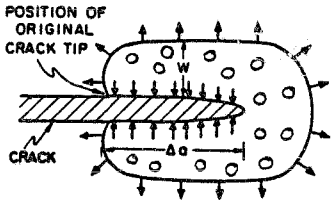


Figure 3.A1 Schematic illustration of a crack surrounded by a constrained dilatant zone: tractions give rise to an internal pressure resulting from the dilatant strain of void formation.

CHAPTER 4: FATIGUE CRACK PROPAGATION IN TRANSFORMATION-TOUGHENED ZIRCONIA CERAMIC

ABSTRACT

Fatigue crack propagation under tension-tension loading is observed in a transformation-toughened partially-stabilized zirconia (PSZ) ceramic containing 9 mol% MgO. Such subcritical crack growth behavior is demonstrated to be cyclically induced, based on a comparison with behavior under sustained loading (at the maximum load in the fatigue cycle) and at varying cyclic frequencies. Crack extension rates, which are measured as a function of the cyclic stress intensity range ΔK over the range 10^{-10} tc 10^{-6} m/cycle, are found to be load ratio dependent and to show evidence of fatigue crack closure, similar to behavior in metals. Cyclic crack growth rates are observed at ΔK levels as low as 3 MPa$\sqrt{m}$, and are considerably faster in moist environments. Moreover, transient accelerations and decelerations in growth rates were observed following low-high and high-low block overloads. Compared to environmentally-assisted, sub-critical crack growth in PSZ under sustained-load conditions, cyclic crack velocities were up to 8 orders of magnitude faster and showed a 40% lower threshold.

4.1. INTRODUCTION

It has long been the general perception that ceramics do not suffer significant degradation by fatigue (1-3). Accordingly, other mechanisms of subcritical crack growth, primarily involving environmentally-assisted cracking processes under monotonic loading, have received far more attention (4-7). Of late, however, there has been increasing interest in possible mechanisms of cyclic crack propagation as viable modes of subcritical crack extension in brittle materials (7-11), although unequivocal demonstrations of fatigue effects are not common (1).

The refuted existence of true cyclic crack propagation effects in conventional monolithic ceramics has been based primarily on the very limited crack tip plasticity apparent in these materials (1). However, where other mechanisms of local inelastic deformation prevail, or where unloading induces additional fracture phenomena, the notion of fatigue in ceramics clearly becomes more acceptable. For tension-tension and tension-compression loading, several such mechanisms have been suggested, including the deformation and lateral cracking of crack surface asperities on unloading (1), tensile opening from the wedging action of asperities (1) or

corrosion/reaction products (12) between the crack walls, friction induced heating at the crack tip (8), and environmentally-assisted cracking processes (8,12). In addition, fatigue cracking has recently been reported in polycrystalline alumina ceramics under far-field cyclic compression loading (11).

In ceramics toughened by crack tip shielding mechanisms, employing, for example, dilatant zones around the crack arising from in situ phase transformation or microcracking phenomena (13,14), the resulting nonlinear stress-strain response suggests the strong possibility of fatigue effects. Although evidence for such behavior in "shielded" ceramics has been observed in bend bars subjected to applied cyclic compressive loading (15), there is little information on corresponding cyclic crack growth under more conventional tension-tension loading.

It is the prime objective of this study to demonstrate that such cyclic crack growth can occur in transformation-toughened ceramics under tension-tension loading, and furthermore that such behavior occurs at stress intensities below, and at crack velocities far above, that commonly reported (5-7) for subcritical crack advance induced by environmental mechanisms.

4.2. EXPERIMENTAL PROCEDURE

Precipitated partially-stabilized zirconia (PSZ), containing 9 mol% MgO, was selected for the present study as it has been extensively characterized with respect to its transformation toughening behavior (13,16-18). Approximately 6% by volume of this material undergoes a stress-induced martensitic transformation, although up to 40% can transform in the high stress fields near a crack tip (18). The microstructure consists of cubic ZrO_2 grains, 50 μm in diameter, containing lens-shaped tetragonal precipitates of maximum dimension 300 nm (17).

Uniaxial tensile properties indicate a tensile strength of 400 MPa and a Young's modulus of 208 GPa. The material displays marked resistance curve toughness behavior, characteristic of significant crack tip shielding. An initiation fracture toughness of approximately 3.9 $MPa\sqrt{m}$ (for an initial crack length of approximately one grain diameter) was apparent with a maximum achievable fracture toughness K_c of up to 18 $MPa\sqrt{m}$. Using suitable "aging" heat treatments, a low toughness condition (K_c of ~5.5 $MPa\sqrt{m}$) and a mid-toughened condition (K_c of ~11.5 $MPa\sqrt{m}$) were also assessed. Extensive microstructural and mechanical property evaluation on this material have been described elsewhere (13,16-18).

Fatigue crack propagation studies were conducted on long (> 3 mm) through-thickness cracks in 3 mm thick compact C(T) specimens, tested in controlled room air (22°C, 45% relative humidity) using

high resolution automated electro-servo-hydraulic testing machines. Initiation of a pre-crack was facilitated by a wedge shaped starter notch. The cyclic frequency, ν, of the applied stress intensity range ($\Delta K = K_{max} - K_{min}$, where K_{max} and K_{min} are the maximum and minimum stress intensities in the fatigue cycle) was varied between 1 and 50 Hz (sine wave) and the load ratio ($R = K_{min}/K_{max}$) between 0.10 and 0.46. Crack growth rates over the range 10^{-10} and 10^{-6} m/cycle were determined under both manual and computer-controlled K-decreasing and K-increasing conditions (normalized K-gradient set at 0.08 mm^{-1} (19)). Crack lengths were continuously monitored, with a resolution typically better than 2 μm, by employing an electrical resistance technique (20) on thin (0.05 to 6 μm thick) NiCr metal foils, which were either bonded or evaporated onto the specimen surface. Simultaneous measurement of the extent of fatigue crack closure (21,22) was achieved using strain gauges mounted on the back surface of the C(T) samples. Using this technique (23), the stress intensity at closure, K_{cl}, defined at first contact of the fracture surfaces on unloading, is determined from the load corresponding to the first deviation from linearity of the elastic compliance curve. A schematic illustration of these techniques is shown in Figure 4.1. Fatigue data are presented in the form of both crack growth rate per cycle, da/dN, and crack velocity (with respect to time), $da/dt = \nu(da/dN)$, as a function of either the applied maximum stress intensity, K_{max}, or the cyclic stress intensity range, ΔK.

Environmental tests were conducted in dry nitrogen gas (inert environment) and distilled water (corrosive environment) by sealing the test piece in an airtight environmental chamber. Gas purity and the environmental temperature were preserved using an appropriate purification and temperature control system. The effect of the crack wake was assessed by growing a crack in the mid-toughened material under constant ΔK conditions. A load ratio of $R = 0.1$ was employed and the loads were continuously adjusted using computer control to maintain the required constant $\Delta K = 5.48$ MPa$\sqrt{m}$. Subsequently, a high-low and low-high block loading sequence was employed to determine transient variations in the crack growth rate.

In order to provide an indication of the maximum transformation toughening under monotonic loading, fracture toughness tests to determine $K_R(\Delta a)$ resistance curves were conducted on selected specimen subsequent to the fatigue test. K_R versus crack extenson Δa curves were computed using appropriate C(T) stress intensity calibrations and load versus crack length data recorded during the test. Tests were conducted in similar environmental conditions to those employed for the respective fatigue test.

Fracture surfaces were examined in the scanning electron microscope (SEM). Crack path profiles were studied using optical microscopy on appropriate polished surfaces perpendicular to the fracture surface.

4.3. RESULTS

Results illustrating rates of fatigue crack propagation da/dN in the low toughened PSZ are presented as a function of the applied stress intensity range ΔK in Figure 4.2. The majority of data pertains to a load ratio of 0.10 at a cyclic frequency of 50 Hz, although additional results, at load ratios of 0.15, 0.31 and 0.46 and frequencies of 1 and 10 Hz, are included for comparison. It is apparent that, over the wide range of growth rates studied, propagation rates are a power law function of the stress intensity range, exhibiting a growth law of the form $da/dN \propto \Delta K^m$, identical to that observed during fatigue in metals (24). However, whereas the exponent m in metals is typically of the order of 2 to 4 in this regime (24,25), growth rates in the ceramic are far more sensitive to ΔK, with m values approaching 24. In addition, a marked dependence on load ratio is also apparent. The actual crack growth equation at R = 0.10, determined from Figure 4.2 using regression analysis, is given in units of m/cycle and $MPa\sqrt{m}$ by:

$$da/dN = 6.31 \times 10^{-22} (\Delta K)^{24} \quad . \qquad (4.1)$$

The closure level corresponding to the R = 0.10 data is plotted as the ratio K_{cl}/K_{max} in Figure 4.3 as a function of the applied ΔK range.

Optical micrographs of the fatigue crack path in Figure 4.4(a,b) show significant crack deflection and evidence of crack bridging just behind the crack tip. SEM examination of the corresponding crack surfaces revealed a transgranular fracture morphology, nominally similar to that obtained under monotonic loading conditions (Figure 4.4(c,d)). Although striations have been reported for a glass ceramic during cyclic contact loading (26) and are commonly seen during the fatigue of metals (27), no evidence was found in the present study of striations or crack arrest markings in PSZ.

Whereas the data in Figure 4.2 apparently show a clear fatigue effect, in view of past skepticism over fatigue in ceramics, it is necessary to demonstrate unequivocally that the crack growth observed is cyclically induced, and that other subcritical cracking mechanisms are not responsible. To this end, three separate sets of experiments were conducted (Figure 4.5), as described below.

4.3.1. (i) Sustained Load Behavior

To show that the observed crack growth was not merely a result of sustained load cracking at maximum load, crack extension was monitored with a) the stress intensity

cyclically varied between K_{max} and K_{min}, and b) the stress intensity held constant at the same value of K_{max}. This procedure was periodically repeated during the entire range of growth rates; a typical result is shown in Figure 4.5(a). It is apparent that, whereas crack extension proceeds readily under cyclic loading conditions (region a), upon removal of the cyclic component by holding at the same K_{max} (region b), no crack growth was detectable.

(ii) Influence of Cyclic Frequency

The frequency dependence of rate of crack advance was examined, at a constant ΔK of 3.5 MPa$\sqrt{m}$, for cyclic frequencies of 1, 10 and 50 Hz (Figure 4.5(b)). For the range of frequencies tested, crack growth rates per cycle, da/dN, were effectively constant and frequency-independent, whereas crack velocities with respect to time, da/dt, increased linearly. This behavior is again similar to fatigue crack propagation in metallic alloys where environmental effects have been inhibited.

(iii) Influence of Stress Intensity Range

Rates of fatigue crack propagation in metals are generally more dependent on the range of stress intensity, rather than the mean or maximum levels (24). To examine this effect in the ceramic, tests were performed at a constant K_{max} (equal to 4.2 MPa$\sqrt{m}$) with increasing K_{min}. Results, in the form of crack velocity, da/dt, as a function of ΔK or the ratio K_{min}/K_{max} shown in Figure 4.5(c), clearly indicate a marked effect of decreasing crack velocities with decreasing stress intensity range at constant K_{max}.

4.3.2. Environmental Contribution to Crack Growth

The fatigue crack propagation behavior of the low toughened PSZ indicating the influence of an inert (dry nitrogen) and corrosive (distilled water) environment at a frequency of 50 Hz and load ratio R = 0.10 is presented in Figure 4.6. Results of the crack growth behavior in air are included for comparison. It is apparent from the data that growth rates are increased, and threshold ΔK_{TH} values decreased, in the moist environments compared to the inert environment. This behavior may be attributed to an environmentally-assisted slow crack growth contribution which acts to decrease the intrinsic resistance of the crack tip material to crack advance and hence accelerates growth rates. This degradation of the intrinsic toughness does not appear to be offset by increased extrinsic shielding from mechanisms such as oxide-induced crack closure or crack deflection which typically occurs in many metallic alloys when exposed to environmental degradation processes.

The effect of environment on the maximum extent of transformation toughening achieved was assessed under monotonic loading by determining the R-curve subsequent to each fatigue test. The resulting $K_R(\Delta a)$ curves showing similar maximum toughness values observed in the dry nitrogen, air and water environments are presented in Figure 4.7. Note that the full R-curve is not observed but begins at the final K_{max} of the ΔK range employed in the prior fatigue cycling. The abrupt decrease in the measured toughness apparent in the R-curves determined in the air and water environment (Figure 4.7) has only recently been observed for the present PSZ ceramic (28). Albeit beyond the scope of the present study, the effect is most likely associated with transitions from plane stress to plane strain dominated crack extension. In addition, despite the strong athermal component of the phase transformation experienced at the crack tip, previous zone size studies seem to indicate that thermal activation still plays a minor role (29). This effect may become noticeable as a decrease in zone size and concomitant decrease in toughness with increasing loading and crack propagation rates. Although of potential importance, particularly for components where design is based on maximum toughness considerations, a more indepth analysis awaits further detailed experimental data.

4.3.3. Influence of Fracture Toughness

The influence of fracture toughness on fatigue behavior is indicated in Figure 4.8 which shows the fatigue crack propagation rate of the peak-toughened material (K_c = 18 MPa$\sqrt{m}$) compared to that of the low-toughness condition (K_c = 5.5 MPa$\sqrt{m}$). The entire growth rate curve has been shifted to higher ΔK ranges suggesting that fatigue crack propagation might scale with the fracture toughness determined under monotonic loading conditions. This is in contrast to the power-law Paris regime (linear section of crack growth rate log(da/dN) vs. log(ΔK) plot) in metallic alloys which in general is not sensitive to the fracture toughness. It is, however, similar to the high growth rate region of fatigue crack propagation in metallic alloys, where K_{max} in the fatigue loading cycle approaches the fracture toughness K_{Ic} of the material and hence an obvious scaling with K_{Ic} occurs. In this region there is typically a crack growth mechanism transition to static fracture modes, such as cleavage fracture, which more closely approximates the brittle fracture modes in ceramic materials.

4.3.4. Constant ΔK and Block Loading Sequences

The extrinsic shielding associated with transformation toughening derives principally from material in the wake of the advancing crack tip. A characteristic of such shielding is

crack-size dependent behavior typically manifest by R-curve behavior under monotonic loading, and "anomalous" small crack growth rate effects in fatigue. Crack wake effects are therefore expected to exert a significant influence on the crack propagation rates during fatigue crack growth in PSZ. Such effects will, in addition, result in a sensitivity of measured fatigue crack growth rates to variation of the stress intensity range with crack length ($d\Delta K/da$) employed during threshold fatigue tests.

In order to provide some indication of these crack wake effects, crack propagation rates were measured under constant ΔK = 5.48 MPa$\sqrt{m}$ conditions in the mid-toughened (K_c = 11.5 MPa$\sqrt{m}$) material. Data indicating transient responses subsequent to high-low (from ΔK = 5.48 to 5.30 MPa$\sqrt{m}$) and low-high (from ΔK = 5.30 to 5.60 MPa$\sqrt{m}$) block loading sequences were also determined and results are presented in Figure 4.9. It is apparent from the data that the fatigue crack propagation rate remained approximately constant for a constant ΔK = 5.48 MPa$\sqrt{m}$ over a distance of ~2.5 mm. This distance was considered sufficiently long to demonstrate that once steady state toughening is achieved, no further increases in transformation toughening with crack extension occurs. Consequently, during fatigue crack propagation, growth rates remain uniform under constant ΔK loading conditions.

The results of the high-low block loading indicate a marked retardation in growth rates immediately after the load change, followed by an increasing growth rate until steady-state velocity is achieved (Figure 4.9). The crack length increment over which transient retarded growth rate behavior occurred was approximately 1.2 mm. Mirror image results were observed following the low-high block loading sequence in which transient accelerated crack growth rate behavior over a distance of approximately 1.0 mm was apparent. The crack length increments over which transient crack growth rate behavior was observed are slightly larger than 5H, where H is the transformation zone width. A transformation zone size of approximately 150 μm was observed in the mid-toughened PSZ using Namarski interference and Raman spectroscopy techniques [29,30). The maximum enhancement in transformation toughening is predicted to occur after a crack extension increment of 5H under monotonic loading (13).

4.4. DISCUSSION

The above results provide persuasive evidence of true cyclic crack growth in PSZ. Crack growth rates display a similar dependency to metals on mechanical factors such as frequency, load ratio, and ΔK, although the sensitivity to the latter two factors is clearly far greater in the ceramic. Increased crack growth rates were apparent in moist environments and have been attributed to an environmentally-assisted contribution to crack growth. Moreover, crack advance is

associated with several mechanisms of crack tip shielding, which act to reduce the local "crack driving force". In addition to transformation toughening in PSZ, the fatigue cracks show evidence of crack deflection and crack bridging (Figure 4.4), and fatigue crack closure involving physical contact between mating crack surfaces (21,22). The variation in crack closure, as shown by the back-face strain measurements of K_{cl} in Figure 4.3, is similar to that seen in metals at low (near-threshold) stress intensities, where closure is developed primarily by corrosion debris or asperities which act as wedges inside the crack (22). In view of the deflected intergranular nature of cyclic crack paths in the ceramic (Figure 4.4), it would seen likely that the wedging by fracture surface asperities (roughness-induced closure) is the predominant closure mechanism in PSZ.

Results of fatigue crack propagation under constant ΔK conditions indicate uniform crack growth rates over distances of up to 2.5 mm. This is in contrast to the highly discontinuous growth rates and periodic crack arrest over the entire range of ΔK values tested that has subsequently been reported for a similar PSZ material (31). In this work, the crack arrest, observed after growth over distances of the order of tens of microns, is attributed to an increase in the transformation toughening component with crack extension. In addition, an attempt is made to relate crack arrest distances to 5H, where H is the transformation zone size. The characteristic crack extension distance 5H indicates the onset of steady state shielding predicted for transformation toughening under monotonic loading (13). Extensive experimental results of the present study are, however, at variance with the behavior reported in ref. 30, showing no indication of discontinuous growth. However, results of the block loading studies reported in the present investigation do seem to attach some significance to the characteristic distance 5H, over which steady-state growth rate behavior is re-established following load changes.

It is beyond the scope of the present study to elucidate the precise mechanisms of fatigue in transformation-toughened PSZ. Clearly detailed microstructural studies are required to assess the effect of cyclic loading on such factors as i) the nature of the inelastic deformation, ii) the extent of phase transformation, iii) any concomitant changes in the transformed zone shape which may modify the degree of shielding, and iv) the changes in the (intrinsic) toughness of material from cyclic damage accumulation mechanisms, such as microcrack formation at particle/matrix interfaces, ahead of the crack tip. A more detailed discussion of possible mechanisms of fatigue crack propagation in extrinsically toughened ceramic materials together with suggestions for future work are presented in Chapter 5.

It is apparent, however, that the cyclic crack growth rates at stress intensities far below, and at crack velocities substantially above, that required for environmentally-induced monotonic crack

advance in PSZ ceramics. Comparison with Becher's sustained-load cracking data on a similar 7.2 mol% MgO PSZ, tested in 55% relative humidity air and in distilled water (6,7), indicates fatigue crack growth at stress intensities as low as 3 MPa$\sqrt{m}$, and cyclic crack velocities to be some 8 orders of magnitude faster, at K_{max} = 5 MPa$\sqrt{m}$, than corresponding rates under monotonic loading (Figure 4.10). Based on these data, it would appear that non-conservative estimates of subcritical crack extension and serious overestimates of life may result if damage-tolerant predictions in PSZ ceramics are based solely on sustained-load cracking and toughness behavior.

4.5. CONCLUSIONS

Based on a study of subcritical crack growth under tension-tension fatigue loading in partially-stabilized zirconia (PSZ), containing 9 vol% MgO, the following conclusions can be made:

1. Fatigue crack propagation under tension-tension loading in transformation-toughened PSZ ceramic is unequivocally demonstrated, and is shown to be governed by a power law function of the applied stress intensity range, ΔK, with an exponent of 24.

2. Akin to behavior in metals, cyclic crack growth rates are found to show similar dependencies on cyclic frequency, load ratio and ΔK level, although the sensitivity to the latter two factors is far greater in the ceramic. Crack propagation rates were increased in moist environments.

3. Cyclic crack growth is predominantly transgranular, with evidence of crack tip shielding by crack deflection, crack bridging (close to the crack tip), and fatigue crack closure, presumably arising from crack surface asperity wedging. Akin to near-threshold fatigue behavior in metals, the effect of such closure diminishes with increasing ΔK.

4. Uniform crack propagation rates were observed under constant ΔK loading conditions for cracks grown distances of up to 2.5 mm. Transient accelerations and decelerations were apparent following low-high and high-low block loading sequences.

5. Cyclic crack growth is found to occur at stress intensities far below, and at crack velocities up to 8 orders of magnitude above, that reported for environmentally-assisted sustained-load crack growth rates. Such observations may have serious implications for damage-tolerant life predictions in transformation-toughened ceramics.

4.6. REFERENCES

1. A. G. Evans, Int. J. Fract., 16 (6), 485-98, 1980.
2. A. G. Evans and M. Linzer, ibid., 12 (2), 217-22, 1976.
3. A. G. Evans and E. R. Fuller, Metall. Trans., 5 (1), 27-33, 1974.
4. S. M. Wiederhorn, E. R. Fuller and R. Thomson, Met. Sci., 14 (4), 450-8, 1980.
5. Li-Sheng Li and R. F. Pabst, J. Mater. Sci., 16 (11), 2861-6, 1980.
6. P. F. Becher, J. Mat. Sci., 21 (1), 297-300, 1966.
7. P. F. Becher, J. Am. Ceram. Soc., 66 (7), 485-488, 1983.
8. D. A. Krohn and D. P. H. Hasselman, J. Am. Ceram. Soc., 55 (4), 208-11, 1972.
9. F. Guiu, J. Mater. Sci., 13 (6), 1357-61, 1978.
10. H. N. Ko, J. Mater. Sci. Lett., 5 (4), 464-6, 1986.
11. L. Ewart and S. Suresh, ibid., 5 (4), 774-8, 1986.
12. L. S. Williams, Chapter 18 in Mechanical Properties of Engineering Ceramics, Edited by W. W. Kriegel and H. Palmour III, Interscience Publishers, Inc., New York, 1961.
13. A. G. Evans and R. M. Cannon, Acta Met., 34 (5), 761-800, 1986.
14. A. G. Evans and K. T. Faber, J. Am. Ceram. Soc., 67 (4), 255-60, 1984.
15. S. Suresh, personal communication, Division of Engineering, Brown University, Providence, RI, 1987.
16. R. H. J. Hannink and M. V. Swain, J. Aust. Ceram. Soc., 18 (2), 53-62, 1982.
17. D. B. Marshall, J. Am. Ceram. Soc., 69 (3), 173-80, 1986.
18. D. B. Marshall and M. R. James, ibid., 69 (3), 215-7, 1986.
19. ASTM Standard E 647-86A, "Standard Test Method for Constant-Load-Amplitude Fatigue Crack Growth Rates"; in 1986 ASTM Annual Book of Standards, Vol. 3.01, American Society for Testing and Materials, Philadelphia, PA, 1986.

20. P. K. Liaw, H. R. Hartmann and W. A. Logsdon, J. Test. Eval., 11 (3), 202-7, 1983.

21. W. Elber, "The Significance of Crack Closure"; pp. 230-42 in Damage Tolerance in Aircraft Structures, ASTM STP 486, American Society for Testing and Materials, Philadelphia, PA, 1971.

22. S. Suresh and R. O. Ritchie, "Near-Threshold Fatigue Crack Propagation: A Perspective on the Role of Crack Closure"; pp. 227-61 in Fatigue Crack Growth Threshold Concepts, Edited by D. L. Davidson and S. Suresh, TMS-AIME, Warrendale, PA, 1984.

23. R. O. Ritchie and W. Yu, "Short Fatigue Cracks: A Consequence of Crack Tip Shielding"; pp. 167-89 in Small Fatigue Cracks, Edited by R. O. Ritchie and J. Lankford, TMS-AIME, Warrendale, PA, 1986.

24. P. C. Paris and F. Erdogan, J. Basic Eng., Trans. ASME, Ser. D, 85 (12), 528-34, 1963.

25. R. O. Ritchie, Int. Metals Rev., 20 (5-6), 205-30, 1979.

26. Mei-Chien Lu and A. E. Evans, J. Am. Ceram. Soc., 68 (9), 505-510, 1985.

27. R. M. N. Pelloux, ASM Trans., 62 (1), 281-5, 1969.

28. R. H. Dauskardt and D. B. Marshall, unpublished data, Lawrence Berkeley Laboratories, Berkeley, CA 94720, and Rockwell International Science Center, Thousand Oaks, CA 91360, 1987.

29. I-Wei Chen and P. E. Reyes-Morel, Mat. Res. Symp. Proc., eds. P. F. Becher, M. V. Swain and S. Somiya, Materials Research Society, 78, 75-88, 1987.

30. R. H. Dauskardt, R. O. Ritchie and D. K. Veirs, Application of Spatially Resolved Raman Spectroscopy in the Study of Transformed Zones in PSZ Ceramic, to be published in J. Am. Ceram. Soc., 1988.

31. L. A. Sylva and S. Suresh, Brown University Report No. NSF-ENG-8451092/2/87, 1987.

4.7. FIGURES

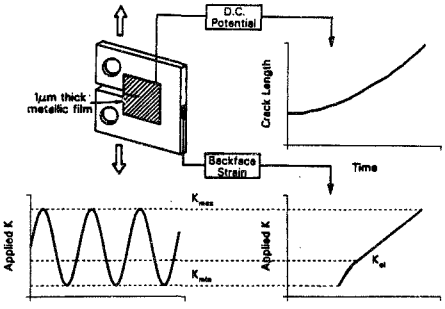


Figure 4.1 Schematic illustration of experimental techniques used to continuously monitor crack length and the stress intensity, K_{cl}, at fatigue crack closure.

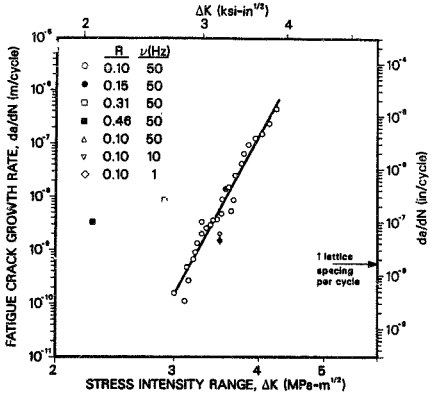


Figure 4.2 Variation of fatigue crack propagation rate, da/dN, with applied stress intensity intensity range, ΔK, for the low-toughened PSZ (MgO) ceramic, tested in room temperature air (45% relative humidity) at a load ratio R of 0.10 and a cyclic frequency of 50 Hz. Data for varying load ratio (0.10 - 0.46) and cyclic frequency (1 - 50 Hz) are included for comparison.

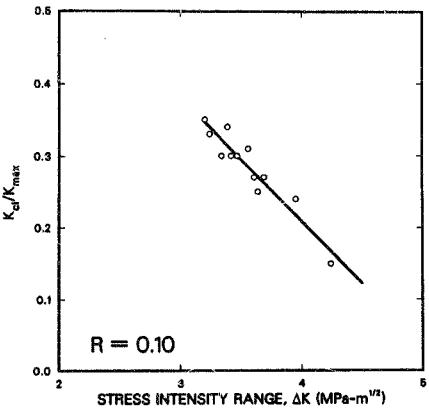


Figure 4.3 Experimentally measured variation of fatigue crack closure in PSZ (MgO), corresponding to cyclic crack growth rate data at R = 0.10 in Figure 4.2. Results, based on back-face strain compliance measurements, show the ratio of closure to maximum stress intensity, K_{cl}/K_{max}, as a function of the applied stress intensity range, ΔK.

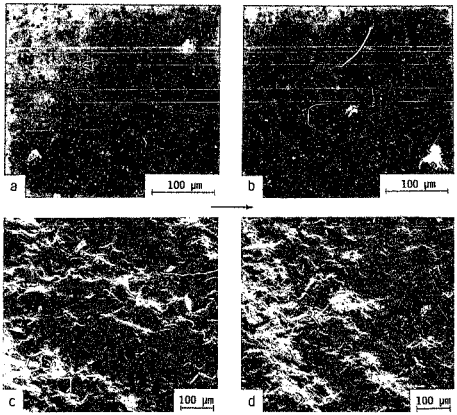


Figure 4.4 Fractography of crack growth in PSZ (MgO): optical micrographs of the fatigue crack path, showing (a) crack deflection and (b) crack bridging immediately behind the crack tip; scanning electron micrographs showing predominantly transgranular fracture surfaces associated with both (c) cyclically and (d) monotonically loaded cracks. Arrow indicates general direction of crack growth.

(a)

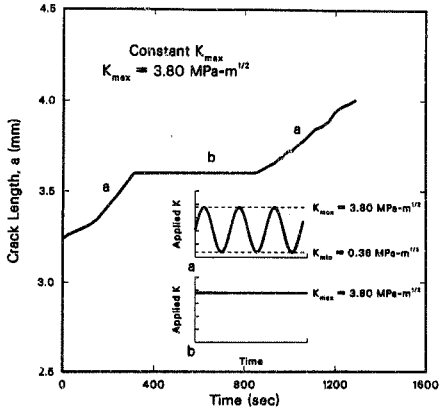
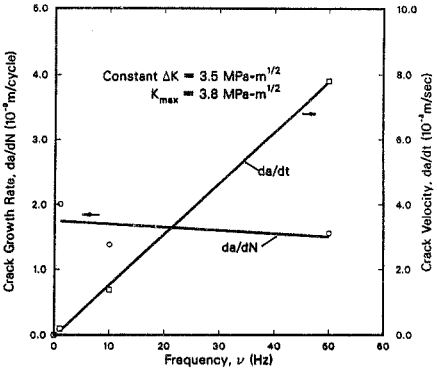
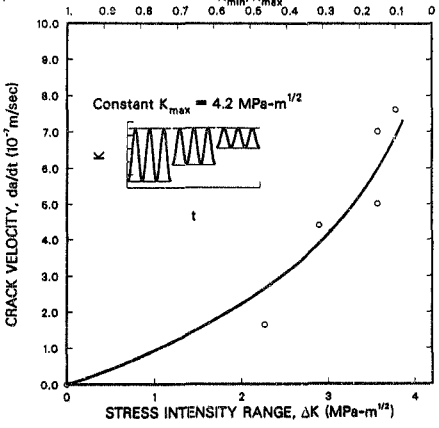


Figure 4.5 Effect in PSZ (MgO) of (a) sustained and cyclic loading conditions on crack growth rate, da/dN, at constant K_{max} (= 3.8 MPa$\sqrt{m}$), (b) varying cyclic frequency on crack growth rate, da/dN, and crack velocity, da/dt, at constant ΔK (= 3.5 MPa$\sqrt{m}$), and (c) varying applied stress intensity range, ΔK, on crack velocity, da/dt, at constant K_{max} (= 4.2 MPa$\sqrt{m}$).

(b)


Constant ΔK = 3.5 MPa-m^1/2
K_max = 3.8 MPa-m^1/2
da/dt
da/dN
Crack Growth Rate, da/dN (10^-3 m/cycle)
Crack Velocity, da/dt (10^-3 m/sec)
Frequency, ν (Hz)
0.0
1.0
2.0
3.0
4.0
5.0
6.0
8.0
10.0
0
10
20
30
40
50
60

(c)


K_{min}/K_{max}
1.
0.9
0.8
0.7
0.6
0.5
0.4
0.3
0.2
0.1
0
10.0
9.0
8.0
7.0
6.0
5.0
4.0
3.0
2.0
1.0
0.0
Constant K_{max} = 4.2 MPa-m$^{1/2}$
K
t
CRACK VELOCITY, da/dt (10^{-7} m/sec)
0
1
2
3
4
STRESS INTENSITY RANGE, ΔK (MPa-m$^{1/2}$)

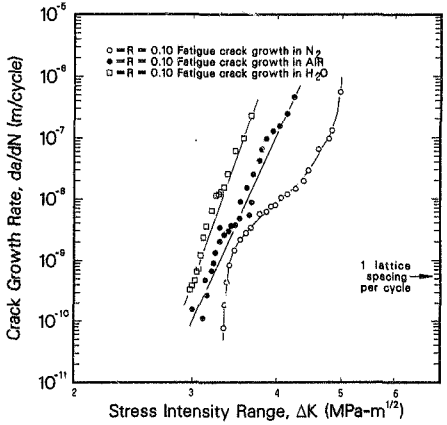


Figure 4.6 Fatigue crack propagation behavior of the low-toughened PSZ indicating the influence of an inert (dry nitrogen), (45% RH) air and corrosive (distilled water) environment at a frequence of 50 Hz and R = 0.10.

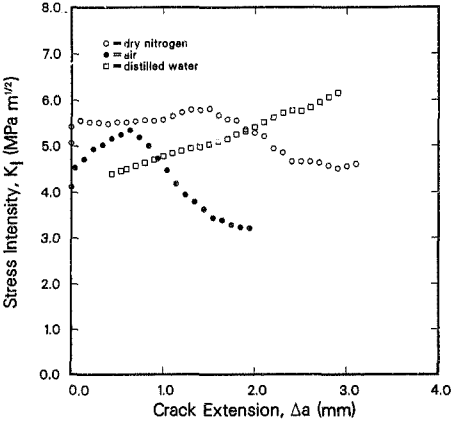


Figure 4.7 $K_R(\Delta a)$ resistance curves from fracture toughness tests indicating the effect of environment on the maximum toughness achieved.

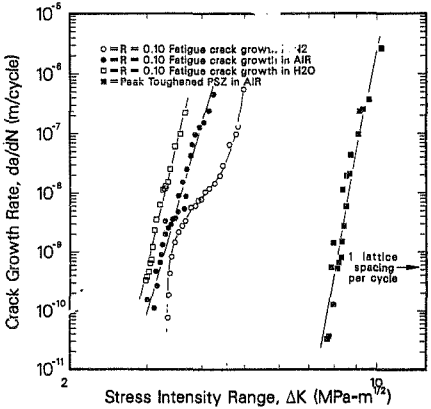


Figure 4.8 Variation of the fatigue crack propagation rate (da/dN) with applied stress intensity range ΔK for the peak-toughened PSZ material. Results for the low-toughened material are included for comparison.

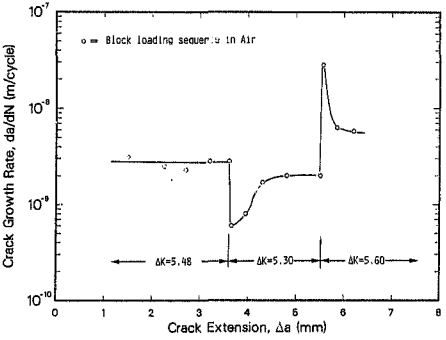


Figure 4.9 Variation of fatigue crack propagation rate (da/dN) showing the effect of constant ΔK = 5.48 MPa$\sqrt{m}$, and following block loading sequences. Note the transient retardation following the high-low sequence, and the transient acceleration following the low-high sequence.

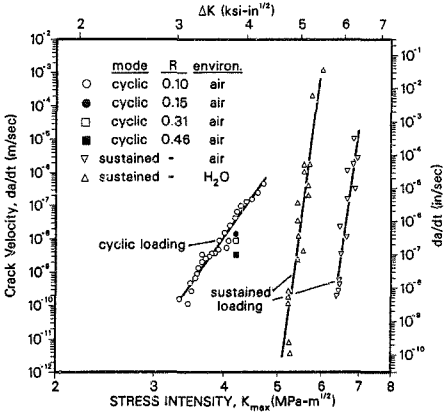


Figure 4.10 Subcritical crack growth behavior in PSZ (MgO) showing a comparison of cyclic crack velocities, da/dt, from the present study with sustained-load cracking data of Becher (6,7) for 55% relative humidity air and distilled water. *Note how fatigue-induced crack growth is much faster than* environmentally-assisted crack growth under monotonic loading conditions.

CHAPTER 5: IMPLICATIONS OF EXTRINSIC TOUGHENING AND PROPOSALS FOR FUTURE WORK

ABSTRACT

The utilization of crack tip shielding can be a potent means to enhance toughness and retard crack growth in a diverse range of materials. The implication of such extrinsic toughening, however, is crack-size dependent behavior and the breakdown of the concept of similitude. This important consequence is shown to result in resistance curve behavior, anomalous "small crack" effects, and contrasting microstructural factors controlling crack initiation and growth.

The future use of ceramics and ceramic composites for advanced structural applications represents an important precursor to potential major improvements in design performance for high temperature, corrosion and wear resistance. The limited use of such brittle materials to date has primarily been attributed to their inherently low toughness and lack of defect tolerance. Scientific research in the last decade, however, has resulted in major advances in the toughening of ceramics principally by extrinsic shielding mechanisms. Although an essential development to their structural use, work undertaken in the present study has shown that such toughened ceramics and composites, contrary to conventional wisdom, may become susceptible to cyclic fatigue. Possible mechanisms of such cyclic fatigue are identified and discussed with regard to four major classes of ceramic and ceramic-matrix composites. Suggestions for future work are presented.

5.1. INTRODUCTION

Processes of crack tip shielding have been shown to provide a potent means of extrinsic toughening during crack propagation in a diverse range of materials, environmental and loading conditions. The various mechanisms of crack tip shielding have been categorized into several distinct classes, namely, crack deflection and meandering, zone shielding, contact shielding, and combined zone and contact shielding. In general, such shielding may be seen to originate from processes which predominate in the wake of the crack tip. An important consequence of this characteristic of extrinsic toughening, however, is crack-size dependent behavior. This in turn leads directly to the breakdown of the concept of similitude and anomalous crack growth behavior. These significant implications of extrinsic toughening, including resistance-curve behavior, "small crack"

CHAPTER 5: IMPLICATIONS OF EXTRINSIC TOUGHENING AND PROPOSALS FOR FUTURE WORK

ABSTRACT

The utilization of crack tip shielding can be a potent means to enhance toughness and retard crack growth in a diverse range of materials. The implication of such extrinsic toughening, however, is crack-size dependent behavior and the breakdown of the concept of similitude. This important consequence is shown to result in resistance curve behavior, anomalous "small crack" effects, and contrasting microstructural factors controlling crack initiation and growth.

The future use of ceramics and ceramic composites for advanced structural applications represents an important precursor to potential major improvements in design performance for high temperature, corrosion and wear resistance. The limited use of such brittle materials to date has primarily been attributed to their inherently low toughness and lack of defect tolerance. Scientific research in the last decade, however, has resulted in major advances in the toughening of ceramics principally by extrinsic shielding mechanisms. Although an essential development to their structural use, work undertaken in the present study has shown that such toughened ceramics and composites, contrary to conventional wisdom, may become susceptible to cyclic fatigue. Possible mechanisms of such cyclic fatigue are identified and discussed with regard to four major classes of ceramic and ceramic-matrix composites. Suggestions for future work are presented.

5.1. INTRODUCTION

Processes of crack tip shielding have been shown to provide a potent means of extrinsic toughening during crack propagation in a diverse range of materials, environmental and loading conditions. The various mechanisms of crack tip shielding have been categorized into several distinct classes, namely, crack deflection and meandering, zone shielding, contact shielding, and combined zone and contact shielding. In general, such shielding may be seen to originate from processes which predominate in the wake of the crack tip. An important consequence of this characteristic of extrinsic toughening, however, is crack-size dependent behavior. This in turn leads directly to the breakdown of the concept of similitude and anomalous crack growth behavior. These significant implications of extrinsic toughening, including resistance-curve behavior, "small crack"

effects, and contrasting microstructural factors controlling crack initiation and growth, are discussed in the present chapter.

An additional implication, however, which has potentially major repercussions with regard to reliable design, regards processes of cyclic subcritical crack propagation in a recently developed range of advanced materials. These materials, which in particular includes ceramic and ceramic-matrix composites, rely almost entirely on extrinsic toughening mechanisms for acceptable toughness properties. Paradoxically, with this approach to toughening, results of the present investigation indicate that these materials can become prone to cyclic fatigue degradation. This form of degradation has in particular been associated with the non-linear behavior of material elements in the vicinity of the crack tip in transformation toughened ceramics. However, various additional forms of damage accumulation associated with other mechanisms of extrinsic toughening under cyclic loading conditions may also be identified as potential sources of fatigue. The concluding sections of the present work therefore focuses on these phenomena, speculates on possible mechanisms of such cyclic fatigue, and includes suggestions for future work.

5.2. GENERAL IMPLICATIONS OF EXTRINSIC TOUGHENING

Intrinsic toughening is essentially a property of the material/microstructure, and therefore can be expected to be active for a specific fracture mechanism independent of such factors as crack configuration, crack size, geometry, etc. Extrinsic mechanisms, however, demand the presence of a crack with sufficient wake for them to operate. **Thus, the direct implication of crack propagation dominated by shielding, aside from a reduced cracking rate from the lower local driving force, is crack-size dependent behavior.** A number of important scenarios follow:

First, the material will show resistance-curve fracture toughness behavior where the driving force to sustain cracking will increase with increasing crack length (until steady-state). Such R-curves are common in brittle materials which rely on process of zone shielding for extrinsic toughening. Marked R-curve toughness behavior evident in ceramics (1,2) is schematically illustrated in Figure 5.1. Here shielding can occur from transformation and microcrack toughening, or whisker reinforcement. Similar behavior has also been reported in rocks and concrete (3,4), where shallower curves are apparent due to microcracking phenomena. In addition, R-curve behavior has been identified in ductile metallic alloys, where zone shielding from prior plastic zones left in the wake of the crack induces a lower strain singularity ahead of the tip (c.f., the 1/r strain singularity for a fully plastic stationary crack with the ln(1/r) singularity for a non-stationary crack (5)).

Second, "small crack" effects are to be expected, since, at the same nominal driving force, the small crack may experience a higher local driving force, due to diminished shielding along its restricted wake, which causes it to propagate at a rate in excess of the long crack. Such accelerated growth of small cracks is now a well-known phenomenon in the fatigue of metallic alloys, as shown recently for example by the results on aluminum-lithium alloys (6), and has been demonstrated experimentally to be associated primarily with reduced shielding from crack closure (e.g. 6,7,8).

Third, microstructural factors known to be beneficial for resistance to crack initiation and the growth of small cracks may have a very different effect on the growth of long cracks (7). This follows because the role of extrinsic mechanisms becomes negligible where the crack wake is small or non-existent. There are numerous examples of this in the fatigue literature; for example in steels, increasing yield strength or decreasing grain size results in lower thresholds for (long) crack growth, yet higher thresholds for crack initiation, i.e., higher fatigue limits. In addition, in duplex or particle/precipitate-hardened materials, grain size, texture, slip character and precipitate/phase distribution appear to have a relatively minor influence on small crack growth, yet these factors have a significant influence on long crack growth rates primarily through their effect on crack closure and deflection (7). Similar effects have been reported in ceramics. In alumina for example, coarsening grain size (or even calcium embrittlement of the grain boundaries) can lead to degraded crack initiation toughness, yet once the crack has grown some distance, the resulting rougher fracture path induces significant crack bridging such that the coarser-grained (or embrittled) structures actually show superior crack growth toughness (9).

Finally, of particular interest in the present work, is the effect of fatigue loading conditions on the mechanisms of extrinsic toughening in ceramic and ceramic-matrix composite materials. As these materials, in general, rely primarily on such mechanisms for toughness, any degradation of the micromechanisms providing shielding may have significant implications for subsequent crack extension. In particular, in materials toughened by zone shielding mechanisms, for example, transformation or microcrack toughening, the effect of unloading may induce changes in the frontal process zone morphology due to the high stress fields generated ahead of the dilated zone itself. Although the extent of zone shielding scales with the process zone width, increases in the frontal zone size ahead of the crack tip are known to result in a reduced contribution to toughening. In fiber/whisker reinforced ceramic-matrix composites, cyclic loading may be expected to produce a progressive degradation in the fiber/whisker-matrix interfacial strength. Such decreases will reduce the shielding capacity of the bridging zone behind the crack tip, exposing the crack tip to an increased driving force. The synergistic effect of both a reduced extrinsic shielding component together with a degraded intrinsic toughness is therefore considered of particular

importance in understanding the fatigue behavior of ceramic materials.

Whereas certain of the intrinsic and extrinsic mechanisms described have been used to quantify the extent of toughening exhibited by various ceramic and ceramic-matrix composite microstructures under monotonic loading, to date there have been few systematic studies on subcritical crack extension behavior of these materials which specifically utilizes this dual approach under cyclic and sustained loading conditions. It is therefore considered appropriate to propose an investigation of a selected range of ceramic and reinforced ceramic-matrix composites, each exhibiting a distinct dominant toughening mechanism, which i) identifies the specific toughening mechanisms, in light of the characteristic microstructural features, ii) provides a detailed characterization of the fatigue crack propagation behavior in each material, particularly with regard to furnishing a basic understanding of the mechanisms of crack advance, iii) evaluates the relative dominance of the extrinsic versus intrinsic effects during fatigue crack growth, and specifies any unique implications to mechanical properties of this dominance, for example, the possible occurrence of small crack effects, iv) assesses the predominance of both mechanical and environmental variables controlling such subcritical crack extension, and hence, the potential of employing novel fatigue inhibition techniques to increase service life.

5.3. POSSIBLE MECHANISMS OF FATIGUE IN CERAMIC MATERIALS AND PROPOSALS FOR FUTURE WORK

5.3.1. Introdiction

The last decade has witnessed major improvements in the microstructural design and processing techniques of ceramics, which has provided a versatile class of materials offering exceptional properties in the areas of mechanical strength, extreme hardness and creep resistance. In combination with other properties such as dimensional stability, corrosion and wear resistance, and retention of strength with time at temperature, recent advances in the development of enhanced toughness has resulted in the potential of ceramics to perform functions structurally not possible with other more traditional engineering materials. As a result, ambitious predictions have been made for the application of ceramics in numerous engineering markets where their low density and unique set of properties may be exploited.

Of particular interest in the automotive, aerospace and defense industries are ceramic and reinforced ceramic-matrix composites for use in gas turbine and other advanced heat engine applications. Although the particular material property requirements for gas turbine and reciprocating engines differ, in both cases increased

operating temperatures and faster rotational speeds may provide impressive improvements in efficiency, power/weight ratios and fuel consumption. In gas turbine applications, blades, rotors, vanes, shrouds, combuster, combuster liners, and other parts are all candidates for ceramic materials. Here much effort has been directed towards the development of high performance ceramics and reinforced ceramic-matrix composites capable of operating at higher temperatures and higher operating stresses (10,11). While the high temperature properties have received most attention for heat-engine applications, these materials are also being developed for 'stationary' products such as heat exchangers, recuperators, tubes, exhaust systems and similar high-temperature operating equipment (12). Conversely, requirements for reciprocating heat engines stress the need for thermally insulating and wear and abrasion resistant materials (13,14). For example, in addition to hostile environmental conditions, the precombustion chamber in diesel engines must survive both mechanical and thermal stressing which is often cyclic in nature. Large temperature gradients are present and mechanical stresses may be exacerbated by thermal expansion mismatch between the chamber and cylinder-head materials (15). Advantages of ceramic components include improved combustion performance due to higher running temperatures, reduction of idle noise, and easier starting.

Life prediction is naturally crucial to permit the reliable design and use of ceramic materials. Accordingly, extensive research has been undertaken to improve the toughness of ceramics which ultimately translates into improved reliability. Advanced structural ceramics receiving the most attention in the past 15 years has been silicon nitrides, including sialons, silicon carbides, and transformation toughened zirconias (16). Silicon nitrides and carbides are believed to be capable of operating at temperatures up to 1650°C. Zirconia, in addition to being strong up to approximately 600°C, has the advantage of a lower thermal conductivity and a thermal expansivity matching that of many reciprocating engine (particularly diesel) materials. Extensive research is also being undertaken in the development of materials toughened by the addition of dispersed zirconia particles, whisker/fiber reinforced ceramic-matrix composites, microcrack toughening, and more recently the addition of ductile particle dispersions (17,18). A number of the more significant materials, together with their primary toughening mechanism and maximum toughness, are summarized in Table I.

Despite the impact of the potential widespread use of ceramics and ceramic-matrix composites, it is perhaps surprising that relatively few systematic studies of a fundamental nature have been performed to relate mechanistically, and ultimately model, the role of the composite microstructure in controlling **subcritical** crack growth resistance in these materials. This may be particularly important where crack propagation occurs under cyclic loading conditions. As most of the more significant applications of ceramics, particularly for components in gas turbine and reciprocating heat engine applications, entail substantial cyclic loading and thermal

operating temperatures and faster rotational speeds may provide impressive improvements in efficiency, power/weight ratios and fuel consumption. In gas turbine applications, blades, rotors, vanes, shrouds, combuster, combuster liners, and other parts are all candidates for ceramic materials. Here much effort has been directed towards the development of high performance ceramics and reinforced ceramic-matrix composites capable of operating at higher temperatures and higher operating stresses (10,11). While the high temperature properties have received most attention for heat-engine applications, these materials are also being developed for 'stationary' products such as heat exchangers, recuperators, tubes, exhaust systems and similar high-temperature operating equipment (12). Conversely, requirements for reciprocating heat engines stress the need for thermally insulating and wear and abrasion resistant materials (13,14). For example, in addition to hostile environmental conditions, the precombustion chamber in diesel engines must survive both mechanical and thermal stressing which is often cyclic in nature. Large temperature gradients are present and mechanical stresses may be exacerbated by thermal expansion mismatch between the chamber and cylinder-head materials (15). Advantages of ceramic components include improved combustion performance due to higher running temperatures, reduction of idle noise, and easier starting.

Life prediction is naturally crucial to permit the reliable design and use of ceramic materials. Accordingly, extensive research has been undertaken to improve the toughness of ceramics which ultimately translates into improved reliability. Advanced structural ceramics receiving the most attention in the past 15 years has been silicon nitrides, including sialons, silicon carbides, and transformation toughened zirconias (16). Silicon nitrides and carbides are believed to be capable of operating at temperatures up to 1650°C. Zirconia, in addition to being strong up to approximately 600°C, has the advantage of a lower thermal conductivity and a thermal expansivity matching that of many reciprocating engine (particularly diesel) materials. Extensive research is also being undertaken in the development of materials toughened by the addition of dispersed zirconia particles, whisker/fiber reinforced ceramic-matrix composites, microcrack toughening, and more recently the addition of ductile particle dispersions (17,18). A number of the more significant materials, together with their primary toughening mechanism and maximum toughness, are summarized in Table I.

Despite the impact of the potential widespread use of ceramics and ceramic-matrix composites, it is perhaps surprising that relatively few systematic studies of a fundamental nature have been performed to relate mechanistically, and ultimately model, the role of the composite microstructure in controlling subcritical crack growth resistance in these materials. This may be particularly important where crack propagation occurs under cyclic loading conditions. As most of the more significant applications of ceramics, particularly for components in gas turbine and reciprocating heat engine applications, entail substantial cyclic loading and thermal

Table I. Typical Ceramic and Reinforced Ceramic-Matrix Composite Materials Indicating Present Toughness and Toughening Mechanisms (from (18)).

Material	Toughening Mechanism	Maximum Toughness ($MPa\sqrt{m}$)
LAS/SiC	Fiber Reinforced	>20
Glass/C		>20
SiC/SiC		>20
Al_2O_3/SiC(20%)	Whisker Reinforced	10
Si_3N_4/SiC(20%)		14
Al_2O_3/Al(20%)	Ductile Dispersion	>12
B_4C/Al(20%)		>14
WC/Co(20%)		20
PSZ	Transformation Toughened	18
TZP		16
ZTA		10
ZTA	Microcrack Toughened	7
Si_3N_4/SiC		7

shock conditions, a detailed characterization and more fundamental understanding of any fatigue processes must be considered essential.

Accordingly, the principal thesis for future study should be to identify and characterize the salient micromechanisms of subcritical crack propagation processes in ceramics and reinforced ceramic-matrix composites. Particular emphasis should initially be placed on crack growth under cyclic loading conditions at ambient temperature in a selected range of materials exhibiting distinct toughening mechanisms. Subsequently, the study may be extended to include both environmental and high temperature effects. Specifically, it is considered important to relate the mechanisms of subcritical crack growth to the particular toughening mechanism and hence to characteristic features of the microstructure. In addition, hitherto unexplored and potentially useful novel fatigue inhibition techniques, involving, for example, controlled tension or compression overloads and notch geometry effects, should also be assessed. The ultimate aim of this work should be to describe and model in quantitative fashion the mechanisms of failure of advanced ceramic materials on the microstructural scale, and to utilize this understanding to provide a basis for the rational design of new

composite microstructures with improved fracture and fatigue properties.

The discussion in the following sections will focus on a number of major classes of ceramic and ceramic-matrix composites. Each class of material was selected to exhibit distinct toughening mechanisms, namely, transformation and microcrack toughening (eg. partially stabilized zirconia (PSZ), zirconia toughened alumina (ZTA), and SiC reinforced Si_3N_4), deflection and bridging (eg. polycrystalline Al_2O_3, and overaged (stabilized) ZTA and PSZ), fiber/whisker reinforcement (eg. SiC whisker reinforced Al_2O_3 and SiC whisker reinforced Si_3N_4), and ductile particle dispersion toughening (eg. aluminum particle toughened alumina). For each class of material, the processes of extrinsic toughening will briefly be described, followed by a discussion on the possible mechanisms of cyclic fatigue degradation. Finally, suggestions for future work pertinent to each class of material are presented.

5.3.2. Transformation and Microcrack Toughened Materials

Introduction: Significant toughening of brittle ceramic materials can be imparted by stress induced transformations which may include martensitic transformations, as well as twinning (1,19,20). Martensitic toughening, using a dispersed phase of partially stabilized zirconia particles, has been most extensively investigated and is given primary emphasis. In addition, toughening has also be achieved in ceramics prone to microcracking in regions of local residual tension, caused by thermal expansion mismatch or by transformation (2,21). Zone shielding obtains both from the subsequent dilatation governed by the volume displaced by the microcrack, and by the reduction of the elastic modulus within the process zone. Materials which exhibit potent transformation and microcrack toughening mechanisms include, zirconia and alumina ceramics containing partially stabilized zirconia particles as a dispersed phase. SiC reinforced Si_3N_4 ceramic composites exhibit microcrack toughening in addition to bridging effects.

Mechanisms: In the most general sense, the majority of mechanisms that provide extrinsic toughening in ceramics have the common feature that material elements in the region of the the crack surfaces exhibit non-linear behavior with an associated hysteresis. The appreciable non-linear behavior of material elements in the process zone of a transformation toughened material, compared to that of a conventional monolithic ceramic, is schematically illustrated in Figure 5.2. The resulting transformation toughening component can then be explicitly related to the extent of the hysteresis using energy balance considerations (20).

A direct consequence of such toughening in ZTA and PSZ ceramics which involves a strong extrinsic shielding component is crack-size dependent behavior. *R-curve toughness behavior, small crack effects,*

etc., are therefore to be anticipated. In addition, the inelastic behavior of material ahead of the crack tip associated with extensive "transformation plasticity", compared to the very limited microplasticity apparent in monolithic ceramics (Figure 5.2), suggests the strong possibility of fatigue effects. Work reported in the present study (Chapter 4) for a MgO-PSZ has revealed extensive fatigue behavior with properties similar to that observed in metals. Although the precise mechanisms of cyclic crack propagation are presently unclear, the presence of transformation and microcrack phenomena, with associated non-linear behavior, allows speculation on a number of possible effects that may give rise to this behavior.

Tentative mechanisms of fatigue crack propagation may be conveniently categorized into two distinct classes: those that degrade the intrinsic toughness, and those that reduce the component of extrinsic toughening. Possible mechanisms have been identified and are summarized in Figure 5.3.

With regard to degradation of the intrinsic toughness, the effect of cyclic loading may give rise to extensive accumulated damage in the material ahead of the crack tip. This may take the form of localized microplasticity, or microcracking, particularly in grain boundary and particle/matrix interface regions, and be associated with such factors as additional fracture phenomena on the unloading portion of the cycle and the degree of reversibility of the transformation reaction. Additional fracture phenomena may include the operation of Mode II and III crack propagation on unloading due to changes in the local stress state induced by Mode I opening on the loading cycle. In addition, crack propagation during loading may permit relaxation of residual stresses in grains to an unstressed configuration. Subsequent unloading then results in additional tensile and shear stresses which arise from the inability of the relaxed grains to be accommodated in their original positions (22). These effects are likely to be a strong function of residual stress states arising from thermal expansion anisotropy (22), elastic anisotropies of the grains which may give rise to singular stress fields (23), and the nature of cyclic accommodation of transformation strains when these are present in the material. As the magnitude of the residual stress increases with grain size, a pronounced grain size dependence of the fatigue crack propagation may be anticipated.

Reduction of the extrinsic toughness due to cyclic loading may result from changes in the process zone morphology or some form of cyclic accommodation of the transformation strain (possibly associated with the type of martensitic twin variants that form in transformable particles on repeated loading). As already discussed, the high stress fields induced ahead of the process zone on unloading may result in an increased frontal process zone and concomitant decrease in shielding. In addition, a somewhat more conjectural explanation might involve some form of cyclically induced strain preconditioning of the process zone that changes the transformation criterion from being shear dominated to the markedly smaller zone

associated with a hydrostatic criterion. Clearly, however, detailed studies of cyclically induced transformation kinetics and zone morphology are required to provide a basis for a deeper understanding of the micromechanisms of fatigue crack propagation in zone shielded ceramics.

Future Work: In light of the above considerations with regard to the possible effects and implications of transformation and microcrack toughening mechanisms on subcritical cyclic crack extension, future work should be directed towards initially assessing the susceptibility to fatigue crack propagation of a number of materials in which the above shielding mechanisms are dominant. In particular, attention should be placed on identifying any degradation mechanisms that may be operating to decrease either the intrinsic toughness (in material ahead of the crack tip), or the extrinsic toughness (in the wake of the crack).

A novel ingredient for future studies should be the ability to monitor quantitatively the contribution from crack tip shielding in situ during test procedures, using back-face strain compliance (8) and caustics measurements (24). The former technique permits estimates of the reduction in local "crack driving force" principally from crack wedging and bridging during fatigue crack propagation. Estimates of the reduced driving force may then be verified through the use of local measurements of the stress intensity at the crack tip using the method of caustics (24). In addition, shielding by deflection may be estimated from the crack path morphology, using the stress intensity solutions for deflected cracks (25). Information on the local variations in crack tip stress intensity may additionally be obtained through experiments on long fatigue cracks in compact C(T) samples, where the crack wake is progressively removed by micro-machining, while simultaneously monitoring the degree of shielding. This technique has been successfully used elsewhere to investigate the effect of a bridging zone on crack propagation in a Al_2O_3 ceramic (26).

Identifying and quantifying the effect of mechanical variables controlling any fatigue crack propagation behavior apparent in these materials should also be considered. These may include the effect of the mean stress (load ratio), the frequency and the waveform. In addition, the existence of any small crack effects from experiments on crack initiation and the early growth of small (500 to 2000 mm) naturally-occurring flaws in unnotched samples, strongly suggested by the presence of marked R-curve behavior of these materials, should also be assessed. An important additional aspect of this work should be to investigate the possible existence of novel fatigue resistance enhancement techniques, in which fatigue crack propagation may be inhibited. These may include the effects of overloads (both tension and compression) in which the residual stresses, or the effect of additional crack advance induced by the overload, may provide increased extrinsic shielding and hence an inhibition of fatigue crack growth. The significance of notch geometry may also be

evaluated with regard to defining its role on the initiation and subsequent growth of fatigue cracks.

Additional considerations for future work should include an investigation of environmental effects on the fatigue crack propagation behavior of these materials. Sample tests should therefore be conducted in inert and aggressive environments (for example, dry gaseous argon versus distilled water) in order to quantify the environmental contribution to crack extension. Finally, it is considered important in light of the envisaged high temperature requirements for the present materials, to study the effects of elevated temperature on subcritical crack growth, once again with particular emphasis on fatigue loading conditions. At high temperatures, creep rupture studies indicate that cracks either propagate to critical size for fracture, or they blunt, which is accompanied by shear band formation and growth (27). Eventual failure then occurs by damage accumulation within these shear bands. Shear-band formation and growth, and the associated damage accumulation, therefore emerge as significant mechanisms in creep rupture. Accordingly, higher temperatures are expected to produce significant effects on the fatigue crack propagation behavior. These may include the introduction of non-linearity in the stress-strain response of the material elements in the high stress fields ahead of the crack tip, and additional damage mechanisms that relate to the extension of pre-existing flaws and those that involve flaw generation due to [illegible].

5.3.3. Deflection and Bridging Materials

Introduction: Mechanisms of deflection and bridging are expected to operate in most ceramic and ceramic-matrix materials. With regard to future studies, however, it is considered important to select some materials in which these mechanisms are the principal source of extrinsic toughening. In particular, it should be possible to isolate and quantify the contribution of these mechanisms in a polycrystalline alumina ceramic, and a stabilized zirconia toughened alumina (ZTA) and overaged partially stabilized zirconia (PSZ) ceramic in which the transformation toughening mechanisms have been inhibited.

Mechanisms: In brittle ceramic materials, cracks may be deflected either by localized residual stress fields, or by fracture resistant second phase particles or precipitates where deflection angles are functions of the volume fraction and morphology of the particles (28). Deflection causes both tilting and twisting of the crack front. The resulting reduction of the crack tip driving force is a function of the tilt and twist angles alone. Where deflection is dominated by particles incorporated in the matrix, for example, precipitates in PSZ and ZTA materials or ZnO-ZrO_2 alloys, the maximum predicted increase in toughness is from 50 to 70% under monotonic loading (29). However, the size, rather than simply the angle, of the deflected crack segment may have an effect on time dependent crack advance, as

it dictates the extent of crack extension which experiences the reduced driving force. Accordingly, shielding through crack deflection can be more significant in affecting subcritical crack growth rates, such as those by fatigue or sustained load environmentally-assisted crack growth.

The extent of shielding which derives from a bridging zone of ligaments in the wake of an advancing crack is less well understood. Bridging may derive from uncracked ligaments and crack bridges, or frictional and geometrical interlocking of microstructurally rough fracture surfaces. In both cases significant toughening may derive and has been observed to produce R-curve behavior in alumina and other non-phase transforming ceramics (26,30-32). In general, however, the amount of shielding is expected to be less than that associated with particle or fiber/whisker bridging of the crack flanks in composite microstructures under monotonic loading. The effect of cyclic loading on crack advance which is impeded primarily by bridging mechanisms is less apparent. Indeed, it is not well established whether true fatigue crack growth behavior under tension-tension loading conditions even exists in these materials which do not display a non-linear stress strain response ahead of the crack tip. However, whereas crack deflection may only have implications with regard to decreasing crack growth rates in materials already prone to fatigue crack propagation, it seems likely that any accumulative damage of the bridging zone by cyclic loading may lead to a reduction of the extrinsic shielding and hence the possibility of further crack advance. Such degradation of the bridging zone may take the form of progressive interface-localized microcracking, including both friction-induced microcracking of interlocking rough asperities and localized microcrack rupture of the intact crack wake ligaments.

Future Work: For the present deflection and bridging toughened materials, future investigations should follow the techniques and approaches outlined for the transformation and microcracking materials. Preliminary studies should therefore i) initially characterize the fatigue crack propagation behavior, specifically with the objective of identifying the role of the salient intrinsic and extrinsic toughening mechanisms, and ii) develop quantitative micro-mechanical models to account for such subcritical crack growth behavior. Subsequent work should concentrate on i) defining the role of mechanical variables such as load ratio, frequency, and waveform in controlling crack growth rates, ii) investigating any apparent small crack behavior, and iii) assessing the potential of novel fatigue inhibition techniques. Final studies should explore environmental and high temperature ($\sim 1000^{o}C$) effects on subcritical crack propagation behavior.

5.3.4. Whisker Reinforced Ceramic-Matrix Materials

Introduction: Much work on ceramic-matrix composites to date has been directed towards discontinuous (short fiber/particulate)

composites, such as silicon carbide whisker reinforced alumina, mullite and silicon nitride matrices, as these materials show very attractive properties (e.g., enhanced strength and toughness, wear resistance and creep properties), particularly at high temperatures.

Mechanisms: Toughening mechanisms in ceramic-matrix composite materials are expected to result in a substantial extrinsic shielding component, with associated R-curve behavior. Such mechanisms are likely to include crack stopping and delamination/debonding at fiber interfaces, frictional work following debonding, crack bridging, fiber pull-out effects, and crack deflection. It will thus be essential in future studies to identify the relevance and implications of these processes to fully understand the subcritical crack growth behavior of these materials. Of particular significance will be identifying the role of the fiber and interface strengths, as this will govern the relative importance of the crack bridging (weak interface strength) and pull-out (weak fiber strengths) toughening mechanisms. As the fiber and matrix typically have comparable toughness, in the absence of debonding the composite is brittle and toughness behavior satisfies the rule of mixtures. Conversely, debonding reduces the amplitude of the singularity at the fiber and, when sufficiently extensive, allows the crack to circumvent the fiber, leaving the fiber intact in the crack wake (18). The bridging zone of intact fibers in the crack wake inhibits crack opening, thus shielding the crack from the applied driving force. The marked importance of interfacial strength is therefore apparent.

The effect of cyclic loading conditions on these materials has received virtually no attention, and hence, particularly for tension-tension loading, effects may only be surmised. However, similar to crack bridging effects discussed previously, fatigue loading may be expected to produce a progressive degradation in the shielding capacity of the bridging zone through weakening of the whisker-matrix interfacial strength. In addition, decreases in the intrinsic toughness of the composite caused by damage accumulation ahead of the crack tip may also be expected. Here the source of the microcrack initiation sites, however, remains uncertain; grain boundaries, clusters of SiC whiskers, individual whiskers, and interfacial oxide layers, may all be implicated.

Future Work: The study of whisker reinforced materials should follow a similar basic scheme to that previously detailed in the preceding sections. Specifically, future work should attempt to initially relate any fatigue crack propagation behavior in ceramic-matrix composites to controlled volume fractions of whisker reinforcement. In addition, using selected heat treatments, the whisker/matrix interfacial strength should be altered to assess the influence of varying degrees of effective whisker reinforcement on such subcritical crack growth behavior. In order to isolated salient micromechanisms of subcritical crack propagation in these materials, the microstructural origins of accumulated microcracking damage and

fiber debonding should be investigated, as a function of such variables as grain size, fiber/matrix interfacial strength (using repeated loading nano-hardness indentation techniques), and fiber shape, size and volume fraction.

5.3.5. Ductile Phase Toughened Materials

Introduction: It has recently been recognized that the toughness of brittle ceramic materials may be increased by the introduction of a dispersed ductile phase, to produce materials of high toughness, coupled with other desirable properties (18,33). Although WC/Co is perhaps the most recognized example, the present discussion will concentrate on the more recent Al_2O_3/Al ceramic-matrix composite.

Mechanisms: The use of a dispersed ductile phase is a particularly potent toughening mechanism, provided the crack path can be made to intersect that phase. In other material systems, procedures such as making the phase continuous (e.g., in cobalt reinforced tungsten carbide) or with a low modulus (e.g., in rubber-toughened polymers) have been particularly successful to achieve this end. Two sources of toughening are governed by the plasticity of the ductile phase (18,33). Particles intercepted by the crack, when bonded to the matrix, may exhibit extensive plastic stretching in the crack wake and contribute to the toughness by inhibiting crack opening. Simultaneously, plastic straining of the particles in the process zone causes zone shielding of the crack tip. Possible mechanisms of subcritical fatigue crack propagation in these materials are necessarily at present of a highly conjectural nature; however, similar mechanisms as those expected in whisker reinforced composites and materials exhibiting crack bridging may be anticipated. In addition, the effect of work hardening/softening and classical metal fatigue of the ductile ligaments in the bridging zone may contribute to interesting crack growth behavior.

Future Work: A number of substantial issues remain to be addressed with regard to the crack propagation behavior under both monotonic and cyclic loading in ductile phase toughened composites. This is primarily due to the very recent introduction of this material and hence limited commercial interest, particularly of the Al-toughened Al_2O_3. Depending on the results of preliminary studies, in which computations of toughening and potential commercial interest are established, detailed studies of the effects of cyclic fatigue degradation will be required.

5.4. REFERENCES

1. R. M. McMeeking and A. G. Evans, J. Amer. Cer. Soc., 65, 242, 1982.

2. A. G. Evans and K. T. Faber, J. Amer. Cer. Soc., 67, 255 1984.

3. L. Peck, C. C. Barton and R. B. Gordon, J. of Geophys. Res., 90, 11533, 1985.

4. J. Labuz, S. P. Shah and C. H. Dowling, Int. J. of Rock Mech. and Mining Sci., 22, 85, 1985.

5. R. O. Ritchie and A. W. Thompson, Metall. Trans. A, 16A, 223, 1985.

6. K. T. Venkateswara Rao, W. Yu and R. O. Ritchie, Scripta Met., 20, 1459, 1986.

7. S. Suresh and R. O. Ritchie, Int. Metals Reviews, 29, 445, 1984.

8. R. O. Ritchie and W. Yu, in Small Fatigue Cracks, R. O. Ritchie and J. Lankford, eds., TMS-AIME, Warrendale, PA, 167, 1986.

9. R. F. Cook, to be published (1987).

10. A. Bennett, Mater. Sci. Technol., 2, 891, 1986.

11. D. W. Richerson, Am. Ceram. Soc. Bull., 64, 282, 1985.

12. L. M. Sheppard, Adv. Mater. Pro., 1, 39, 1985.

13. D. A. Parker, Mater. Sci. Technol., 9, 900, 1986.

14. M. E. Woods, W. F. Mandler and T. L. Scofield, Am. Ceram. Soc. Bull., 64, 287, 1985.

15. L. M. Sheppard, Adv. Mater. Pro., 2, 35, 1986.

16. S. Robb, Am. Ceram. Soc. Bull., 62, 556, 1983.

17. F. L. Riley, S. J. Milsom, Mater. Sci. Technol., 9, 891, 1986.

18. A. G. Evans, in Fracture Mechanics - 20th Symposium, ASTM STP, R. P. Wei and R. P. Gangloff, eds., American Society for Testing and Materials, Philadelphia, PA, 1987.

19. R. C. Gravie, R. H. Hannink and R. T. Pascoe, Nature (London), 258, 703, 1975.

20. B. *Budiansky, J. W. Hutchinson* and J. C. Lambropoulos, Int. J. Solid Struct., 19, 337, 1983.

21. N. Claussen, J. Steeb and *R. F. Pabst*, *Am. Ceram. Soc. Bull.*, 56, 559, 1977.

22. D. Lewis, Cer. Eng. Sci. Proc., 4, 847, 1983.

23. *V. Tvergaard and J. W. Hutchinson*, "Micro-Cracking in Ceramics Induced by Thermal Expansion or Elastic Anisotropy," MECH-96, Division of Applied Sciences, Harvard University, Cambridge, MA 1986.

24. P. S. Theocaris and G. A. Papadoupoulos, Eng. Fract. Mech., 13, 683, 1980.

25. *S. Suresh*, *Metall. Trans. A*, 14A, 2375, 1983.

26. F. Deuerler, R. Knehans and R. Steinbrech, J. Physique, 47, 617, 1986.

27. B. J. Dalgleish and E. B. Slamovich, Adv. Mat. Processes, 2, 31, 1986.

28. *K. T. Faber and A. G. Evans*, Acta Met., 31, 565, 1983.

29. A. G. Evans and R. M. Cannon, Acta Met., 34, 761, 1986.

30. R. F. Cook, C. J. Fairbanks, B. R. Lawn and Y.-W. Mai, J. Am. Ceram. Soc., to be published (1987).

31. P. L. Swanson, Adv. in Ceramics, Am. Ceram. Soc., Columbus, OH *in press* (1987).

32. B. S. Majumdar, A. R. Rosenfield and W. H. Duckworth, "Crack Resistance Behavior of *Non-Phase-Transforming Ceramics*," Physical Metallurgy Section, Battelle Columbus Division, Columbus, OH (1986).

33. L. S. Sigl, P. Mataga, B. J. Dalgleish, R. M. McMeeking and A. G. *Evans, to be published* (1987).

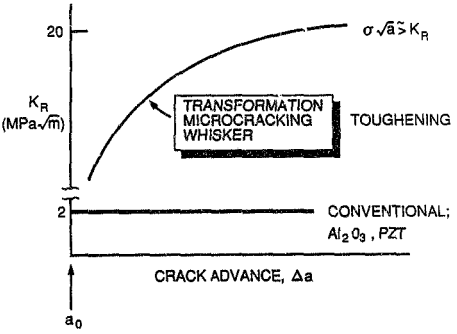


Figure 5.1 Resistance curve behavior illustrating the increase in fracture resistance with crack advance typically encountered in toughened ceramics.

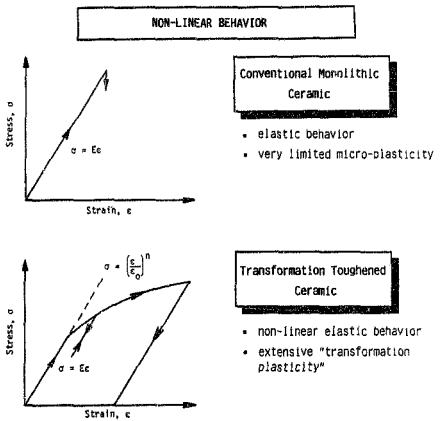


Figure 5.2 Schematic illustration of *non-linear behavior of material* in the process zone of transformation toughened ceramics compared to that of conventional monolithic ceramics.

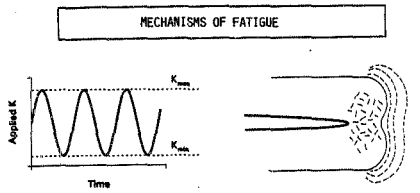


Figure 5.3 *Summary of possible mechanisms of fatigue in transformation toughened ceramics, indicating distinctions between those that influence the intrinsic and extrinsic toughness.*

Author Dauskardt Reinhold Horst
Name of thesis Crack Tip Shielding In Fracture And Fatigue: Extrinsic Versus Intrinsic Toughening. 1987

PUBLISHER:
University of the Witwatersrand, Johannesburg
©2013

LEGAL NOTICES:

Copyright Notice: All materials on the University of the Witwatersrand, Johannesburg Library website are protected by South African copyright law and may not be distributed, transmitted, displayed, or otherwise published in any format, without the prior written permission of the copyright owner.

Disclaimer and Terms of Use: Provided that you maintain all copyright and other notices contained therein, you may download material (one machine readable copy and one print copy per page) for your personal and/or educational non-commercial use only.

The University of the Witwatersrand, Johannesburg, is not responsible for any errors or omissions and excludes any and all liability for any errors in or omissions from the information on the Library website.